

2013-01-01

A Block Operator Splitting Method for Heterogeneous Multiscale Poroelasticity

Paul M. Delgado

University of Texas at El Paso, pmdelgado2@utep.edu

Follow this and additional works at: https://digitalcommons.utep.edu/open_etd



Part of the [Applied Mathematics Commons](#), [Geophysics and Seismology Commons](#), and the [Mechanical Engineering Commons](#)

Recommended Citation

Delgado, Paul M., "A Block Operator Splitting Method for Heterogeneous Multiscale Poroelasticity" (2013). *Open Access Theses & Dissertations*. 1807.

https://digitalcommons.utep.edu/open_etd/1807

A BLOCK OPERATOR SPLITTING METHOD
FOR HETEROGENEOUS MULTISCALE POROELASTICITY

PAUL M. DELGADO

Computational Science Program

APPROVED:

Vinod Kumar, Chair, Ph.D.

Son Young Yi, Ph.D.

Aaron Velasco, Ph.D.

Reza Ashtiani, PhD.

Benjamin Flores, Ph.D.
Dean of the Graduate School

©Copyright

by

Paul Delgado

2013

to my

WIFE, MOTHER, FATHER, and SISTER

with love.

A BLOCK OPERATOR SPLITTING METHOD
FOR HETEROGENEOUS MULTISCALE POROELASTICITY

by

PAUL M. DELGADO, B.S., M.S.

THESIS

Presented to the Faculty of the Graduate School of

The University of Texas at El Paso

in Partial Fulfillment

of the Requirements

for the Degree of

MASTER OF SCIENCE

Computational Science Program

THE UNIVERSITY OF TEXAS AT EL PASO

August 2013

Acknowledgements

Contrary to popular belief, a doctorate degree is not the sole product of an individual's efforts, skills, and perseverance. It is the culmination of all of mankind's effort to understand the world around us and, more importantly, of the people around us who encourage and enable the pursuit of the unknown. Here, I present to you the true heroes and heroines of my journey toward my PhD.

First and foremost, I thank my rock, my soulmate, my one and only true love, Sarah; who without her unending compassion, understanding, and encouragement, none of this research would have been possible. Her unending belief in me, even in those dark days when I did not believe in myself, enabled me to persevere to the very end.

To my parents, who taught me the value of hard work and engrained in me my moral compass. The prime directive, as they said, is to always do good for yourself, for your family, and for the world. It is their vision of a better world that helped me see my future as a computational scientist, working on the challenging problems that our world faces and finding solutions that benefit us all.

To my advisors, Dr. Vinod Kumar and Dr. Son Young Yi, who constantly challenge me to higher standards of integrity and competence in research. I am ever grateful not only for their guidance, but also their unending faith in my ability to tackle problems in ways that no one else ever has :)

NOTE: This thesis was submitted to my Supervising Committee on the July 6th, 2013.

Abstract

Traditional models of poroelastic deformation in porous media assume relatively homogeneous material properties such that macroscopic constitutive relations lead to accurate results. Many realistic applications involve heterogeneous material properties whose oscillatory nature require multiscale methods to balance accuracy and efficiency in computation.

The current study develops a multiscale method for poroelastic deformation based on a fixed point iteration based operator splitting method and a heterogeneous multiscale method using finite volume and direct stiffness methods. To characterize the convergence of the operator splitting method, we use a numerical root finding algorithm to determine a threshold surface in a non-dimensional parameter space β separating convergent & divergent problems. We also use the method of manufactured solutions to verify the proposed multiscale algorithm.

Results suggest that non-dimensional parameter values β above the threshold surface ensure convergence, with increasing rate of convergence as $\beta \rightarrow \infty$. For a given spatial discretization Δx , convergence can be ensured by choosing larger time stepsizes Δt .

The proposed multiscale algorithm converges for the decoupled solid deformation PDE with analogous behaviors as observed in Chu et al. (2012). We observed divergence in our multiscale algorithm for the decoupled fluid equation in the heterogeneous case and attribute it to lack of monotonicity preservation induced by the reaction term in the microscale model. An alternative cross-sectional flux estimator is proposed to improve convergence.

Table of Contents

	Page
Acknowledgements	v
Abstract	vi
Table of Contents	vii
List of Tables	x
List of Figures	xi
Chapter	
1 Introduction	1
1.1 Overview	1
1.2 The Problem	3
1.3 The Proposed Solution	5
2 Literature Review	7
2.1 Poroelasticity	7
2.1.1 Solid Deformation	7
2.1.2 Fluid Flow	9
2.2 Multiscale Modeling	13
2.2.1 Upscaling Methods	14
2.2.2 Divide & Conquer Methods	16
2.2.3 Heterogeneous Multiscale Method	17
2.2.4 Chu et. al.'s Model	18
Microscale Model	18
Macroscopic Model	20
Iterative Coupling Algorithm	21
2.3 Operator Splitting	22
2.3.1 Fractional Step Methods	24

2.3.2	Kim et al's work	25
2.4	Summary	27
3	Methodology	29
3.1	Assumptions	29
3.2	Operator Splitting	31
3.2.1	Block Jacobi Splitting	32
3.2.2	Block Gauss-Seidel Splittings	33
3.2.3	Convergence	34
3.3	Generalization of Chu et al.'s Multiscale Method	36
3.3.1	Macroscopic Model	38
3.3.2	Microscopic Deformation Model	40
3.3.3	Microscopic Flow Model	42
3.4	Research Questions	43
4	Operator Splitting Experiments	45
4.1	Case I	45
4.1.1	Results	48
4.2	Case II	50
4.2.1	Results	57
5	Multiscale Experiments	63
5.1	Verification of Chu et al.'s method	63
5.1.1	Experiment I	67
5.1.2	Experiment II	69
5.1.3	Experiment III	70
5.2	Multiscale Solid Deformation	74
5.2.1	Results	75
5.3	Multiscale Elliptic Reaction-Diffusion	79
5.3.1	Results	81
6	Discussion	90

6.1	Operator Splitting	90
6.1.1	Key Findings	90
6.1.2	Limitations	91
6.2	Multiscale Methods	92
6.2.1	Key Findings	93
6.2.2	Limitations	94
7	Future Work	96
	References	98
	Curriculum Vitae	106

List of Tables

4.1	Convergence Table for $\alpha = 1$, $\Delta t = 0.001$, and $\Delta x = 0.002$	50
4.2	Convergence for $c_0 = 1$	58
4.3	Convergence for $c_0 = 0.5$	58
5.1	Relative Error in multiscale model solution w.r.t. fully microscopic model in the constant conductance case	84
5.2	Relative Error in finite difference solution w.r.t. fully microscopic model . .	85

List of Figures

1.1	Conceptually, one can observe poroelasticity through the time dependent effects of external loads applied to a wet, saturated sponge. As it is squeezed, it both deforms the solid material and induces fluid flow.	2
1.2	Modeling highly heterogeneous materials using continuum scale discretization produces a trade-off between efficiency and accuracy. (a) Highly accurate models are too detailed to yield computationally tractable solutions. (c) Tractable, efficient solutions are highly inaccurate. (b) Multiscale models balance the need for accuracy and efficiency	4
2.1	A structured 8x8 microscale network model with constant pore size and random throat radii.	19
2.2	Macroscale-microscale model coupling, adapted from [26, 25]	20
2.3	Visualization of the four operator splitting methods developed by Kim[46].	26
3.1	Depiction of the 1D Terzaghi Problem, adapted from Mitchison et. al.[52] .	30
3.2	Visualization of the heterogeneous multiscale model sampling the fully microscopic model. In the fluid flow case, the fully microscopic model is a network model of pores and throats. In the solid deformation case, it is an assemblage of spring elements using in a direct stiffness model.	37
4.1	Staggered grid for finite difference discretization. Open and closed circles represent displacement and pressure points, respectively.	48
4.2	Threshold Surface β^* at various Δt and Δx values with $\alpha = 1$	51
4.3	Threshold Surface β^* at various Δt and Δx values with $\alpha = 0.8$	51
4.4	Threshold Surface β^* at various Δt and Δx values with $\alpha = 0.5$	52
4.5	Threshold Surface β^* at various Δt and Δx values with $\alpha = 0.2$	52

4.6	Threshold Surface β^* at various Δt and Δx values with $\alpha = 1$	53
4.7	Threshold Surface β^* at various Δt and Δx values with $\alpha = 0.8$	53
4.8	Threshold Surface β^* at various Δt and Δx values with $\alpha = 0.5$	54
4.9	Threshold Surface β^* at various Δt and Δx values with $\alpha = 0.2$	54
4.10	Threshold Surface β^* at various Δt and Δx values with $\alpha = 1$	55
4.11	Threshold Surface β^* at various Δt and Δx values with $\alpha = 0.8$	55
4.12	Threshold Surface β^* at various Δt and Δx values with $\alpha = 0.5$	56
4.13	Threshold Surface β^* at various Δt and Δx values with $\alpha = 0.2$	56
4.14	Threshold Surface of optimal y-intercept b^* values at various Δt and Δx values with $\alpha = c_0 = 1$ and $m = 0.01$	59
4.15	Threshold Surface of optimal y-intercept b^* values at various Δt and Δx values with $\alpha = c_0 = 1$ and $m = 0.1$	60
4.16	Threshold Surface of optimal y-intercept b^* values at various Δt and Δx values with $\alpha = c_0 = 1$ and $m = 1.0$	60
4.17	Threshold Surface of optimal y-intercept b^* values at various Δt and Δx values with $\alpha = c_0 = 1$ and $m = 10.0$	61
4.18	Threshold Surface of optimal y-intercept b^* values at various Δt and Δx values with $\alpha = c_0 = 1$ and $m = 100.0$	61
4.19	Threshold Surface of optimal y-intercept b^* values at various Δt and Δx values with $\alpha = c_0 = 1$ and $m = 1000.0$	62
5.1	Illustration of a one dimensional multiscale flow model method sampling a two-dimensional pore network model	64
5.2	Conductance distribution for Fluid Flow Case I.	65
5.3	Conductance distribution for Fluid Flow Case II.	66
5.4	A random conductance distribution for Fluid Flow Case III.	66

5.5	Experiment I Constant μ Analysis: Solid lines represent a constant number of sampling domains μ with relative errors displayed for pressure (left) and flux (right).	67
5.6	Experiment I Constant $\mu\delta$ Analysis: Solid lines represent a constant total sampling area $\mu\delta$ with relative errors displayed for pressure (left) and flux (right).	68
5.7	Experiment II Constant μ Analysis: Solid lines represent a constant number of sampling domains μ with relative errors displayed for pressure (left) and flux (right) in the linearly varying conductance case.	69
5.8	Experiment II Constant $\mu\delta$ Analysis: Solid lines represent a constant total sampling area $\mu\delta$ with relative errors displayed for pressure (left) and flux (right) in the linearly varying conductance case.	70
5.9	Experiment III Constant μ Analysis: Solid lines represent a constant number of sampling domains μ with relative errors displayed for pressure (left) and flux (right) in the random conductance case.	71
5.10	Experiment III Constant $\mu\delta$ Analysis: Solid lines represent a constant total sampling area $\mu\delta$ with relative errors displayed for pressure (left) and flux (right) in the random conductance case.	71
5.11	Comparison between the averaged fully microscopic solution and the multi-scale solution with $\mu = 8$ subdomains and sample size $\delta = 4$	72
5.12	Comparison between the averaged fully microscopic solution and the multi-scale solution with $\mu = 8$ subdomains and sample size $\delta = 8$	72
5.13	Comparison between the averaged fully microscopic solution and the multi-scale solution with $\mu = 8$ subdomains and sample size $\delta = 16$	72
5.14	Comparison between the averaged fully microscopic solution and the multi-scale solution with $\mu = 8$ subdomains and sample size $\delta = 32$	73
5.15	Stiffness distribution for Solid Deformation Case I.	74
5.16	Stiffness distribution for Solid Deformation Case II.	74

5.17	A random stiffness distribution for Solid Deformation Case III.	75
5.18	Multiscale deformation errors for constant stiffness and constant μ , varying sample size δ	76
5.19	Multiscale deformation errors for constant stiffness and constant sampling area $\mu\delta$, varying number of sampling subdomains μ	77
5.20	Multiscale deformation errors for linearly increasing and constant μ , varying sample size δ	78
5.21	Multiscale deformation errors for linearly increasing stiffness and constant sampling area $\mu\delta$, varying number of sampling subdomains μ	78
5.22	Average multiscale deformation errors for 100 random stiffness tests with constant μ , varying sample size δ	79
5.23	Average multiscale deformation errors for 100 random stiffness tests with constant sampling area $\mu\delta$, varying number of sampling subdomains μ	80
5.24	Exact, finite difference, and multiscale solutions to the reaction-diffusion equation with constant conductance $K(x) = 1$ and various number of sampling subdomains μ and $\delta = 4$. All graphs are plotted with a logarithmic scale on y-axis.	82
5.25	Exact, finite difference, and multiscale solutions to the reaction-diffusion equation with linearly increasing conductance $K(x) = x$ and various number of sampling subdomains μ and $\delta = 4$. All graphs are plotted with a logarithmic scale on y-axis.	83
5.26	Logarithms of relative pressure error for Multiscale Reaction-Diffusion PDE with constant conductance; holding μ constant and increasing δ	85
5.27	Logarithms of relative pressure error for Multiscale Reaction-Diffusion PDE with constant conductance, holding total sample area $\mu\delta$ constant and increasing μ	86
5.28	Logarithms of relative pressure error for Multiscale Reaction-Diffusion PDE with linearly varying conductance, holding μ constant and increasing δ . . .	87

5.29	Logarithms of relative pressure error for Multiscale Reaction-Diffusion PDE with linearly varying conductance, holding total sample area constant $\mu\delta$ and increasing μ	88
5.30	Logarithms of average relative pressure error for Multiscale Reaction-Diffusion PDE with random conductance, holding μ constant and increasing δ	89

Chapter 1

Introduction

1.1 Overview

Poroelasticity is the study of the transitory interactions between solid deformation and fluid flow within a porous medium. It is characterized by a time dependent, two-way coupling where changes in the state variables of one phase alter those of the other. As illustrated by the poroelastic medium in figure 1.1, applying external load to a saturated porous medium causes changes in the fluid pressures which induces a flow. Likewise, a change in fluid pressures induces stresses that deform the solid skeleton. Karl Terzaghi, a founding father of modern soil mechanics, was the first to observe and characterize the coupling phenomenon in a single dimension[27, 64]. The equations governing poroelasticity matured into a full multi-dimensional theory with the groundbreaking work of Maurice Biot [15, 16, 17]. Biot's equations were initially derived phenomenologically[56] and later validated rigorously by analytical means[22, 20] and experimental observation[44].

Central to the success of Biot's model is its predictive nature in a wide range of applications. Petroleum engineers extract oil by injection of fluids and are vitally interested in issues such as injectivity maintenance surface subsidence[56]. Studies on carbon sequestration and storage technology model the risks of leakage and fracture formation associated with carbon storage using poroelasticity theory[54]. Geotechnical engineers employ Biot's models to characterize soil properties and design appropriate foundations for various structures[61]. Seismologists use Biot's equations in conjunction with Mohr-Coulomb theory for fault activation and interaction studies[28, 29]. Soil scientists also develop irrigation and crop management strategies under the theory of poroelasticity. Hydrologists



Figure 1.1: Conceptually, one can observe poroelasticity through the time dependent effects of external loads applied to a wet, saturated sponge. As it is squeezed, it both deforms the solid material and induces fluid flow.

manage aquifers, water wells, and dams with the guidance of poroelasticity equations[21]. Biological applications include bone deformation[30] and soft tissue modeling[5].

Despite the existence of a number of *analytical* solutions[11, 10, 19, 15, 50, 9] for specific cases, Biot's poroelasticity equations have no closed form analytical solution in the general case. Philips[56] specifies three specific cases of particular importance which have analytical solutions:

- *Terzaghi's Problem*[27]: A one dimensional consolidation problem closely validated against experimental results and whose analytical series solution was obtained by Biot[15]
- *Mandel's Problem*[50]: A two dimensional problem involving a saturated porous media squeezed between two rigid plates. Its solution illustrates a temporary increase in pore pressures above those produced by the initial loading. This is known as the "Mandel-Creyer" effect and its existence demonstrates the importance of time dependent coupling between flow and deformation.
- *Barry & Mercer's Problem*[9]: A problem involving an oscillating point source/sink

term which artificially mimics an injection/production process common in petroleum reservoir simulation. Boundary conditions are specifically chosen to produce an analytical solution.

In contrast, a number of numerical methods have been developed. Zenisek[68] and Showalter [63] characterized the existence and uniqueness of weak and strong solutions of Biot’s equations, respectively. Showalter [63] further demonstrated that the partial differential equations in biot’s equations essentially form a parabolic system[56]. Finite Element Methods [67, 57, 58, 59, 46, 71, 70] are by far the most commonly used approach to solving these equations, with mixed finite element methods being the most ubiquitous among them. Extensive analysis of various one dimensional finite difference methods [41, 39, 42, 40, 1] shows that the use of staggered grids for displacement and pressure leads to greater numerical stability. The recent work of Naumovich[53] extends the Marker & Cell grid method of Gaspar [40] into a generalized 3D finite volume method with staggered control volumes. More recent efforts emphasize operator splitting methods[46, 37] to enable legacy code reuse.

1.2 The Problem

One key phenomenon not addressed by conventional numerical methods for poroelasticity is the existence of heterogeneous material properties in natural porous media. The standard Biot model of poroelasticity assumes relatively homogenous material properties such that elastic moduli and permeabilities are either constant or slowly varying. In various applications[45, 7, 62, 4], spatial distributions of permeability and elastic moduli vary significantly at scales significantly smaller than the typical modeling domain of interest. For example, oil reservoirs require simulations on domains on the order of kilometers while the fundamental scale of heterogeneity in permeability may be millimeters or less[43]. Soils mixtures comprised of organic and inorganic solids and varying grain sizes also oscillate tremendously in terms of elastic modulus and permeability. The ubiquitous presence of nat-

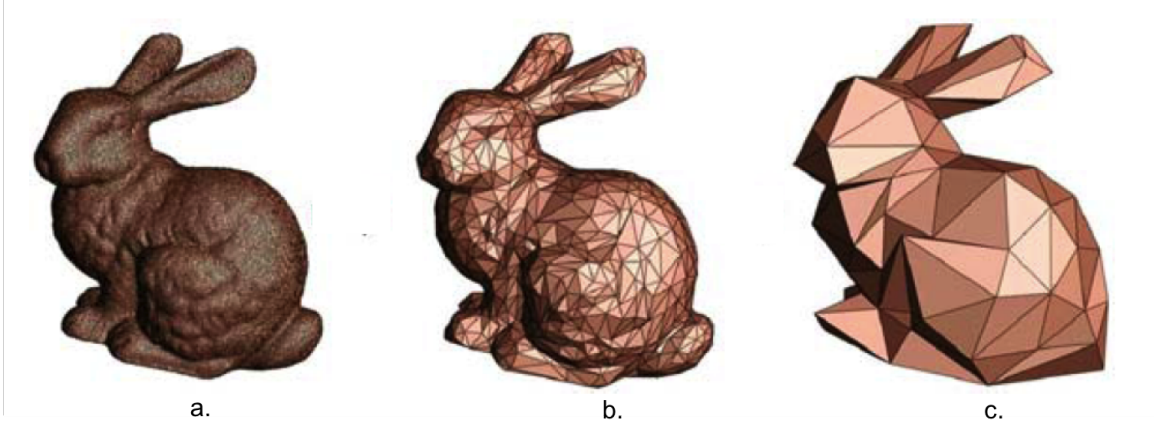


Figure 1.2: Modeling highly heterogeneous materials using continuum scale discretization produces a trade-off between efficiency and accuracy. (a) Highly accurate models are too detailed to yield computationally tractable solutions. (c) Tractable, efficient solutions are highly inaccurate. (b) Multiscale models balance the need for accuracy and efficiency

ural fractures further complicates the distribution of stiffnesses in subsurface formations[8].

The distribution of large contrasts in both permeability and stiffness over small spatial scales complicated numerical simulation result in large relative errors when numerical discretization h in space is larger than the scale of heterogeneity ϵ [3]. Consequently, highly accurate poroelasticity simulation results are computationally expensive or intractable by conventional discretization methods.

Multiscale methods emerged from the need to address heterogeneity while balancing the competing needs for accuracy and efficiency. They can be broadly classified in one of two strategies: Upscaling and Divide & Conquer. Upscaling methods attempt to replace the fine scale problem with an effective coarse scale description by means of an averaging process[55]; typically either volume averaging or asymptotic homogenization. Divide & Conquer methods aim to decompose the fine scale problem into many small subproblems; each of whose solution is easily computed.

Both multiscale approaches have advantages and disadvantages. Upscaling methods are widely applicable to many various partial differential equation models, including poroelasticity[13].

They are highly accurate under certain assumptions such as periodicity or isotropy. For general heterogeneous materials, these assumptions may not be valid and upscaling can lead to high relative errors. On the other hand, Divide & Conquer methods handle general heterogeneity with more accuracy but must be tailored to a specific problem or model in question.

A brief survey on multiscale literature reveals that a large body multiscale methods apply to elliptic PDE's with a single dependent variable[24]. Multiscale methods for coupled problems is an active area of contemporary research. As far as the current author is aware, no known Divide & Conquer methods directly address heterogeneity in Biot's poroelasticity equations.

1.3 The Proposed Solution

Motivated by Kim[46]'s recent work on legacy code reuse in poroelasticity, the current thesis proposes a method which decomposes the multiscale poroelasticity equations into a sequence of elliptic partial differential equations sufficiently general to capitalize on the ample algorithms available for multiscale elliptic PDE's. This method is based on block operator splittings of the poroelasticity equations based on fixed point iterations. The resulting formulation is a pair of continuous elliptic PDE subproblems with multiscale coefficients. In this formulation, any applicable multiscale algorithm can be applied to solve the resulting flow and deformation equations separately. The current thesis also proposes an extension to an existing heterogeneous multiscale algorithm to solve both the deformation and flow under a common framework.

The current thesis proposes both the block operator splitting method and the multiscale method and presents preliminary analysis of both methods. We test the convergence of the operator splitting method under various material property contrasts and develop a heuristic convergence criterion. For the multiscale method, we first verify a method developed by Chu et al. (2012)[26, 25] for fluid flow in porous media. Two extensions of this method

to solve the the fluid flow and deformation problems in our operator splitting method are also proposed. Numerical experiments are conducted to assess its convergence.

Chapter 2

Literature Review

2.1 Poroelasticity

Central to Biot's formulation are three key assumptions: quasi-static deformation, Terzaghi's Principle, and Increment in Fluid Content η . The quasi-static deformation assumption refers to the idea that we typically neglect temporal derivative terms in the linear elasticity equations, but not in the fluid flow equations. This is because the solid phase of a porous medium usually deforms at significantly slower rates than the fluid flow such that at any one instant in time, the solid equation is in a steady state. Terzaghi's Principle and Increment in Fluid Content are constitutive assumptions made to modify the traditional solid and fluid mechanics equations to account for coupling between the separate physics.

In this section, we summarize the mathematical equations governing poroelastic deformation with careful attention to the relevant conservation laws and coupling parameters.

2.1.1 Solid Deformation

For any open subset V of a solid domain Ω , the total stress σ_{total} acting on the surface ∂V is in opposition to the body forces f internal to V in an equilibrium state. Mathematically, this is written as

$$-\int_{\partial V} \sigma_{total} \cdot \vec{n} dA = \int_V f dV$$

where \vec{n} is the unit outward normal vector. By divergence theorem, we can rewrite this

equation as

$$-\int_{\partial V} \nabla \cdot \sigma_{total} dV = \int_V f dV. \quad (2.1)$$

Since 2.1 is true for any arbitrary volume $V \subseteq \Omega$, we can omit the integrals, leaving the momentum equation

$$-\nabla \cdot \sigma_{total} = f \quad (2.2)$$

In traditional solid mechanics, σ_{total} is a function of solid strain $\epsilon = (\nabla u + \nabla u^T)$ only, where the solid displacement u is independent of time. In deformable porous media, stress u is generally a function of both time and space, leading to temporal changes in σ_{total} given through fluid coupling.

More importantly, the constitutive relation for porous media must be modified to account for both solid strain ϵ and fluid effects. The appropriate constitutive relation is given by Terzaghi's Principle. Terzaghi [64] was the first to illustrate that fluids bear significant loads in porous media, rendering the traditional constitutive relation for solids invalid for porous media. In the one dimensional case, the total measurable stress σ_{total} in a porous medium decreases with increasing pore pressure P , resulting in the relation

$$\sigma_{total} = \sigma_{eff} - p$$

where the effective solid stress σ_{eff} is a function of the strain ϵ . Inspired by similar formulations in thermoelasticity, Biot & Willis [15, 18] extended Terzaghi's principle into multiple dimensions using a symmetric deviatoric stress tensor and by introducing a dimensionless factor $\alpha \in [0, 1]$ to account for the strength of the coupling between flow and deformation, yielding the relation

$$\sigma_{total} = \sigma_{eff} - \alpha p I. \quad (2.3)$$

where I is the identity tensor. The factor α effectively captures the limiting behavior for various media, with $\alpha \rightarrow 0$ for porous media with rigid solid skeletons and $\alpha \rightarrow 1$ for unconsolidated (easily deformable) porous media.

Rice & Cleary[60] reformulated the constitutive relation 2.3 to relate bulk moduli to characterize experimentally observed short and long term behaviors. The short term or *undrained* behavior is characterized by initial no flow conditions under applied loads. The long-term or *drained* behavior is characterized by release of fluid under constant pore pressure conditions. We note that Rice & Cleary's formulation is widely adopted in the geophysical community, while Biot-Willis's formulation is commonly used in the mathematical community.

In the current study, we use the Biot-Willis formulation of the constitutive relation with the standard linear stress-strain relation for effective solid stress. Following [57, 58, 59, 63] we assume the linear solid stress-strain relation

$$\sigma_{eff} = \lambda tr(\epsilon) + 2\mu\epsilon \quad (2.4)$$

with

$$\epsilon \equiv (\nabla u + \nabla u^T). \quad (2.5)$$

Substituting Eqs. 2.3, 2.4 and 2.5 into 2.2, we obtain the solid deformation equation

$$-(\lambda + \mu) \nabla(\nabla \cdot u) - \mu \nabla^2 u + \alpha \nabla p = f \text{ in } \Omega \quad (2.6)$$

As stated earlier, the solid displacement u must necessarily be a function of both space and time with temporal variation obtained from interaction with fluid flow. In the next section, we derive the coupled fluid flow equations.

2.1.2 Fluid Flow

For fluid flows at sufficiently low reynolds numbers, we can neglect momentum effects and use mass conservation alone to model the flow. For any arbitrary volume¹ $V \subseteq \Omega$, the total rate of change of density ρ is the sum of fluid sources g internal to volume V minus the

¹In this case, V is an open subset of Ω .

total mass ejected through the boundary. Mathematically, we write

$$\frac{\partial}{\partial t} \int_V \rho = \int_V g - \int_{\partial V} (v\rho) \cdot n$$

where n is the unit normal to the surface ∂V . Applying divergence theorem, we obtain

$$\frac{\partial}{\partial t} \int_V \rho = \int_V g - \int_V (\nabla \cdot v\rho).$$

As with the deformation equation, since the equation above is true for any arbitrary $V \subseteq \Omega$, we can omit the integrals and write

$$\frac{\partial \rho}{\partial t} = g - (\nabla \cdot (v\rho)).$$

Under the appropriate assumptions², fluid discharge velocity v in porous media is linearly proportional to head h , yielding the so-called Darcy's Law[31]

$$v = \frac{k}{\mu_f} \nabla h$$

where μ_f is the fluid viscosity, and k is the permeability tensor. The term $h = \nabla p + \rho g z$, where p is the fluid pressure, and $\rho g z$ denotes the gravitational flow potential at height z above some given datum. Neglecting gravitational effects, it is henceforth assumed $h = \nabla p$. Substituting Darcy's law into the mass conservation law, we obtain the fluid flow equation

$$\frac{\partial \rho}{\partial t} = -\nabla \cdot \left(\frac{\rho k}{\mu} \nabla p \right) = g \quad (2.7)$$

We note that Darcy's law is only valid under the assumption of negligible deformation of the solid skeleton in porous media. When consolidation processes deform significant volume fractions in porous media, Darcy's law alone is not enough to characterize fluid flow. Terzaghi [64] observed that after initial loading, fluid pressure obeys parabolic diffusion in the one dimensional case. He proposed the consolidation law

$$c_0 \frac{\partial P}{\partial t} = k \frac{\partial^2 P}{\partial z^2}$$

²Steady state, incompressible, single phase laminar, newtonian flow at low reynolds numbers $Re < 10$ in rigid porous media.

where k is positive and c_0 is the non-negative specific constrained storage coefficient. Note that Terzaghi's equation only accounts for fluid effects and does not account for solid-fluid interaction effects.

While Biot [15] was not the first to extend Terzaghi's equation to higher dimensions, he was the first to successfully derive equations for the dynamic interaction fluid pressure and solid deformation. We follow the mixed stiffness formulation[65] of Biot's equations which implicitly assumes that the fluid density ρ in continuity equation 2.7 is scaled by the dimensionless *increment in fluid content* η . Thus, we obtain

$$\frac{\partial(\rho\eta)}{\partial t} = -\nabla \cdot \left(\frac{\rho k}{\mu} \nabla p \right) = g \quad (2.8)$$

We note that η is conceptually similar to *strain* in solid mechanics [35]. Where strain ϵ quantifies changes in length per unit length, increment in fluid content η quantifies the change in fluid volume (from a reference volume) per unit bulk volume[15]. Like strain, the variable η can take on both positive and negative values denoting expansion and contraction conditions, respectively. For incompressible fluids, ρ is a constant and thus can be factored out of all derivative terms in 2.8. In this setting, η can also be interpreted as the increment in porosity per bulk volume. Dividing from both sides of 2.8 by ρ , we obtain

$$\frac{\partial(\eta)}{\partial t} = -\nabla \cdot \left(\frac{k}{\mu} \nabla p \right) = \tilde{g} \quad (2.9)$$

where \tilde{g} is now interpreted as a volumetric source term.

The fundamental assumption in Biot theory[65] is that increment in fluid content η can be modeled as a linear combination of both fluid pressure and volumetric strain $\epsilon_v \equiv \nabla \cdot u$; i.e.

$$\eta = a_1 p + a_2 \epsilon_v. \quad (2.10)$$

The parameters a_1 and a_2 capture the limiting behavior in porous media. Coefficient a_1 is the rate of change in fluid content η per unit pressure under constant strain conditions, i.e. the specific constrained storage coefficient c_0 . The other coefficient $a_2 \equiv \alpha$ is the rate of change in fluid content η per unit strain under constant pressure conditions. Under the

assumption of reciprocity[65, 15], it can be shown that the volume of fluid ejected by an increase in compressive stress under constant pressure conditions is equal to the volumetric expansion due to fluid pressure increase. Hence, the coefficient a_2 must necessarily be equivalent to the Biot-Willis coefficient α found in equation 2.3. Defining $\epsilon_v \equiv \nabla \cdot u$, we can write equation 2.10

$$\eta = c_0 p + \alpha \nabla \cdot u. \quad (2.11)$$

Substituting 2.11 into the modified continuity equation 2.9, we obtain the fluid equation

$$\frac{\partial}{\partial t} (c_0 p + \alpha \nabla \cdot u) = -\nabla \cdot \left(\frac{k}{\mu} \nabla p \right) = \tilde{g} \quad (2.12)$$

Paring Eqs 2.12 and 2.6, we arrive at the coupled partial differential equations

$$-(\lambda + \mu) \nabla (\nabla \cdot u) - \mu \nabla^2 u + \alpha \nabla p = f \text{ in } \Omega \quad (2.13)$$

$$\frac{d}{dt} (c_0 p + \alpha \nabla \cdot u) - \frac{1}{\mu_f} \nabla \cdot (K \nabla p) = h \text{ in } \Omega \quad (2.14)$$

with mixed boundary conditions

$$\begin{aligned} p &= p^*(x) \quad \text{on } \partial\Omega_p \\ \frac{1}{\mu_f} \nabla \cdot (K(x) \nabla p) \cdot n &= q \text{ on } \partial\Omega_f \\ u &= u^*(x) \quad \text{on } \partial\Omega_d \\ \sigma \cdot n &= t_N \text{ on } \partial\Omega_t. \end{aligned}$$

Here, the boundaries $\partial\Omega_p$, $\partial\Omega_f$, $\partial\Omega_d$, $\partial\Omega_t$ refer to the portions of the boundary with fixed pressure, flux, displacement, and traction conditions. Note that Eqs 2.13- 2.14 are fully coupled in pore pressure p and displacement u through the time derivative of fluid content $(c_0 p + \alpha \nabla \cdot u)$.

Since 2.13- 2.14 are time dependent, the system also requires an initial condition $[u(0, x), p(0, x)]^T$. According to [35], the initial condition cannot be chosen arbitrarily and must satisfy certain constraints. In [41], the initial condition is chosen such that the initial increment in fluid content η is zero so that the fluid phase is ejected with finite velocity. Hence, we impose the condition

$$c_0 p + \alpha \nabla \cdot u = 0.$$

at $t = 0$. According to [56], this condition is usually combined with the static equilibrium condition in solid equation 2.13 to produce a unique initial condition.

In the asymptotic limit $t \rightarrow \infty$, the rate of change in fluid content is zero; yielding the *steady state* poroelasticity equations

$$-(\lambda + \mu) \nabla(\nabla \cdot u) - \mu \nabla^2 u + \alpha \nabla p = f \text{ in } \Omega \quad (2.15)$$

$$-\frac{1}{\mu_f} \nabla \cdot k(x) (\nabla p - \rho_f g) = h \text{ in } \Omega \quad (2.16)$$

Since 2.16 is independent of displacement u , the steady state case is a *one way* coupled system of elliptic partial differential equations. This formulation has been successfully applied to estimate heterogeneities in permeabilities over large scale basins in California[2].

2.2 Multiscale Modeling

Classical continuum scale models, such as Biot's Poroelasticity Model, implicitly assume homogeneous material properties such that macroscopic constitutive laws are sufficient to predict the overall behavior of the system. When materials properties are highly heterogeneous, macroscopic constitutive relations are often unknown explicitly or require discretization at scales much smaller than is computationally expedient. The most obvious approach to treat heterogeneity is through Direct Numerical Simulation (DNS); whereby the resolution of the spatial discretization h must necessarily be smaller than the scale of the heterogeneity ϵ . Generally, the domain of interest is many orders of magnitudes larger than the scale of heterogeneity. Of course, this results in time consuming simulations which even the fastest supercomputers on earth cannot handle.

Multiscale modeling emerges from the necessity to balance the two mutually opposing modeling needs that neither macroscopic simulation or direct numerical simulation

can address: detail and efficiency. Multiscale methods can be broadly classified into two categories: Upscaling and Divide & Conquer methods[3]

2.2.1 Upscaling Methods

Upscaling methods replace the heterogeneous material properties in the system by effective macroscopic parameters. Thus, the system is resolved only on the macroscopic grid. Volume Averaging and Asymptotic Homogenization are classical examples of upscaling methods.

In Volume Averaging, the heterogeneous, spatially varying material property $\psi(x)$ at a discrete point x_i of the macroscopic grid is replaced by

$$\bar{\psi}(x_i) = \frac{1}{||V_{x_i}||} \int_{V_{x_i}} \psi(x) dV$$

where V_{x_i} is a window encompassing the point x_i with volume $||V_{x_i}||$. The locally average quantities $\bar{\psi}(x_i)$ can be reduced to a scalar quantity by arithmetic or harmonic average as necessary. Volume Averaging is both intuitive to understand and easy to implement but is insufficient to treat anisotropy or nonlinearities [3].

Homogenization methods treat heterogeneous material properties a_ϵ as a locally periodic quantity that varies in both a slow (x) and fast (y) variable. In the limit as the scale $\epsilon \rightarrow 0$, the oscillations are removed but their coarse scale effects remain. Asymptotic homogenization is based upon the power series expansion

$$u_\epsilon(x) = u_0(x, y) + \epsilon u_1(x, y) + \epsilon^2 u_2(x, y) + \dots$$

where $u_i(x, y)$ are unknown periodic functions in $y = \frac{x}{\epsilon}$. It is expected that $u_\epsilon \rightarrow u_0$ as $\epsilon \rightarrow 0$. For elliptic partial differential equations of the form

$$-\nabla \cdot (a_\epsilon(x, y) \nabla u(x, y)) = f,$$

we substitute the scaled gradient

$$\nabla \equiv \nabla_x + \frac{1}{\epsilon} \nabla_y$$

and the ansatz $u_\epsilon(x)$ into the partial differential equations of the system. Equating like coefficients of ϵ on both sides of the resulting equation, we observe the following:

1. $u_0(x, y)$ is necessarily only a function of the slow variable x . Thus, we write $u_0(x, y) = u_0(x)$.
2. $u_1 = \sum_j \omega_j(x, y) \partial_j u_0(x)$ where ω_j solve locally defined cell problems of the form

$$\nabla_y \cdot [a_\epsilon(x, y) \nabla_y \omega_j(x, y)] = \nabla_y \cdot [a(x, y) e_j] \text{ in } \Omega$$

where ω_j is periodic in y .

3. The original PDE is replaced by the equation

$$\nabla \cdot [a_0 \nabla u_0] = f$$

where the coefficients of the effective tensor a_0 are given as

$$(a_0)_{ij} = \frac{1}{||Y||} \int_Y a(x, y) (\partial_i^y \omega_j(x, y) + \delta_{ij}) dy$$

where Y and $||Y||$ are the local cell domain and volume, respectively.

Asymptotic Homogenization is mathematically rigorous in terms of convergence theory and accuracy, but also has drawbacks. Though the effective coefficient a_0 is obtained from microstructure, the u_0 alone lacks microstructure. $u_0 \not\approx u_\epsilon$. Intuition suggests that since term u_1 contains microstructure information, it could be combined with u_0 to provide a more accurate solution. However, the introduction of u_1 can fail to satisfy local conservation principles[3]. More importantly, it is very difficult to derive a periodic $a(x, y)$ from a general heterogeneous material property $a_\epsilon(x)$. Where heterogeneity is randomly distributed throughout the medium, the periodicity assumption is invalid.

A recent survey of multiscale methods [13] suggests that heterogeneity in poroelasticity is generally resolved by upscaling, with volume averaging being the most common approach due to its relative simplicity in comparison to homogenization. The aforementioned limitations of upscaling approaches motivate the need to develop efficient numerical methods for

heterogeneous poroelastic media. Divide & Conquer type multiscale methods, in general, lend themselves more easily to adapt not only to heterogeneity, but anisotropy as well. For this reason, we focus the remainder of the current thesis on developing a framework for a Divide & Conquer type multiscale method for heterogeneous poroelastic media.

2.2.2 Divide & Conquer Methods

Divide & Conquer methods decompose the macroscopic problem into many small coarse scale subproblems. Within each subproblem, a local solution is obtained by treating the the small scale heterogeneity directly. The local solutions are then coupled to the macroscopic problem and resolved at larger scales. The objective of these methods is to solve a coarse scale problem at a resolution h larger than the scale of heterogeneity ϵ by solving individual subproblems at subresolutions h_{sub} smaller than the scale of heterogeneity ϵ . Multiscale Finite Element/Variational Methods (MSFEM, MSVM), Mortar Methods (MMM) and the Heterogeneous Multiscale Method (HMM) are all examples of the Divide & Conquer strategy and all share a common framework:

1. **Localization:** Decomposition of the domain into coarse elements of scale h such that $h > \epsilon$.
2. **Solution of Subproblems:** Local subproblems are assigned appropriate boundary conditions and solved at a scale h_{sub} such that $h_{sub} < \epsilon$
3. **Coarse-Grid Coupling:** Solutions of local subproblems are used to assemble and solve the problem on the coarse grid of scale h .

One important component of multiscale methods which distinguish it from traditional domain decomposition methods is the notion of *subsampling*. That is, an *efficient* multiscale method never fully coupled to all the scale details, but rather samples the fine scale details in such a way to reduce degrees of freedom while preserving accuracy. Thus, not only

should the coarse grid problem be efficiently solved, but each subproblem must be easily solved with fewer details than traditional domain decomposition methods.

A survey of divide & conquer multiscale methods [66] indicates that a vast majority of multiscale methods apply to single physics simulations (i.e. fluid flow only, solid deformation only, etc.). In the case of poroelasticity, upscaling is the predominant method[13, 51, 34, 23, 48]. Azevedo et al.[6] used statistical scaling relations coupled to a macroscale finite element discretization within a monte carlo algorithm to extract probable effects of fluid injection and extraction. Ladeveze & Nouy[48] employ spatiotemporal homogenization within the so-called LATIN framework. As far as the current author is aware, no domain decomposition methods have been devised specifically for coupled flow and deformation processes in porous media.

The current work follows the Divide & Conquer strategy known as the Heterogeneous Multiscale Framework, which we briefly summarize below.

2.2.3 Heterogeneous Multiscale Method

As described by Weinan E[66], the Heterogeneous Multiscale method is a framework of different methods consisting of an incomplete macroscopic description of the systems behavior whose missing data is supplemented by microscopic simulation. The general methodology consists of four main components:

1. Macroscopic solver - an effective macroscopic description of the systems behavior, often consisting of an incomplete conservation equation and boundary/initial conditions.
2. Restriction operator - a method which projects state variables from the macroscopic domain to local microscopic subdomains, often in the form of boundary and/or initial conditions
3. Microscopic solver - an effective microscopic description of the system behavior, often

consisting of conservation and micro-constitutive relations whose boundary conditions are obtained by the restriction operator.

4. Data Estimator - an effective equation which predicts the data needed to complete the macroscopic conservation equation from local microscopic simulation

2.2.4 Chu et. al.'s Model

The current work is based on a heterogeneous multiscale method for flow in porous media based on Chu et al.[26, 25] with the following components:

1. Macroscopic solver: Finite Volume Method
2. Restriction operator: Linear interpolation
3. Microscopic solver: Direct Stiffness method (pore network models)
4. Data Estimator: Cross-sectional Flux summation

In the following sections, we describe their method in detail.

Microscale Model

The microscale model is a discretization of the void space within a porous medium into a network of cylindrical pipes (throats) and spherical chambers (pores) [36]. In this context, the network forms a discrete graph of nodes and edges, known as a Pore Network (PN) Model. The topology of the network can be structured or unstructured, as needed to model a particular porous medium. Figure 1 illustrates a structured network with constant throat lengths.

For incompressible fluids, imposing mass conservation at each pore i results in conser-

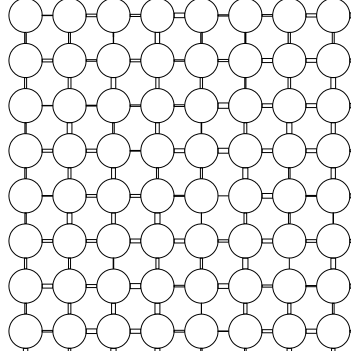


Figure 2.1: A structured 8x8 microscale network model with constant pore size and random throat radii.

vation of volumetric flux given by

$$\sum_{j \in K_i} q_{ij} = s_i \quad (2.17)$$

$$q_{ij} = g_{ij}(\Delta P_{ij}) \quad (2.18)$$

where q_{ij} represents the volumetric flow rate from pore i to pore j , K_i denotes the set of all pores connected to pore i , and g_{ij} is the hydraulic conductance, which is a function of the pressure difference ΔP_{ij} between pores i and j , and s_i is an internal volumetric source term. In the laminar newtonian flow case, the function g_{ij} is given by the linear Hagen-Poiseuille relation:

$$g_{ij}(\nabla P_{ij}) = \frac{\pi r_{ij}^4}{8\mu L_{ij}} \nabla P_{ij} \quad (2.19)$$

where r_{ij} , L_{ij} , and μ are the throat radii, throat lengths, and fluid viscosity, respectively. Though g_{ij} is presented as a linear function here, it may be a non-linear for other fluids or flow regimes.

The equations given by (1), (2), and (3) result in the linear system:

$$[C]p = b \quad (2.20)$$

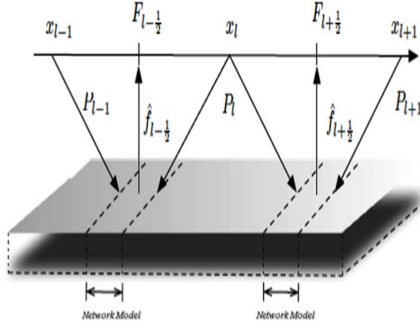


Figure 2.2: Macroscale-microscale model coupling, adapted from [26, 25]

where C is the conductance matrix, p is the pressure, and b represents the vector containing boundary conditions. Typically, two opposite faces of the network model are defined as the axial boundaries with dirichlet conditions. The remaining boundary faces in the network model are defined as the transverse boundaries. Periodic conditions are imposed on the transverse boundaries for strongly isotropic materials, but alternative boundary conditions have been developed for anisotropic conditions[26, 25].

Macroscopic Model

At the continuum scale, the mass conservation principle for incompressible fluids is governed by

$$\nabla \cdot v = S(x) \quad (2.21)$$

where v is the bulk flow velocity and S represents source/sink terms. The standard Darcy model of fluid flow assumes $v = \kappa \nabla P$, where P and κ are the macroscopic pressure and permeability, respectively. The current study follows [26, 25] by assuming no explicit form of v . Instead, v is implicitly assumed as a function of position, pressure and pressure gradient. That is, $v = v(x, P, \nabla P)$.

The Finite Volume (FV) discretization of (4) results in dual grids representing the macroscopic pressures and fluxes of representative control volumes as seen in Figure 2.

The divergence theorem³ applied to the one dimensional discretization of (3) results in:

$$F_{i+\frac{1}{2}} - F_{i-\frac{1}{2}} = S(x_i)\Delta x \quad (2.22)$$

where $F_{i+\frac{1}{2}}$ represents the volumetric flux through the boundaries of the control volumes.

Iterative Coupling Algorithm

The key to coupling the two models above is a reformulation of the macroscopic flux in terms of both microscopic flux *and* macroscopic pressure. In [26, 25], the coupling is achieved primarily through the assumption that $F = 0$ when $\nabla P = 0$. In the one dimensional case where ∇P is a scalar quantity, the mean value theorem implies that there exists ξ such that

$$\frac{F(x, P, \xi)}{d\nabla P} = \frac{F(x, P, \nabla P) - F(x, P, 0)}{\nabla P - 0} \quad (2.23)$$

or equivalently

$$F(x, P, \nabla P) = \frac{F(x, P, \xi)}{d\nabla P} \nabla P \quad (2.24)$$

where ξ is between 0 and ∇P . We note that the macroscopic model requires the evaluation of the flux F at the point $x_{i+\frac{1}{2}}$. Thus, the quantity $\frac{dF(x_{i+\frac{1}{2}}, P, \xi)}{d\nabla P}$ is estimated as

$$\frac{dF(x_{i+\frac{1}{2}}, P, \xi)}{d\nabla P} \approx \frac{F_{i+\frac{1}{2}}(x_{i+\frac{1}{2}}, P, \nabla P) - F_{i+\frac{1}{2}}(x_{i+\frac{1}{2}}, P, 0)}{\nabla P - 0} = \frac{F_{i+\frac{1}{2}}(x_{i+\frac{1}{2}}, P, \nabla P)}{\nabla P} \quad (2.25)$$

with $\nabla P \approx \frac{P_{i+\frac{1}{2}}^R - P_{i+\frac{1}{2}}^L}{\delta}$, where $P_{i+\frac{1}{2}}^R$ and $P_{i+\frac{1}{2}}^L$ are the interpolated dirichlet boundary conditions on the network model centered at $x_{i+\frac{1}{2}}$ with length δ . Assuming linear interpolation of the boundary conditions from the macroscopic pressure values, we replace $\nabla P \approx \frac{P_{i+\frac{1}{2}}^R - P_{i+\frac{1}{2}}^L}{\delta}$ by the discrete forward difference operator $D^+[P_i] \equiv \frac{P_{i+1} - P_i}{\Delta x}$. Hence, we can define an effective macroscopic coefficient $K_{i+\frac{1}{2}}$ as

$$-K_{i+\frac{1}{2}}(P_i, P_{i+1}) \equiv \frac{F_{i+\frac{1}{2}}(x_{i+\frac{1}{2}}, P, \nabla P)}{D^+[P_i]}$$

³See [26, 25] for higher dimensional schemes.

and

$$F_{i+\frac{1}{2}}(x_{i+\frac{1}{2}}, P_i, P_{i+1}) = -K_{i+\frac{1}{2}}(P_i, P_{i+1})D[P_i] \quad (2.26)$$

where $D[\cdot]$ is a difference operator and $K_{i+\frac{1}{2}}$.

Substituting $F_{i+\frac{1}{2}}$ into the macroscopic equation 2.22, we obtain

$$D \left[\frac{f_{i+\frac{1}{2}}(P_i, P_{i+1})}{D^+[P_i]} D[P_i] \right] = S_i \quad (2.27)$$

We note that the formulation 2.27 is sufficiently general enough to handle both linear and non-linear fluxes. Hence, 2.27 is, in general a system of non-linear equations which can be solved by fixed point iteration⁴ or by quasi-newton methods [26, 25]. Hence, the iteratively coupled multiscale model is linearized as:

$$D^- \left[\frac{f(P_i^{(n)}, P_{i+1}^{(n)})}{D^+[P_i^{(n)}]} D^+[P_i^{(n+1)}] \right] = S_i \quad (2.28)$$

$$[C_{i+\frac{1}{2}}]p_{i+\frac{1}{2}} = b_{i+\frac{1}{2}} \text{ for } i = 0, \dots, n. \quad (2.29)$$

The algorithm iterates between micro and macro scale models until some convergence criteria is satisfied. In [26, 25], Chu et. al. prove this multiscale system has analogous convergence rates as multiscale homogenization in the linear case. We note that the formulation presented is independent of the linearity assumptions on the velocity. Chu et al. proceed to demonstrate this model's applicability to non-linear constitutive relations at the microscale in [26, 25].

2.3 Operator Splitting

Poroelasticity falls into the broader category of coupled multiphysics problems defined by systems of partial differential equations describing the interaction between two or more field variables. Multiphysics problems differ from general mixed PDE formulations in that

⁴Convergence of the fixed point iteration from any starting value is established in [26, 25]

”neither domain can be solved separately from each other [and] neither set of dependent variables can be explicitly eliminated” [69]. Coupled problems are further classified into two categories based on the degree of domain overlap where the state variables are defined[71].

Type I problems (also known as Interfacial Problems) are characterized by systems of equations whose dependent variables lie on separate, non-overlapping domains and with interaction occurring solely through domain interfaces. Fluid-structure interaction is a typical Type I problem where the interface divides the regions where the distinct media and their governing partial differential equations are valid. As they are dynamic problems, interfacial displacement is tracked through additional time dependent mesh variables and equations into Type I systems. Kumar [47] characterized discretized systems of equations for fluid-structure interaction in terms of dynamic structure u_s , mesh u_m , and fluid u_f variables. The system of equations is summarized as

$$\begin{cases} \vec{N}_s(u_s, u_m, u_f) = 0 \\ \vec{N}_m(u_s, u_m, u_f) = 0 \\ \vec{N}_f(u_s, u_m, u_f) = 0 \end{cases} \quad (2.30)$$

where \vec{N}_s , \vec{N}_m , and \vec{N}_f are the (typically non-linear) equations governing the structure u_s , mesh u_m , and fluid u_f variables, respectively.

Type II problems (also known as Overlapping Problems) are those systems whose dependent variables lie on partially or totally overlapping domains. Thermo-structure interaction is a typical Type II problem where the state variables of temperature, stress, and strain interact within the same medium. In contrast to Type I problems, Type II problems do not require additional terms to account for dynamic mesh displacement, even when the coupling is strong. In the context of fluid-solid coupling, equations 2.30 reduce to the simplified form:

$$\begin{cases} \vec{N}_s(u_s, u_f) = 0 \\ \vec{N}_f(u_s, u_m, u_f) = 0 \end{cases}$$

After temporal and spatial discretization, Biot’s poroelasticity equations 2.13-2.14 form a saddle point system of the form:

$$\begin{bmatrix} A & B^T \\ B & -C \end{bmatrix} \begin{bmatrix} u \\ p \end{bmatrix}^{t+1} = \begin{bmatrix} f \\ g \end{bmatrix}^{t+1} \quad (2.31)$$

at each timestep t , where A, B, C are symmetric positive definite. Matrix systems of this form are saddle point problems whose spectrum contains both positive and negative eigenvalue[12].

2.3.1 Fractional Step Methods

The rationale behind operator splitting methods is that fully coupled time dependent dynamics can be decomposed into the superposition of the individual operators corresponding to separate physical processes, such as diffusion, advection, reaction, etc. Fractional splitting methods apply easily to hyperbolic differential equations of the form

$$y_t = (A + B)y \quad (2.32)$$

where A and B are differential operators. The various splitting methods resolve this ODE by solving a sequence of subproblems composed of each individual operator over a fixed number of iterations with or without predictor-corrector adjustments between each iteration. For example, Lie-Trotter Splitting is a first order accurate method requiring the solution of two subproblems alternately applying each operator within a single timestep:

$$\frac{y^* - y_t}{\Delta t} = Ay^t \quad (2.33)$$

$$\frac{y_{t+1} - y^*}{\Delta t} = By^* \quad (2.34)$$

Other methods, such as Strang Splitting, achieve higher order accuracy by advancing over partial timesteps between t and $t + 1$ while alternating between operators. In general, fractional step methods are not guaranteed to converge in a fixed number of iterations despite stable time-stepping discretization[46].

Poroelectricity equations cannot be converted into the form 2.32 except in the particular case where $c_0 \equiv 0$. In this case, Gaspar et al[38] showed that it can be transformed into

an alternative form which was amenable to a specialized fractional step method. The key to their work was the application of additional differential operators to the flow and deformation equations to eliminate certain terms in the equations. Introducing new variables for the pressure laplacian $q = -\Delta p$ and deformation velocity $v = \frac{du}{dt}$, they resolved the poroelasticity equations by solving a sequence of subproblems⁵ within each timestep in the following order:

$$\frac{q^{t+1} - q^t}{\Delta t} - (\lambda + 2\mu)k\nabla^2 q^{t+1} = -(\lambda + 2\mu)\nabla^2 f^{t+1} \quad (2.35)$$

$$-\nabla^2 p^{t+1} = q^{t+1} \quad (2.36)$$

$$-\mu\nabla^2(\nabla \cdot v^{t+1}) + \nabla \left(\frac{p^{t+1} - p^t}{\Delta t} \right) + (\lambda + 2\mu)k\nabla q^{t+1} = (\lambda + \mu)\nabla f^{t+1} \quad (2.37)$$

In the general case where $c_0 \neq 0$ is not easily amenable to the above approach. The general quasi-static poroelasticity problem is denoted by

$$Au = 0 \text{ for deformation} \quad (2.38)$$

$$Bu_t + Cu = 0 \text{ for flow} \quad (2.39)$$

In this form, the problem cannot be transformed into the canonical form established by 2.32. Consequently, alternative splitting methodologies have been developed.

2.3.2 Kim et al's work

Motivated by an industrial need to enable highly optimized legacy codes and solvers for individual flow and deformation equations, Kim[46] analyzed four operator splitting strategies for a non-linear formulation of the poroelasticity equations for multiphase flow & deformation. His approach decomposes the coupled system into solutions of single set of equations for flow or deformation at a time. When necessary, he used pressure and displacement predictor/corrector methods which impose the respective conservation principles.

⁵With appropriately adjusted boundary conditions and additional stabilization techniques.

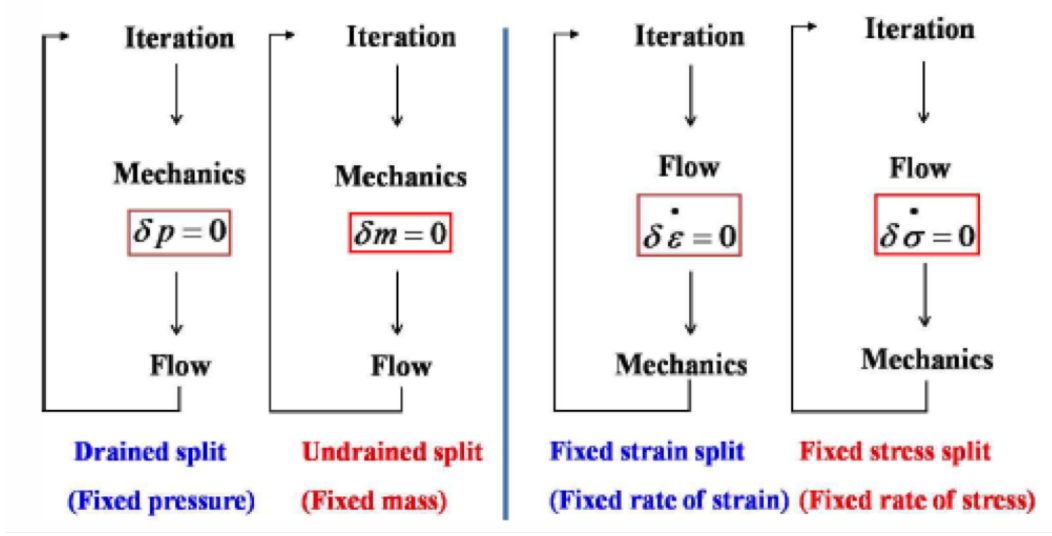


Figure 2.3: Visualization of the four operator splitting methods developed by Kim[46].

The Drained Splitting method solves the deformation problem first by holding the pressure constant and consequently solving fluid flow using the updated deformations. The Undrained Splitting method imposes constant fluid mass while the deformation equation is resolved, requiring an additional pressure correction. Fixed Strain Splitting method solves the flow equation first, holding the volumetric strain constant. The updated pressures are then used to resolve the deformation equation. Like the drained splitting method, no additional predictor/corrector is used to update the pressures. Finally, the fixed stress splitting method also resolves the fluid equation first, but holds the total mean rate of stress constant such that the volumetric stress is automatically computed.

Kim[46] derived stability criteria for the drained, undrained, fixed strain and fixed stress splittings as well as the fully coupled problem by Von Neumann Analysis. They noted that drained and fixed strain splittings (i.e. the methods which did not employ predictor-corrector adjustments) have a stability criterion related to the ratio of the bulk stiffnesses of the fluid and solid skeleton. On the other hand, the undrained, fixed stress, and fully coupled methods were unconditionally stable.

He further tested and verified their applications to four specific test cases including

Terzaghi’s and Mandel’s problem as mentioned in chapter 1. Furthermore, he observed that drained and fixed strain splittings were inconsistent if limited to a fixed number of iterations. That is, if not permitted to iterate until convergence, these two methods become inconsistent over time. Though both undrained and fixed stress splitting are unconditionally stable, fixed stress splitting required fewer iterations than undrained splittings for the cases tested. Furthermore, we note that Kim’s stability work assumed constant parameter values which are not necessarily applicable to the variable coefficient case.

2.4 Summary

In summary, Biot’s poroelasticity equations are a system of linear PDE’s which describe the interaction between flow and deformation in porous media. While analytical solutions exist, there is no general solution to Biot’s Equations. The mathematical properties of Biot’s equations have been well researched and many numerical methods have been developed to solve them.

In many realistic media, highly variable material properties exist which make efficient and accurate simulation results extremely difficult to achieve with traditional continuum scale numerical methods. Multiscale methods balance the need for accuracy by efficient use of a small sample of microscopic information. The two main classes of multiscale methods are Upscaling and Divide & Conquer methods, with the former being the dominant method used for poroelasticity applications of heterogeneous nature. As far as the current author is aware, no multiscale methods of the Divide & Conquer type have been developed for Biot’s equations.

A large body of multiscale algorithms exist which only apply to elliptic partial differential equations. A methodology to capitalize on decades worth of multiscale algorithms would enable highly accurate solutions to the multiscale poroelasticity equations and their applications.

Consequently, the focus of the remainder of this thesis is on the development of a Divide

& Conquer type multiscale method for Biot's poroelasticity equations. In our approach, we develop an operator splitting method which resolves each timestep as a sequence of elliptic problems. Our algorithm is sufficiently generalizable such that any feasible multiscale method could potentially be utilized. In particular, the current thesis also proposes a single method to resolve the two resulting multiscale elliptic PDE's solution by means of a modification of the method established by Chu et al.[26, 25]'s. The details of these methods are elaborated in the following section.

Chapter 3

Methodology

3.1 Assumptions

To begin the process of developing a multiscale method for Biot's equations, we make several assumptions to the standard quasi-static formulation of the linear poroelasticity equations[63]. Firstly, for simplicity, we restrict our attention to the 1D formulation of Biot's equations 2.13- 2.14 in the spatial domain $\Omega \equiv [0, L]$ with no source terms:

$$-\frac{d}{dx} \left((\lambda + 2\mu) \frac{du}{dx} \right) + \alpha \frac{dp}{dx} = 0, \quad x \in \Omega \quad (3.1)$$

$$\frac{d}{dt} \left(c_0 p + \alpha \frac{du}{dx} \right) - \frac{1}{\mu_f} \frac{d}{dx} \left(k \frac{dp}{dx} \right) = 0, \quad x \in \Omega. \quad (3.2)$$

The boundary conditions are imposed as fixed values

$$p = p_L \quad \text{at } x = 0 \quad (3.3)$$

$$(\lambda + 2\mu) \frac{du}{dx} = -T_L \quad \text{at } x = 0 \quad (3.4)$$

$$u = u_R \quad \text{at } x = L \quad (3.5)$$

$$\frac{1}{\mu_f} k \frac{dp}{dx} = F_R \quad \text{at } x = L \quad (3.6)$$

where and $p_L, t_L, u_R, f_R \geq 0$. We also impose a finite the initial condition satisfying

$$c_0 p + \alpha \frac{du}{dx} = 0 \quad \text{at } t = 0. \quad (3.7)$$

Note in the situation where $p_L = u_R = f_R = 0$ and $\lambda, \mu, c_0, \alpha, \mu_f$ & k are constant, equations 3.1- 3.7 are equivalent to the classic Terzaghi Problem where a constant (compressive) load t_L is suddenly applied to the top ($x = 0$) of a column of fluid-saturated

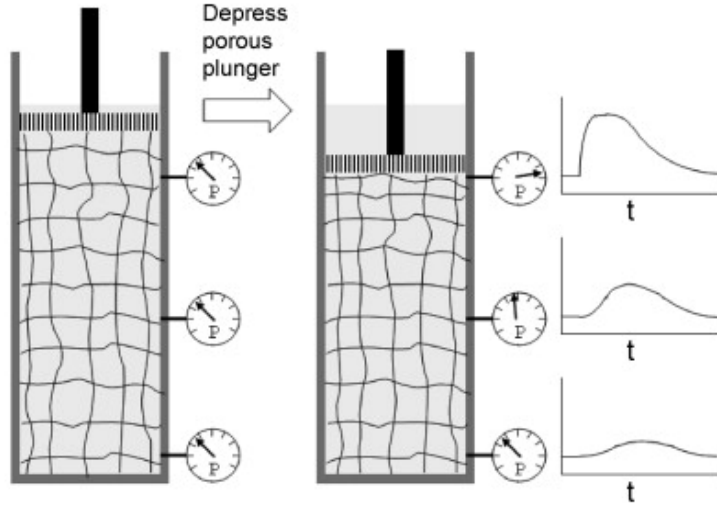


Figure 3.1: Depiction of the 1D Terzaghi Problem, adapted from Mitchison et. al.[52]

porous medium of finite length. The load is induced by a permeable plunger or piston such that fluid drains through the top boundary as shown in figure 3.1. Due to draining conditions, the top of the medium is also subject to zero excess pore pressure conditions. The dirichlet and neumann conditions at $x = 1$ model the situation that the bottom of the medium is both rigid and impermeable, respectively. The medium is constrained in the transversal directions by a rigid container such that it is subject only to uniaxial strain[65]. The initial condition captures the fact that there is no increment in fluid content upon initial loading.

Next, we assume the lame parameters λ , μ and permeability k in equations 3.1- 3.2 vary in space but not in time. We further assume that these variable material parameters are highly heterogeneous, but not necessarily periodic. More precisely, we assume $\lambda(x)$, $\mu(x)$ and $k(x)$ are continuous functions with sharp gradients of positive characteristic length $\epsilon \ll 1$ distributed randomly within the computational domain Ω . All other material parameters are assumed to be constant. Consequently, we model λ , μ , and k as functions

of x and rewrite equations 2.13- 2.14 as:

$$-\frac{d}{dx} \left(\nu(x) \frac{du}{dx} \right) + \alpha \frac{dp}{dx} = 0, \quad x \in \Omega \quad (3.8)$$

$$\frac{d}{dt} \left(c_0 p + \alpha \frac{du}{dx} \right) - \frac{d}{dx} \left(K(x) \frac{dp}{dx} \right) = 0, \quad x \in \Omega \quad (3.9)$$

with $\nu(x) = \lambda(x) + 2\mu(x)$ and $K(x) = \frac{k(x)}{\mu_f}$.

Due to the heterogeneity encapsulated in ν and K , equations 3.8- 3.9 cannot be accurately resolved by conventional continuum methods without an extremely small spatial discretization $h < \epsilon$. To resolve this issue, we first propose an operator splitting strategy which resolves equations 3.8- 3.9 as a sequence of two uncoupled elliptic PDE's. Then, we propose a heterogeneous multiscale method which resolves both elliptic equations by a common framework.

3.2 Operator Splitting

To decouple equations 3.8- 3.9, we follow Rothe's semi-discretization methodology using a backward euler finite difference in time t while leaving the spatial variable x and its corresponding operators continuous. This results in the implicit semi-discrete equations

$$-\frac{d}{dx} \left(\nu(x) \frac{du^t}{dx} \right) + \alpha \frac{dp^t}{dx} = 0, \quad x \in \Omega \quad (3.10)$$

$$\left(c_0 \frac{p^t - p^{t-1}}{\Delta t} + \alpha \frac{\frac{du^t}{dx} - \frac{du^{t-1}}{dx}}{\Delta t} \right) - \frac{d}{dx} \left(K(x) \frac{dp^t}{dx} \right) = 0, \quad x \in \Omega \quad (3.11)$$

where t is the discrete time step and Δt is the temporal increment. Note that all terms $t - 1$ are known quantities in the t th timestep and thus can be treated as source terms.

Hence, we rewrite equations 3.10- 3.11 as

$$-\frac{d}{dx} \left(\nu(x) \frac{du^t}{dx} \right) + \alpha \frac{dp^t}{dx} = 0, \quad x \in \Omega \quad (3.12)$$

$$\left(\frac{c_0}{\Delta t} p^t + \frac{\alpha}{\Delta t} \frac{du^t}{dx} \right) - \frac{d}{dx} \left(K(x) \frac{dp^t}{dx} \right) = R^{t-1}, \quad x \in \Omega \quad (3.13)$$

where $R^{t-1} = \frac{c_0}{\Delta t} p^{t-1} + \frac{\alpha}{\Delta t} \frac{du^{t-1}}{dx}$.

Introducing new notation, we define four continuous linear operators A, G, D , and B as follows:

$$Au \equiv -\frac{d}{dx} \left(\nu(x) \frac{du}{dx} \right) \quad (3.14)$$

$$Gp \equiv \alpha \frac{dp}{dx} \quad (3.15)$$

$$Du \equiv \frac{\alpha}{\Delta t} \frac{du}{dx} \quad (3.16)$$

$$Bp \equiv \frac{c_0}{\Delta t} p - \frac{d}{dx} \left(K(x) \frac{dp}{dx} \right) \quad (3.17)$$

Then, we can rewrite equations 3.12- 3.13 in terms of a single linear system $Lv^t = b$, where

$$L \equiv \begin{bmatrix} A & G \\ D & B \end{bmatrix}, \quad v^t \equiv \begin{bmatrix} u^t \\ p^t \end{bmatrix}, \quad b \equiv \begin{bmatrix} 0 \\ R^{t-1} \end{bmatrix} \quad (3.18)$$

We shall refer to system 3.18 as the fully coupled semi-discrete equations. Note that in this formulation, u and p are continuous variables coupled to each other only at the current timestep. To uncouple these equations, we apply the method of successive approximations¹ by formulating a sequence of approximations which resolve the current iterate $u^{t,n}, p^{t,n}$ in terms of the previous iterate $u^{t,n-1}, p^{t,n-1}$. We propose two different decoupling methods motivated by block operator decompositions of L .

3.2.1 Block Jacobi Splitting

In the Block Jacobi Splitting method, we formulate a sequence of approximations $v^{t,n} \equiv [u^{t,n}, p^{t,n}]^T$ by decomposing the operator L as a sum of the its diagonal and off-diagonal components. That is, we write $L = M + N$ where

$$M \equiv \begin{bmatrix} A & 0 \\ 0 & B \end{bmatrix}, \quad N \equiv \begin{bmatrix} 0 & G \\ D & 0 \end{bmatrix} \quad (3.19)$$

¹Also known as Fixed Point Iteration or Picard Iteration.

Hence, system 3.18 is rewritten as

$$Mv^t + Nv^t = b. \quad (3.20)$$

Next, we apply a fixed point iteration such that all instances of u^t in equation 3.12 and all instances of p^t in equation 3.13 use the current iterate n . All other (off-diagonal) terms use the previous iterate $n - 1$. Consequently, the solution at each timestep t is resolved by the system

$$Mv^{t,n} + Nv^{t,n-1} = b. \quad (3.21)$$

or equivalently

$$-\frac{d}{dx} \left(\nu(x) \frac{du^{t,n}}{dx} \right) = S_p^{t,n-1}, \quad x \in \Omega \quad (3.22)$$

$$\frac{c_0}{\Delta t} p^{t,n} - \frac{d}{dx} \left(K(x) \frac{dp^{t,n}}{dx} \right) = S_u^{t,n-1} + R^{t-1}, \quad x \in \Omega. \quad (3.23)$$

where $S_p^{t,n-1} \equiv \alpha \frac{dp^{t,n-1}}{dx}$ and $S_u^{t,n-1} \equiv \frac{\alpha}{\Delta t} \frac{du^{t,n-1}}{dx}$.

3.2.2 Block Gauss-Seidel Splittings

The Block Gauss-Seidel Splitting method uses a block operator decomposition of the form $L = M + N$ where M is either the block lower or upper triangular portions of L while N contains the remaining blocks of L . When M is the block lower triangular, we obtain a splitting similar in scope to Kim's Drained Splitting method[46], where

$$M \equiv \begin{bmatrix} A & 0 \\ D & B \end{bmatrix}, \quad N \equiv \begin{bmatrix} 0 & G \\ 0 & 0 \end{bmatrix} \quad (3.24)$$

Alternatively for M upper triangular, the resulting Block Gauss-Seidel method is similar to Kim's Fixed Strain splitting method[46], where

$$M \equiv \begin{bmatrix} A & G \\ 0 & B \end{bmatrix}, \quad N \equiv \begin{bmatrix} 0 & 0 \\ D & 0 \end{bmatrix} \quad (3.25)$$

Substituting for L and applying fixed point iteration, we again arrive at the system

$$Mv^{t,n} + Nv^{t,n-1} = b. \quad (3.26)$$

In the upper triangular case, all instances of u^t and p^t in equation 3.13 and all instances of u^t in equation 3.13 use the current iterate. The remaining term p^t in equation 3.12 uses the previous iterate. The block lower Gauss-Seidel splitting can alternatively be formulated as

$$-\frac{d}{dx} \left(\nu(x) \frac{du^{t,n}}{dx} \right) + \alpha \frac{dp^{t,n-1}}{dx} = 0, \quad x \in \Omega \quad (3.27)$$

$$\left(\frac{c_0}{\Delta t} p^{t,n} + \frac{\alpha}{\Delta t} \frac{du^{t,n}}{dx} \right) - \frac{d}{dx} \left(K(x) \frac{dp^{t,n}}{dx} \right) = R^{t-1}, \quad x \in \Omega. \quad (3.28)$$

Analogously, the block upper Gauss-Seidel splitting can be written as

$$-\frac{d}{dx} \left(\nu(x) \frac{du^{t,n}}{dx} \right) + \alpha \frac{dp^{t,n}}{dx} = 0, \quad x \in \Omega \quad (3.29)$$

$$\left(\frac{c_0}{\Delta t} p^{t,n} + \frac{\alpha}{\Delta t} \frac{du^{t,n-1}}{dx} \right) - \frac{d}{dx} \left(K(x) \frac{dp^{t,n}}{dx} \right) = R^{t-1}, \quad x \in \Omega. \quad (3.30)$$

Although both block Gauss-Seidel splittings are not entirely decoupled, one of the two resulting equations at each iteration is always independent of a state variable. Thus for each iteration n , one equation is solved for one variable and its solution is incorporated as a source term in the other equation.

3.2.3 Convergence

Clearly, both Block Jacobi and Gauss-Seidel strategies compute the solution at each timestep $[u^t, p^t]^T$ coupled semi-discrete system as a sequence of two PDE's of the form

$$-\frac{d}{dx} \left(\nu(x) \frac{du}{dx} \right) = f, \quad (3.31)$$

$$\frac{c_0}{\Delta t} p - \frac{d}{dx} \left(K(x) \frac{dp}{dx} \right) = g \quad (3.32)$$

In the Block Jacobi case, f and g are independent of u and p . In the Block Gauss-Seidel case, f is independent of u and p , but g is a function² of u . Note that equation 3.31 is

²In particular, g is a function of $\frac{du}{dx}$

an elliptic diffusion equation while 3.32 is an elliptic reaction-diffusion equation. Since our decomposition method does not yet assume a particular spatial discretization, we conjecture that any numerical method can be applied to 3.31- 3.32. However, the numerical method must satisfy certain criteria in order to ensure convergence. In particular, Banach's fixed point theorem suggests that if the mapping $v^{t,k-1} \rightarrow v^{t,k}$ is a contraction, then the sequence of iterations converges.

For a given splitting $L = M + N$, we can write the split system as $Mv^t = -Nv^t + b$ and denote the functional $F(v) \equiv M^{-1}(-Nv + b)$. The functional iteration is expressed in the form $v^n = F(v^{n-1})$. According to Banach's fixed point theorem, the iteration converges if for any v_1 and v_2 in the domain of F ,

$$\|F(v_1) - F(v_2)\| \leq q\|v_1 - v_2\| \quad (3.33)$$

for some $0 < q < 1$. Note that 3.33 is sufficiently generalizable to continuous and discrete operators. If equations 3.31- 3.32 are discretized on a macroscopic equispaced grid of interval length Δx , then operators M and N are linear matrices and theorem 3.33 is automatically satisfied if $\|M^{-1}N\| < 1$. In this case, the sequence of iterates v^k approaches the exact solution v^* at a rate closely related to the spectral radius ρ of $M^{-1}N$. Furthermore, the fixed point iteration converges faster as $\rho \rightarrow 0$ and slower as $\rho \rightarrow 1$.

Note that convergence is not guaranteed for all combinations of material parameters and spatiotemporal discretizations. Also, convergence is not guaranteed for a fixed number of iterations as described by Kim[46]. The principal advantage of the proposed method is that the solution to the coupled poroelasticity equations at each timestep is decomposed into the solution of a sequence of elliptic diffusion and elliptic reaction diffusion equations with multiscale coefficients for which many multiscale algorithms are readily available. Moreover, as many of these methods are iterative in scope, they can be more readily implemented in this particular form.

While a thorough comparative analysis of various multiscale methods for equations in each operator splitting strategy is beyond the scope of this thesis, we develop a particular

heterogeneous multiscale method based on the framework established by Chu et al.[26, 25] and applicable to both equations. Details of this method are elaborated in the next section.

3.3 Generalization of Chu et al.’s Multiscale Method

Clearly, the two resulting elliptic PDE’s derived from our operator splitting strategy can be generalized into the form

$$\nabla \cdot \Phi(x, \Psi, \nabla \Psi) + h(\Psi) = S(x) \quad (3.34)$$

where Φ denotes a function of a state variable Ψ & its gradient $\nabla \Psi$, $S(x)$ denotes a source term, and $h(\Psi)$ is a linear function of the state variable. When $h(\Psi)$ is identically zero, we obtain the elliptic diffusion equation which describes the solid deformation equation. The flow equation is obtained by setting $h(\Psi) = c^*P$ where c^* is a constant which depends on given material parameters and the chosen time stepsize Δt .

In a recent paper[33], the current author established that the fundamental assumptions inherent to Chu et al.’s multiscale algorithm are applicable not only to steady state fluid flow in porous media, but also solid deformation and steady state heat transfer as well. More importantly, the microscale pore network model used in Chu et al.’s algorithm belongs to a much more general class of finite element methods known as Direct Stiffness Methods. In the solid deformation case, [33, 32], direct stiffness methods can be incorporated into the Chu et al.’s multiscale framework both in the single[33] and higher dimensional cases.

In the context of the operator splitting method as outlined in the previous section, we note two main observations about Chu et al.’s original algorithm. While it was verified as a tool for fluid flow in porous media, it has never been verified as a tool to model solid deformation. Also, while it was developed under the assumption of an elliptic diffusion equation as in the solid deformation equation 3.31, it has not been tested on an elliptic reaction-diffusion equation. Specifically, it has never been applied to solve the fluid flow equation described by the 3.32.

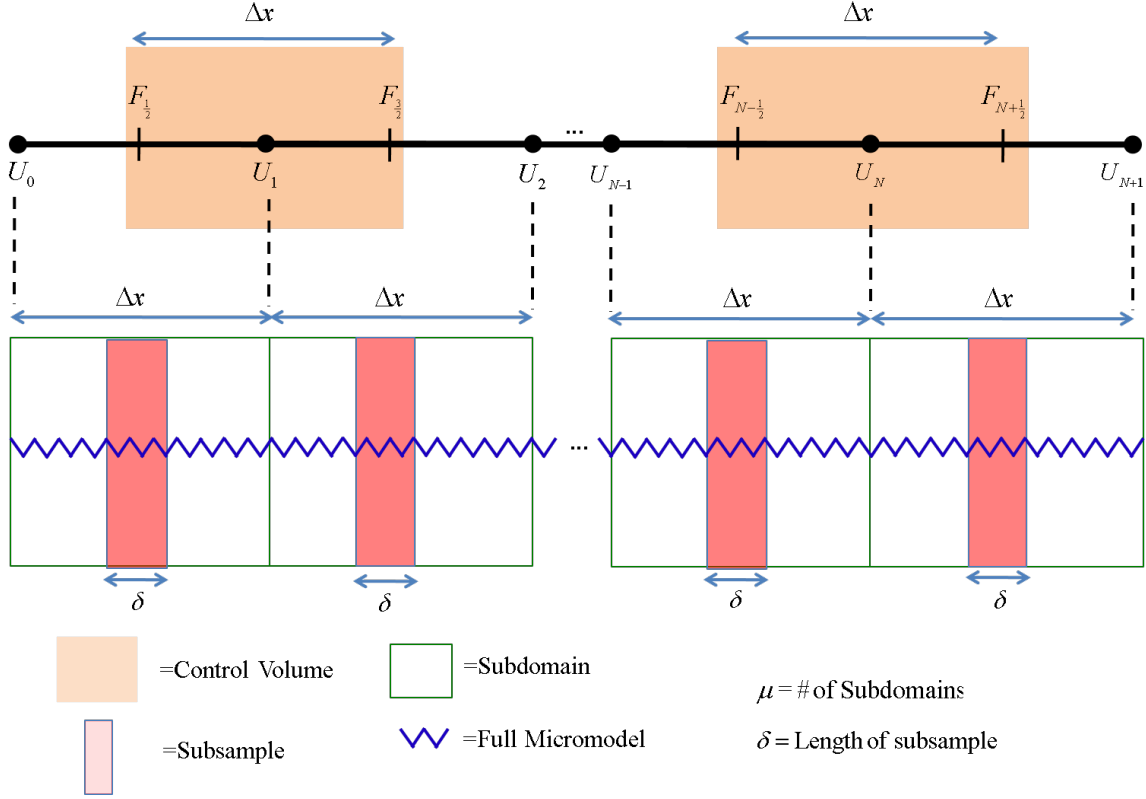


Figure 3.2: Visualization of the heterogeneous multiscale model sampling the fully microscopic model. In the fluid flow case, the fully microscopic model is a network model of pores and throats. In the solid deformation case, it is an assemblage of spring elements using in a direct stiffness model.

Hence, this thesis also addresses both the verification of Chu et al.'s multiscale method in the context of solid deformation in the form 3.31 and proposes an extension of this method to handle the fluid flow equation 3.32. Both proposed methods are based on coupling the Finite Volume Method at the continuum scale with a Direct Stiffness Finite Element [49, 14] at the microscale. Details of these two models are summarized in the same macroscopic framework described in the next section, with the two separate cases of fluid flow and solid deformation handled by distinct microscopic models.

3.3.1 Macroscopic Model

Using equation 3.34, we apply the finite volume method by discretizing the domain Ω into finitely many equispaced cells $B_i = [x_{i-\frac{1}{2}}, x_{i+\frac{1}{2}}]$ with discrete values of Ψ defined at the cell center x_i . Integrating this equation over each control volume B_i and applying the divergence theorem, we obtain an expression of the form

$$\hat{\Phi}_{i+\frac{1}{2}} - \hat{\Phi}_{i-\frac{1}{2}} + h(\Psi_i)\Delta x = \hat{F}_i\Delta x. \quad (3.35)$$

where $\hat{\Phi}_{i+\frac{1}{2}} \equiv \Phi_{i+\frac{1}{2}}\Delta A$, with ΔA denoting the cross-sectional area of the control volume. The variables Ψ and Φ have different interpretations corresponding to the flow and deformation problems. For fluid flow, the variable Ψ and Φ represent the macroscopic pressure P and flux F . For solid deformation, displacement U and total boundary force \tilde{F} are represented by Ψ and Φ , respectively. The fractional indices in 3.35 indicate that conserved quantities are defined on the boundary of control volume, while integer indices denote cell centered values. In its current form, equation 3.35 is incomplete because no explicit macroscopic constitutive relation is known or assumed.

The key assumption to couple macro and micro spatial scales in [26, 25] is that the volumetric flux is zero when the pressure gradient is zero. In [33], the current author observed that this assumption extends from a linear potential flow assumption that can be extended into other physical phenomena. In heat transfer contexts, for example, we can assume a zero heat flux when there is no temperature gradient. In solid deformation contexts, this assumption can be interpreted as a zero strain inducing a zero stress. Hence, we make the fundamental assumption that

$$\hat{\Phi}(x, \Psi, \nabla\Psi) = 0 \text{ when } \nabla\Psi = 0.$$

To establish the coupling between scales, we apply the mean value theorem to the first order Taylor expansion of $\Phi(x, \Psi, \nabla\Psi)$ in terms of the third argument $\nabla\Psi$ and use our fundamental assumption. Here we assume the one dimensional case where $\nabla\Psi$ is a scalar

quantity. Consequently, there exists $\xi \in (0, \nabla\Psi)$ such that

$$\hat{\Phi}(x, \Psi, \nabla\Psi) = \hat{\Phi}(x, \Psi, 0) + \frac{d\hat{\Phi}(x, \Psi, \xi)}{d\nabla\Psi} (\nabla\Psi - 0). \quad (3.36)$$

Applying our fundamental assumption, the first term on the right hand side is eliminated, yielding

$$\hat{\Phi}(x, \Psi, \nabla\Psi) = \frac{d\hat{\Phi}(x, \Psi, \xi)}{d\nabla\Psi} \nabla\Psi. \quad (3.37)$$

Since the quantity $\frac{d\hat{\Phi}(x, \Psi, \xi)}{d\nabla\Psi}$ must be evaluated at the boundary of the control volume, it is approximated as

$$\begin{aligned} \frac{d\hat{\Phi}(x, \Psi, \xi)}{d\nabla\Psi} &\approx \frac{\hat{\Phi}_{i+\frac{1}{2}}(x, \Psi, \nabla\Psi) - \hat{\Phi}_{i+\frac{1}{2}}(x, \Psi, 0)}{\nabla\Psi - 0} \\ &= \frac{\hat{\Phi}_{i+\frac{1}{2}}(x, \Psi, \nabla\Psi)}{\nabla\Psi} \\ &\equiv -K_{i+\frac{1}{2}}(\Psi_i, \Psi_{i+1}). \end{aligned} \quad (3.38)$$

Substituting 3.38 into equation 3.37 and approximating $\nabla\Psi$ by the forward finite difference $D^+[\Psi_i] \approx \frac{\Psi_{i+1} - \Psi_i}{\Delta x}$, we obtain the expression

$$\hat{\Phi}_{i+\frac{1}{2}}(x, \Psi_i, \Psi_{i+1}) = -K_{i+\frac{1}{2}}(\Psi_i, \Psi_{i+1}) D^+[\Psi_i] \quad (3.39)$$

Deriving an analogous expression for $\Phi_{i-\frac{1}{2}}$ and substituting it and equation 3.39 into equation 3.35, we obtain

$$- \left[K_{i+\frac{1}{2}}(\Psi_i, \Psi_{i+1}) D^+[\Psi_i] - K_{i-\frac{1}{2}}(\Psi_{i-1}, \Psi_i) D^+[\Psi_{i-1}] \right] + h(\Psi_i) \Delta x = \hat{F}_i \Delta x \quad (3.40)$$

Regardless of whether $K_{i\pm\frac{1}{2}}$ is a constant function, equation 3.40 can be resolved by successive approximations Ψ_i^{n+1} (i.e. fixed point iteration) for all i as

$$- \left[K_{i+\frac{1}{2}}(\Psi_i^n, \Psi_{i+1}^n) D^+[\Psi_i^{n+1}] - K_{i-\frac{1}{2}}(\Psi_{i-1}^n, \Psi_i^n) D^+[\Psi_{i-1}^{n+1}] \right] + h(\Psi_i^{n+1}) \Delta x = \hat{F}_i \Delta x \quad (3.41)$$

So far, equation 3.41 still remains incomplete because no method has yet been specified to estimate $\hat{\Phi}_{i\pm\frac{1}{2}}$. The missing quantities are evaluated by a model which requires

limited information at the microscopic scale. In the following section, we outline two separate methods to estimate the missing information based on direct stiffness methods as a microscopic model.

3.3.2 Microscopic Deformation Model

In the deformation case, the reaction term $h \equiv 0$ while the missing quantities $\hat{\Phi}_{i \pm \frac{1}{2}}$ in 3.35 describes the total forces acting at the boundaries of a control volume. We estimate this total force by simulation of a microscopic model defined on a small region $B_\delta(x_{i+\frac{1}{2}})$ centered at $x_{i+\frac{1}{2}}$ with total length δ . For a one dimensional medium, we can neglect shearing forces and assume only axial deformations.

At sufficiently small deformations, we can describe a one dimensional medium as an assemblage of springs of varying stiffnesses connected at discrete nodes. For a particular node i , the sum of all forces from the connected springs F_{ij} is balanced by the total internal forces s_i acting directly on the node itself. Mathematically, this relation is written as

$$\sum_{j \in C_l} F_{lj} = s_l \quad (3.42)$$

where C_l denotes the set of nodes which connected to node l .

For simplicity, we assume that internodal forces are linearly proportional to the displacement by the linear relation

$$F_{lj} = K_{lj} (u_l - u_j)$$

where u_i and u_j are respectively the displacements at nodes l and j , and

$$K_{lj} = \frac{E_{lj} A_{lj}}{L_{lj}}$$

where E_{lj} is the young's modulus, A_{lj} is the cross-sectional area, and L_{lj} is the length of the spring.

Given fixed displacement conditions or a mix of fixed traction and fixed displacement at the boundaries produces a unique solution. In the context of the heterogeneous multiscale framework, we require a restriction operator which produces suitable boundary conditions onto the locally defined microscopic models. For the deformation model, microscale boundary conditions are linearly interpolated from the macroscopic displacements U_i and U_{i+1} to the boundaries of each $B_\delta(x_{i+\frac{1}{2}})$. For purely dirichlet boundary conditions, we can denote the left and right boundaries of the microscopic model $B_\delta(x_{i+\frac{1}{2}})$ as $u_{i+\frac{1}{2}}^L$ and $u_{i+\frac{1}{2}}^R$. By linear interpolation, these two boundary values are given as

$$u_{i+\frac{1}{2}}^L = U_{i+\frac{1}{2}} - \frac{U_{i+1} - U_i}{\Delta x} \left(\frac{\delta}{2} \right) \quad (3.43)$$

$$u_{i+\frac{1}{2}}^R = U_{i+\frac{1}{2}} + \frac{U_{i+1} - U_i}{\Delta x} \left(\frac{\delta}{2} \right) \quad (3.44)$$

where $U_{i+\frac{1}{2}} = \frac{U_i + U_{i+1}}{2}$ is the average macroscopic displacement value.

The poroelasticity problem addressed in this thesis is of the form 3.8- 3.9, which include mixed dirichlet-neumann boundary conditions in both displacement and pressure. After operator splitting, the multiscale solid equation 3.31– 3.32 also retain mixed boundary conditions. The use of mixed boundary conditions was not addressed by Chu et al. (2012)[26, 25]. For a one dimensional medium, we still use purely dirichlet boundary conditions on the microscopic model. The current thesis hypothesizes that the neumann boundary condition need only be applied at the macroscopic level. Thus, the initial guess of macroscopic displacements generates purely dirichlet boundary conditions at the microscopic level.

To complete our heterogeneous multiscale solid deformation model in 1D, we prescribe a data estimator which approximates the missing values $\hat{\Phi}_{i+\frac{1}{2}}$ in each $B_\delta(x_{i+\frac{1}{2}})$. Here, $\hat{\Phi}_{i+\frac{1}{2}}$ denotes the total force acting on the boundary of control volume i . Given the 1D nature of the microscopic model, this total force can be approximated by the force through any spring element in micro model i . For the current model, we choose

$$\hat{\Phi}_{i+\frac{1}{2}} \approx [K_{lj}(u_l - u_j)]_{i+\frac{1}{2}}$$

where the spring connecting nodes l and j lies on the left boundary of the local micro model defined in the region $B_\delta(x_{i+\frac{1}{2}})$.

3.3.3 Microscopic Flow Model

The pore network model described in 2.17 is a suitable surrogate for the elliptic diffusion equation 2.21 because it is a localized discrete analogy of the volumetric, macroscopic scale conservation law . In the context of the flow equation derived from operator splitting 3.32, an additional term must be added to the microscale pore network model to account for the non-zero reaction term $h(\Psi) \equiv c^* P_i \Delta x$ appearing in the macroscopic equation. Hence, we propose a modified network model

$$\sum_{j \in K_l} q_{lj} + c^* p_l \Delta x = s_l \quad (3.45)$$

$$q_{lj} = g_{lj}(\Delta P_{lj}) \quad (3.46)$$

$$g_{lj}(\nabla P_{lj}) = \frac{\pi r_{lj}^4}{8\mu L_{lj}} \quad (3.47)$$

We shall refer to this model as the ***Reaction-Diffusion Network Model (RDNM)***. Clearly, equation 3.45 is a discrete analogy of the macroscopic equation 3.32 and retains the essence of the macroscopic model. The flux term 3.46 and micro constitutive relation 3.47 are analogous to the pore network model using the Hagen-Poiseuille law.

As with Chu et al.'s original algorithm dirichlet boundary conditions are imposed onto opposite boundaries of the network model. Our proposed multiscale method uses the same restriction operator and data estimators as in Chu et al. (2012)[26, 25]. That is, we use linear interpolation formula analogous to 3.43 to obtain fixed pressure boundary conditions on opposite sides of the RDNM in the axial direction and impose periodic boundary conditions on the transverse boundaries. Given initial guess of macroscopic pressures P_i and P_{i+1} , linear interpolation produces left and right dirichlet boundary conditions $P_{i+\frac{1}{2}}^L$ and

$P_{i+\frac{1}{2}}^R$ given as

$$u_{i+\frac{1}{2}}^L = U_{i+\frac{1}{2}} - \frac{U_{i+1} - U_i}{\Delta x} \left(\frac{\delta}{2} \right) \quad (3.48)$$

$$u_{i+\frac{1}{2}}^R = U_{i+\frac{1}{2}} + \frac{U_{i+1} - U_i}{\Delta x} \left(\frac{\delta}{2} \right) \quad (3.49)$$

We also approximate the flux through the RDNM by taking the sum of the fluxes along a cross-section perpendicular to the axis of flow. The presence of a reaction term in the micromodel suggests that flux is non-constant throughout the micromodel. The primary flux of interest is through the boundary of the macroscopic control volumes, which correspond to the center of the micromodels. Hence, instead of using the flux through throats connected at the boundary, we use the sum of fluxes through throats connected to the center of $B_\delta(x_{i+\frac{1}{2}})$. In the case of a micromodel with an even number of throats, we use the average of the two cross-sectional fluxes through connected to the nodes corresponding to $x_{i+\frac{1}{2}}$. Denote $I_{i+\frac{1}{2}}^L$ and $I_{i+\frac{1}{2}}^R$ as the sets of all horizontal throats connected to a pore at $x_{i+\frac{1}{2}}$ from the left and right, respectively. Then, each $\hat{\Phi}_{i+\frac{1}{2}}$ is estimated as

$$\hat{\Phi}_{i+\frac{1}{2}} \approx \frac{f_1 + f_2}{2}$$

where $f_1 = \sum_{lj \in I_{i+\frac{1}{2}}^L} q_{lj}$ and $f_2 = \sum_{lj \in I_{i+\frac{1}{2}}^R} q_{lj}$ are the fluxes through the center-left and center-right cross-sections, respectively. The case with an odd number of horizontal throats only requires a single flux evaluation at the center throat.

3.4 Research Questions

The primary hypothesis of the current thesis is that the operator splitting method proposed above is sufficiently general that any suitable elliptic diffusion and elliptic reaction-diffusion PDE may be utilized. In particular, this approach enables the use of iterative multiscale methods such as those of the divide & conquer strategy. Banach Fixed Point Theorem suggests that the proposed operator splitting method is convergent at each time step un-

der sufficient conditions which depend on not only on the choice of temporal and spatial stepsizes, but also the material parameters.

Hence, this thesis focuses on the convergence of both the operator splitting scheme and the multiscale approximations. The objectives of this thesis are to:

- Characterize of the material parameter constraints which enable convergence of the operator splitting method.
- Investigate the convergence of the proposed multiscale algorithms to resolve the two elliptic problems obtained from the operator splitting

In Chapter 4, we characterize the parameter space for which the operator splitting method converges and diverges by obtaining the threshold surface separating the two spaces by numerical methods and observing the effects of parameter perturbations. We obtain results for two particular cases:

- **The constant case** - All material parameters are constant
- **The linearly variant case** - Mobility $K(x)$ and Elastic Modulus $\nu(x)$ are linear functions, while all other material parameters are constant.

In chapter 5, we verify the convergence of the proposed multiscale methods for the solid and fluid equations derived from operator splitting. We begin by verifying the implementation of Chu et al.'s algorithm for steady state fluid flow in porous media. We then proceed to verify our multiscale algorithms for the decoupled fluid and solid equations obtained from our operator splitting method. In particular, we seek to confirm their convergence in the case with constant, linearly variant, and heterogeneous (random) material parameters.

In chapter 6, we discuss the results of our operator splitting and multiscale tests and interpret their implications. We also discuss the limitations of our study and propose suggestions for further studies and improvements in chapter 7.

Chapter 4

Operator Splitting Experiments

The stability of our proposed operator splitting method in chapter 3 depends on the spectral radius ρ of the product of $M^{-1}N$, where M & N are block operators. The eigenvalues of $M^{-1}N$ depend on the chosen spatiotemporal discretization and the material properties $\nu(x)$, $K(x)$, α and c_0 . The exact nature of this relation is unknown and this thesis seeks to estimate this relation numerically. We restrict our attention to two particular cases of poroelasticity problems distinguished by the degree of heterogeneity.

4.1 Case I

In Case I, we assume homogeneous material properties in equations 3.8- 3.9. That is, the parameters K , ν , α , and c_0 are all constant in space and time. To simplify our analysis, we nondimensionalize equations 3.8- 3.9 by introducing new spatial, temporal, and state variables. Here, we follow an analogous approach to [41]; nondimensionalizing with respect to the domain length L and traction boundary condition T_L . We select

$$\hat{x} \equiv \frac{x}{L} \text{ (dimensionless space),} \quad (4.1)$$

$$\hat{t} \equiv \frac{\nu k t}{L^2} \text{ (dimensionless time),} \quad (4.2)$$

$$\hat{p} \equiv \frac{p}{T_L} \text{ (dimensionless pressure),} \quad (4.3)$$

$$\hat{u} \equiv \frac{\nu u}{T_L L} \text{ (dimensionless displacement).} \quad (4.4)$$

Substituting the new variables into equations 3.8- 3.9, we obtain

$$-\frac{d^2\hat{u}}{d\hat{x}^2} + \alpha \frac{d\hat{p}}{d\hat{x}} = 0, \quad (4.5)$$

$$\frac{d}{d\hat{t}} \left(\beta \hat{p} + \alpha \frac{d\hat{u}}{d\hat{x}} \right) - \frac{d^2\hat{p}}{d\hat{x}^2} = 0, \quad (4.6)$$

where $\beta \equiv c_0\nu$. By these choices, the nondimensional domain becomes $\Omega_{nondimensional} \equiv [0, 1]$. The initial condition also becomes non-dimensionalized as

$$\beta p + \alpha \frac{d\hat{u}}{d\hat{x}} = 0.$$

By definition, $\alpha \in [0, 1]$ is a dimensionless parameter which characterizes the strength of the coupling between the flow and deformation equations. In the simplest case with $\alpha = 0$, the two equations are completely decoupled from each other. In contrast, the case with $\alpha = 1$ characterizes the strongest possible coupling between the two processes. We predict that as $\alpha \rightarrow 0$, a wider range of β values will converge for a given spatiotemporal stepsize Δx & Δt . We also predict that as $\alpha \rightarrow 1$, the range of β values result in a convergent operator splitting becomes narrower for a given Δt and Δx . Thus, for a given Δt and Δx there exists some threshold value β^* which separates the range of problems which can and cannot be solved by the proposed operator splitting methods for a specific Δt and Δx . This threshold value is attained precisely at the value of β^* such that the corresponding spectral radius of $M^{-1}N = 1$.

In the absence of analytical methods to determine a closed form of the spectral radius of $M^{-1}N$ in terms of α , β , Δt and Δx , we determine its relation numerically by finding the optimal threshold β^* value for various choices of δt and δx . For each choice of α , δt and δx , we apply a bisection search algorithm of the parameter space $\beta \in [0, \infty)$ to find β^* such that $\rho(M^{-1}N) = 1$.

Given parameter α and stepsizes Δt and Δx . Let the operator splitting method (block jacobi or block gauss-seidel) also be given. Let the matrix pairs (M_1, N_1) and (M_2, N_2) be the discretized split operator pairs generated from applying our chosen operator splitting method to equations 4.5- 4.6. That is, M_1 and N_1 are constructed using α , Δt , and β_1

and discretizing the split operators by some numerical scheme with spatial stepsize Δx . The matrix pair (M_2, N_2) are constructed analogously using β_2 in place of β_1 . Let ρ_1 and ρ_2 denote the two spectral radii of (M_1, N_1) and (M_2, N_2) . Assume that ρ_1 and ρ_2 lie on opposite sides of the desired value $\rho^* \equiv 1$; that is,

$$(\rho_1 - \rho^*)(\rho_2 - \rho^*) < 0.$$

The bisection search algorithm works moving the bounds β_1 and β_2 containing the root of the equation $\beta^* - 1 = 0$ closer to the true value of β^* . This is accomplished selecting the midpoint value $\beta_{mid} = \frac{\beta_1 + \beta_2}{2}$ and determining the spectral radius ρ_{mid} corresponding to the discrete matrices M_{mid}, N_{mid} constructed from β_{mid} . If the value $(\rho_{mid} - \rho^*)(\rho_1 - \rho^*) < 1$ then the interval between β_{mid} and β_1 contains the desired value ρ^* and the bound β_2 is reassigned to β_{mid} . Otherwise, the interval between ρ_{mid} and ρ_2 contains the desired value ρ^* and the bound β_1 is reassigned to β_{mid} . This process repeats itself until the residual $|\rho_{mid} - \rho^*|$ is less than some given tolerance ϵ .

Due to memory limitations and time constraints, we limit our experiments to spatiotemporal steps in terms of powers of two. That is, we choose $\Delta x = 2^{-i}$ for $i = 2, 3, \dots, 8$ and $\Delta t = 2^{-j}$ for $j = 2, 3, \dots, 18$. The spectral radius is obtained by using MATLAB's *EIG()* function and selecting the maximum eigenvalue in absolute value. We formulate the matrix $M^{-1}N$ by explicit calculation of M^{-1} and its multiplication to N . The resulting matrix is dense and requires a computationally expensive process to determine the eigenvalues. Due to time and memory limitations, we are unable to select $\Delta x > 2^8$.

We repeat our analysis for successively decreasing values of α as $\alpha \rightarrow 0$. We predict that as $\alpha \rightarrow 0$, the convergence constraint diminishes for all spatiotemporal discretization choices.

The matrices M and N are obtained by discretizing the split operators derived from equations 4.5- 4.6 by finite difference method. We use a backward difference in time and centered differences in space for both first and second derivative approximations using a staggered grid as illustrated in figure 4.1. As noted in [53, 39], application of the finite



Figure 4.1: Staggered grid for finite difference discretization. Open and closed circles represent displacement and pressure points, respectively.

difference method to the poroelasticity equations on standard collocated grids leads to large, non-physical oscillations which hinder the accuracy of the solution. Staggered grids consisting of alternating pressure and displacement points reduce this effect[42] and lead to greater overall accuracy¹. In this case, the quantity Δx represents the distance between two consecutive pressure points and two consecutive displacement points. The number of intervals for each state variable is defined by $N = \frac{1}{\Delta x}$, which is always guaranteed to be a positive integer by our aforementioned choices of Δx . This choice induces $N + 1$ pressure points and $N + 1$ displacement points (including boundary points), which produces staggered grid containing a total of $2N + 2$ points.

4.1.1 Results

Figures 4.2- 4.13 display the threshold β^* values at various choices of Δt and Δx . Figures 4.2- 4.5, 4.6- 4.9, and 4.10- 4.13 show the thresholds for the Block Jacobi, Block Upper Gauss-Seidel, and Block Lower Gauss-Seidel splitting methods, respectively. Each individual graph represents a different value of α .

The results indicate that there is no qualitative difference between the convergence behavior of the Block Jacobi and Gauss-Seidel splittings. They are all, at best, *conditionally convergent*. The existence of a surface separating convergent and divergent indicates that for any given Δt and Δx , there exists some range of parameter values such that the splitting will not converge. Non-dimensionalization of the homogeneous constant coefficient case in-

¹It is also stated in[39] that a backward time difference is unconditionally stable for all values of β . Note that stability and consistency of the finite difference method are insufficient conditions to guarantee convergence of the proposed operator splitting methods.

indicates that for a given $\alpha \in [0, 1]$, the product $\beta \equiv c_0\nu$ is the primary quantity which characterizes the convergence or divergence of the operator splitting. The space of convergent and divergent coupled problems separated by the surface $\beta^*(\Delta t, \Delta x)$, corresponding to the values of β such that the spectral radius of the discrete operator $M^{-1}N$ is less than unity for each tested value α . It was determined that the half space $\beta \geq \beta^*(\Delta t, \Delta x)$ always corresponds to the set of parameters such that the operator splitting converges.

In all operator splitting methods and for a given α and constant Δx , the surface $\beta^*(\Delta t, \Delta x)$ decreases as Δt increases. A similar trend is observed for all other values of α . Due to the unconditionally stable implicit timestepping scheme, this indicates that the recommended strategy to ensure convergence for a given β is to *increase* the time stepsize, rather than decreasing it. While this strategy ensures convergence, it sacrifices accuracy in the process as larger Δt decreases the order of accuracy in the obtained solution.

In the case of strong fluid-solid coupling ($\alpha = 1$), it was also observed that for all proposed operator splitting methods with constant α and $(\Delta t, \Delta x \rightarrow (0, 0))$, the threshold surface $\beta^*(\Delta x, \Delta t)$ increases asymptotically to unity. We conjecture that the range of parameters values β which enable convergence of all proposed operator splitting methods can be conservatively estimated by the half-space above the threshold plane $\beta = 1$.

In the limit as $\alpha \rightarrow 0$, we observe that the threshold surface $\beta^*(\Delta t, \Delta x)$ decreases uniformly in value as does the threshold plane. This indicates that a greater range of parameter values converge as the coupling strength decreases. For a fixed Δt , Δx , and β , the spectral radius of $M^{-1}N$ also decreases as $\alpha \rightarrow 0$. This implies that if convergent, the operator splitting methods converge faster as the strength of the coupling decreases. Indeed, this is consistent with our previous assumptions.

Although any value of β above the threshold surface ensures convergence, the number of iterations required to converge within a given error tolerance ϵ varies for different β . The rate of convergence of fixed point iterations is known to be inversely proportional to the spectral radius of the discrete operator $M^{-1}N$. Thus, the expected number of iterations required to converge as increases as $\beta \rightarrow \beta^*(\Delta x, \Delta t)$ and decreases as $\beta \rightarrow \infty$. Due

Table 4.1: Convergence Table for $\alpha = 1$, $\Delta t = 0.001$, and $\Delta x = 0.002$

β	$\rho(M^{-1}N)$	iterations
0.9	1.0528	Does not converge
1	0.99877	2510
2	0.70624	16
5	0.4466	8
10	0.31584	6
100	0.099877	2

to the diffusive nature of the solutions to the poroelasticity equations for fixed boundary conditions², the maximum number of iterations required to converge at any timestep is bounded by the first timestep. We also test the convergence behavior for a constant Δt , Δx , and α . In these tests, the fixed point iteration uses the residual convergence criterion

$$\|v_{coupled}^t - v_{split}^{t,k}\| \leq \epsilon$$

where $v_{coupled}^t = (u^t, p^t)^T$ and $v_{split}^{t,k} = (u^{t,k}, p^{t,k})^T$ are the numerical solutions from solving the fully coupled and the jacobi operator splitting methods, respectively. For experimentation, we chose $\epsilon = 10^{-5}$ in all tests. The data displayed in Table 4.1 is consistent with theoretical predictions.

4.2 Case II

In Case II, we assume the elastic moduli $\nu(x)$ and mobility $K(x)$ are linear functions of space and all other material parameters are constant. Characterization of all the infinite variations in possible choices $\nu(x)$ and $K(x)$ is beyond the scope of this thesis. We limit our current analysis to linear functions

$$\nu(x) = K(x) = mx + b > 0$$

²Boundary conditions that do not vary in time.

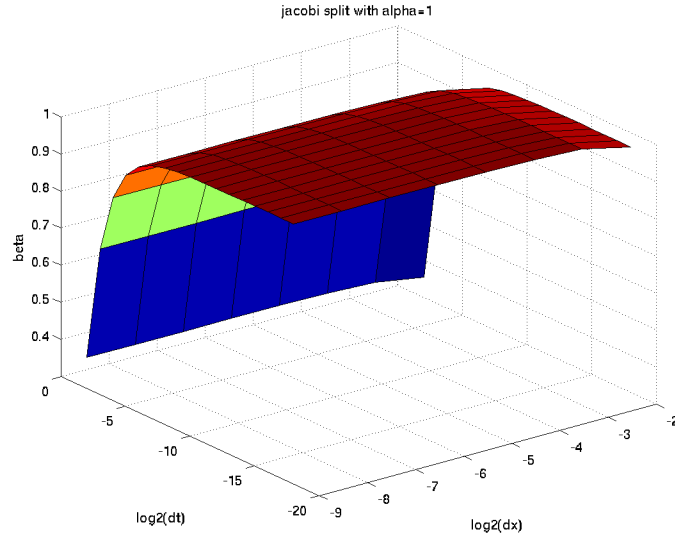


Figure 4.2: Threshold Surface β^* at various Δt and Δx values with $\alpha = 1$.

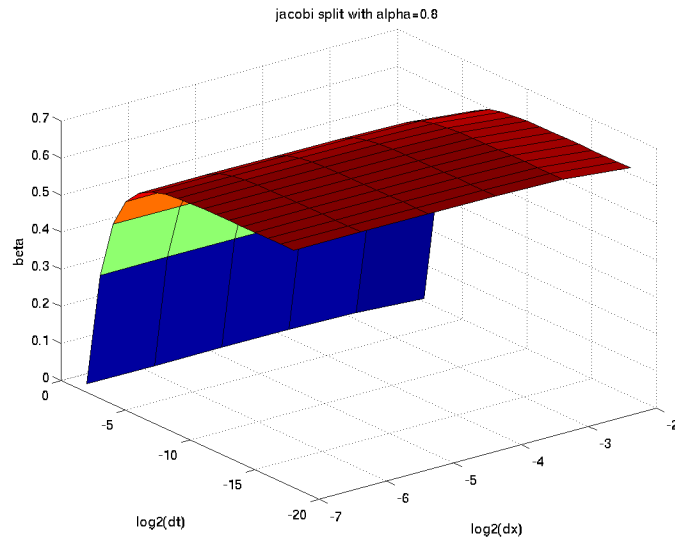


Figure 4.3: Threshold Surface β^* at various Δt and Δx values with $\alpha = 0.8$.

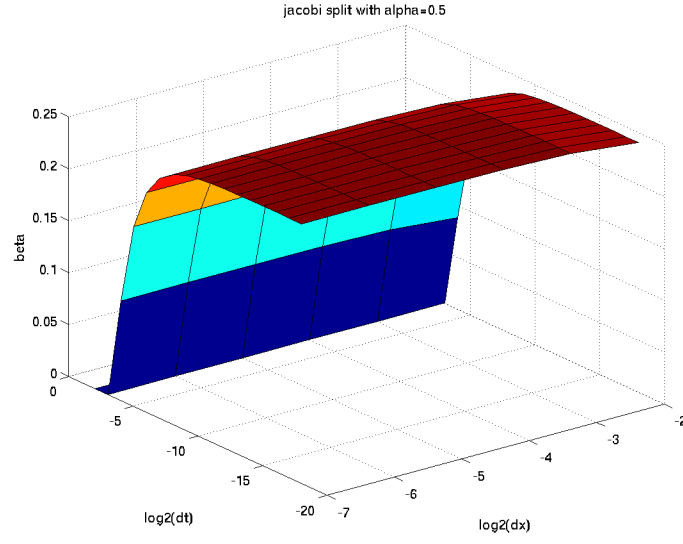


Figure 4.4: Threshold Surface β^* at various Δt and Δx values with $\alpha = 0.5$.

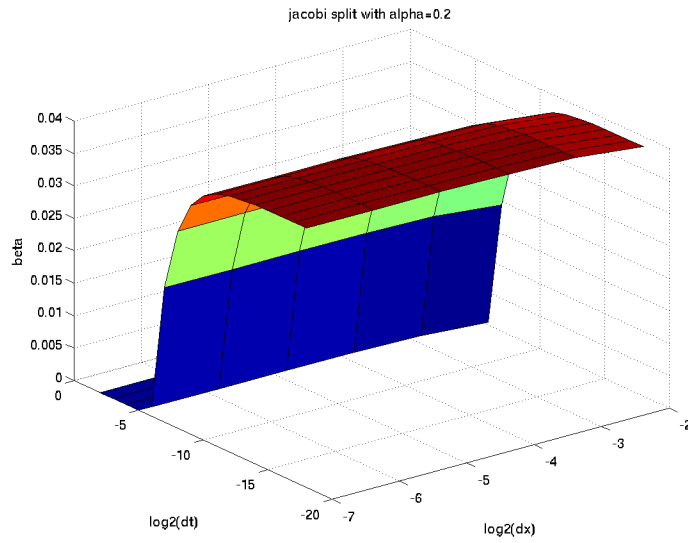


Figure 4.5: Threshold Surface β^* at various Δt and Δx values with $\alpha = 0.2$.

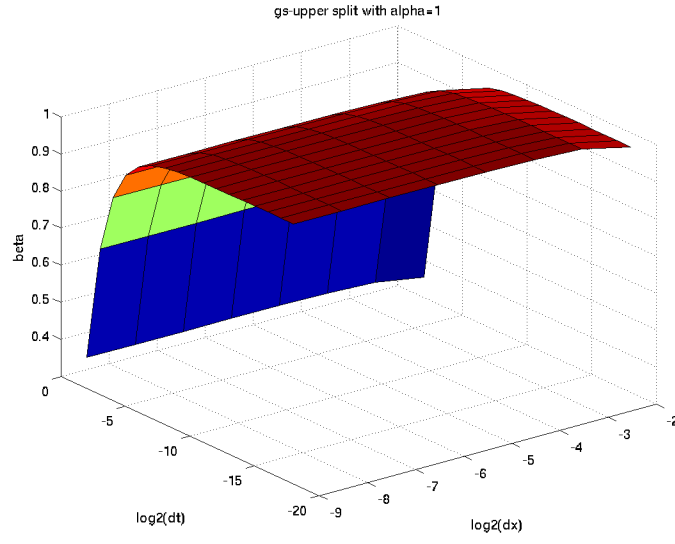


Figure 4.6: Threshold Surface β^* at various Δt and Δx values with $\alpha = 1$.

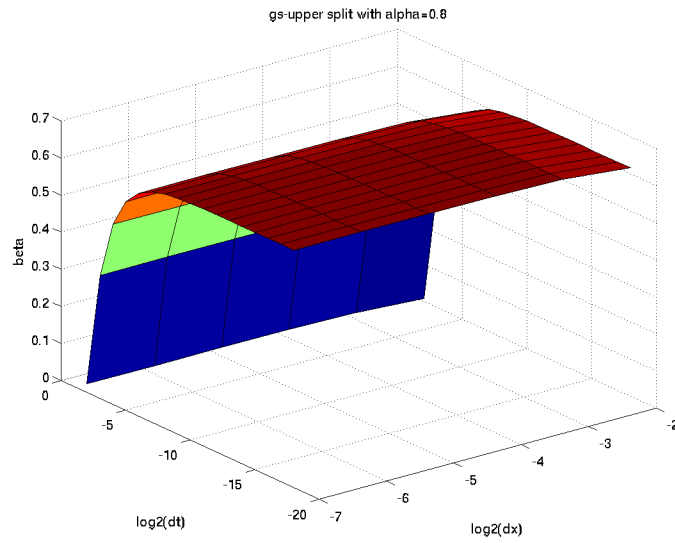


Figure 4.7: Threshold Surface β^* at various Δt and Δx values with $\alpha = 0.8$.

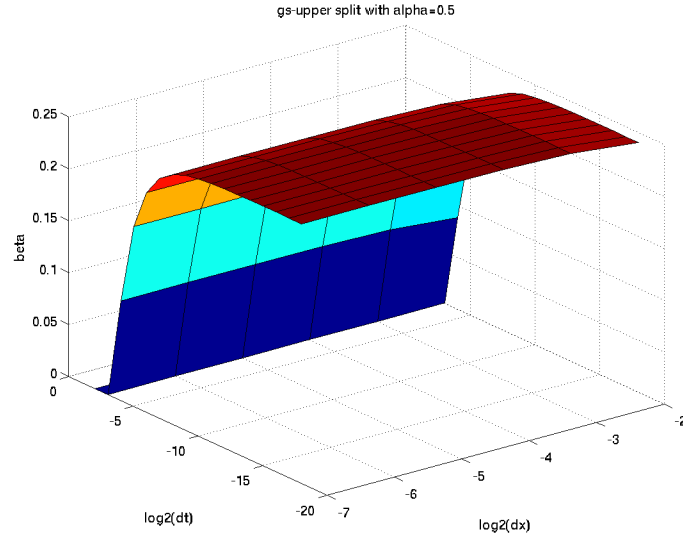


Figure 4.8: Threshold Surface β^* at various Δt and Δx values with $\alpha = 0.5$.

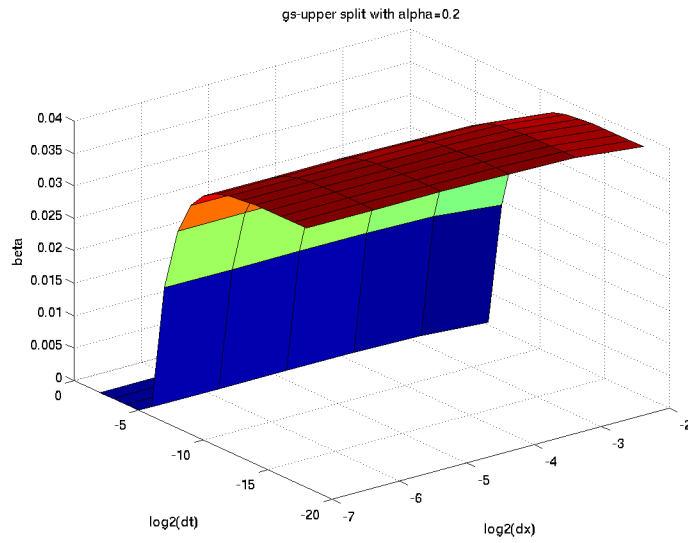


Figure 4.9: Threshold Surface β^* at various Δt and Δx values with $\alpha = 0.2$.

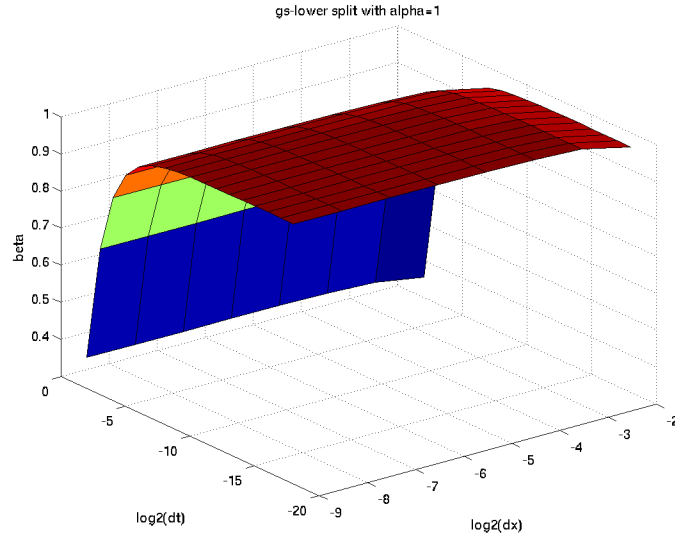


Figure 4.10: Threshold Surface β^* at various Δt and Δx values with $\alpha = 1$.

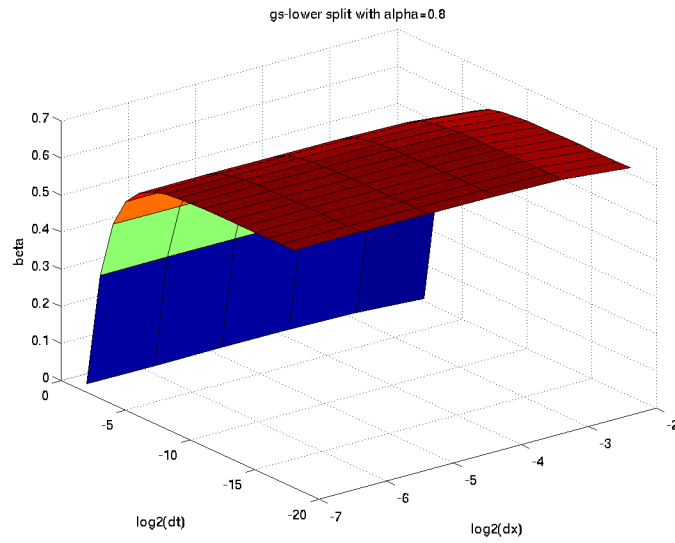


Figure 4.11: Threshold Surface β^* at various Δt and Δx values with $\alpha = 0.8$.

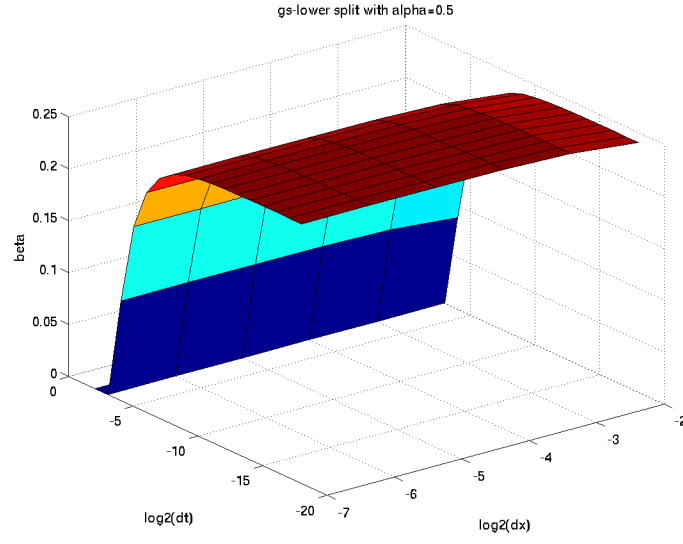


Figure 4.12: Threshold Surface β^* at various Δt and Δx values with $\alpha = 0.5$.

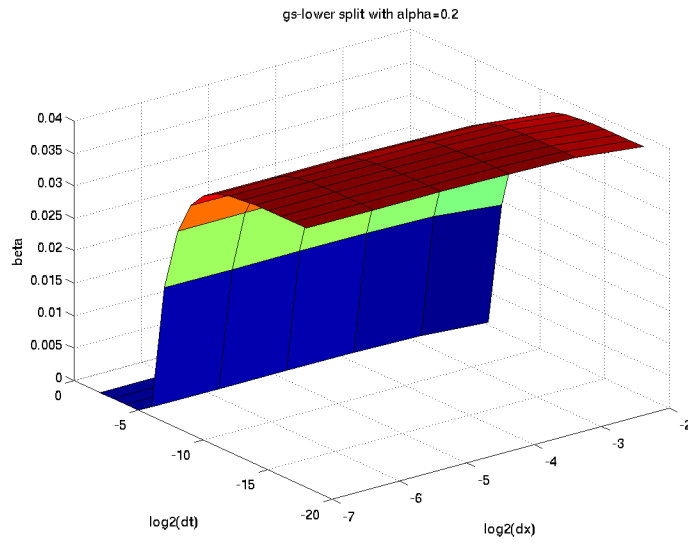


Figure 4.13: Threshold Surface β^* at various Δt and Δx values with $\alpha = 0.2$.

with positive slope m . We also restrict our domain to the interval $[0, 1]$.

Motivated by the results of the non-dimensional constant coefficient case, we hypothesize that the values of $c_0\nu(x)$ play an essential role in the characterization of the convergence of the operator splitting methods. Without loss of generality, we restrict $c_0 = 1$ and $\alpha = 1$. In our tests, we also hold the slope m constant and determine the optimal threshold y-intercept b value which ensures convergence for each choice of Δt and Δx . Using the same framework as in Case I. We discretize the fully coupled and split equations by finite difference method on a staggered grid.

Based on the previous results, we predict that when $\nu(x) < 1$ for all $x \in [0, 1]$, the operator splitting diverges. Likewise, we expect the splitting method to converge when $\nu(x) \geq 1$ for all $x \in [0, 1]$. In this convergent case, we anticipate the rate of convergence to increase as the $\min_{x \in [0, 1]} \nu(x)$ increases. We also anticipate divergence if $\nu_{min} \leq \nu(x) \leq \nu_{max}$ for all $x \in [0, 1]$, with $0 < \nu_{min} < 1$ and $\nu_{max} > 1$.

4.2.1 Results

Figures 4.14- 4.19 display the threshold y-intercept b surfaces at various Δt and Δx for constant $c_0 = \alpha = 1$. Each graph corresponds to a different value of the slope $m = 10^i$ for $i = -2, -1, \dots, 3$ such that $\nu(x) = mx + b$. For the small positive slopes chosen in figures 4.14 and 4.15, the threshold surface b^* is bounded by the plane $b = 1$ over the range of Δt and Δx values tested. As before, the threshold surface is monotonically increasing as $\Delta t, \Delta x \rightarrow 0$ and $b^*(\Delta t, \Delta x) \rightarrow 0$ as Δt increases. This indicates that convergence can be ensured for fixed spatial discretization Δx by increasing the time step Δt . Further testing (not displayed) indicates that decreasing α also decreases in the asymptotic limiting plane which the threshold surface approaches, but never crosses.

As the slope m increases (figures 4.16- 4.19), the threshold surface b^* values decreases at all $(\Delta t, \Delta x)$. As shown in figure 4.16, the decrease in the threshold surface values does not correspond to a vertical shift in the surface, but rather a lateral shift towards the origin in the Δx - Δt plane. In the case where $m = 100$ and $m = 1000$ (figures 4.18-

Table 4.2: Convergence for $c_0 = 1$

m	b	c_0	$\rho(M^{-1}N)$	iterations
0.2	0.9	1	1.01	Does not converge
0.2	1.0	1	0.96	162
0.2	1.1	1	0.92	16
0.2	2	1	0.68	8
0.2	5	1	0.44	6
0.2	20	1	0.2175	2

Table 4.3: Convergence for $c_0 = 0.5$

m	b	c_0	$\rho(M^{-1}N)$	iterations
0.2	1.8	0.5	1.02	Does not converge
0.2	1.9	0.5	0.98	522
0.2	2.0	0.5	0.96	168
0.2	5	0.5	0.61	14
0.2	20	0.5	0.2175	6

4.19, respectively), the threshold surface reduces smaller than machine epsilon for double precision ($O(10^{-324})$). The plane $b = 1$ remains an asymptotic limit in these cases, despite not being visible in the range of $\Delta t, \Delta x$ displayed. This result indicates that the convergence of our operator splitting method is less restrictive for large Δx when material property gradient is large. In contrast, when the material property gradient is small, the threshold surface is nearly identical to the limit plane $b = 1$ over all Δt and Δx .

Tables 4.2-4.3 show the convergence behavior for various values of b and c_0 for $\alpha = 1$, $\Delta x = 0.002$ and $\Delta t = 0.001$. In the case with $c_0 = 0.5$, the optimal threshold y-intercept b^* value is roughly double that of the case with $c_0 = 1$. This shift corresponds to a shift in the threshold surface upwards. Also, the optimal threshold b^* value shifts to slightly less than double the value with $c_0 = 1$. This is a byproduct of the variation encompassed by

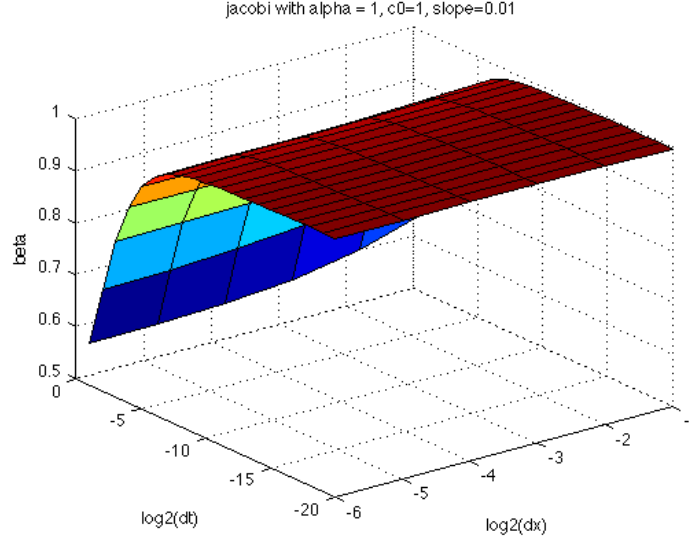


Figure 4.14: Threshold Surface of optimal y-intercept b^* values at various Δt and Δx values with $\alpha = c_0 = 1$ and $m = 0.01$.

the slope $m = 0.2$. In this context, the value of the slope m shifts the threshold surface horizontally toward the origin in the Δx - Δt plane.

These findings contradict our initial assumption that the operator splitting method diverges when $\nu(x)$ obtains values less than and greater than unity in the domain $x \in [0, 1]$. It implies that the material property gradients play a significant role in characterizing the convergent problems for our proposed operator splitting methods. In the case of linear heterogeneity, our operator splitting method converges for a wider range of discretization choices $\Delta t, \Delta x$ when a large gradient exists. However, the threshold surface increases as $\Delta t, \Delta x$ decrease, approaching a limiting surface. This indicates that conditional stability holds for material properties under a limiting plane. The value of this plane strongly depends on the value of α and c_0 .

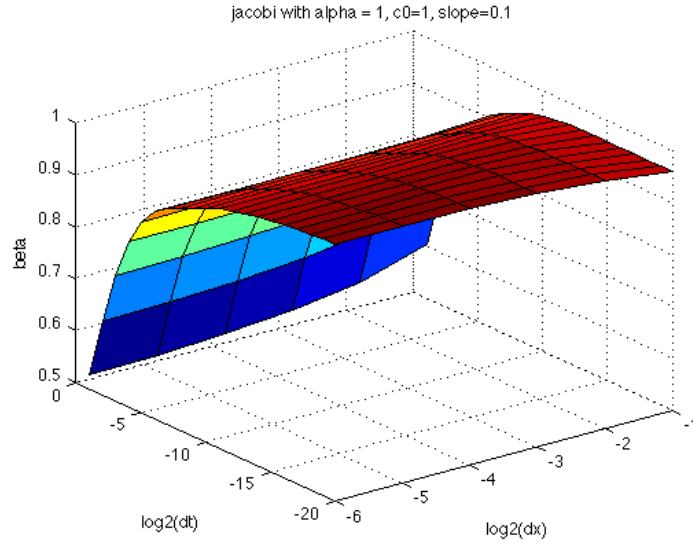


Figure 4.15: Threshold Surface of optimal y-intercept b^* values at various Δt and Δx values with $\alpha = c_0 = 1$ and $m = 0.1$.

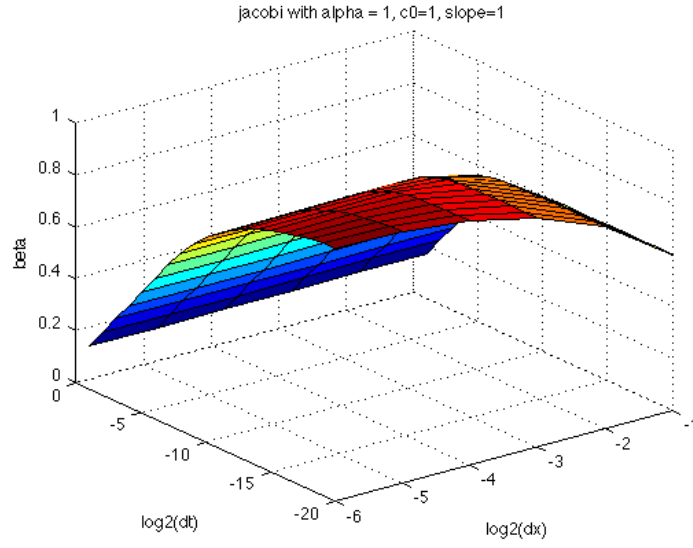


Figure 4.16: Threshold Surface of optimal y-intercept b^* values at various Δt and Δx values with $\alpha = c_0 = 1$ and $m = 1.0$.

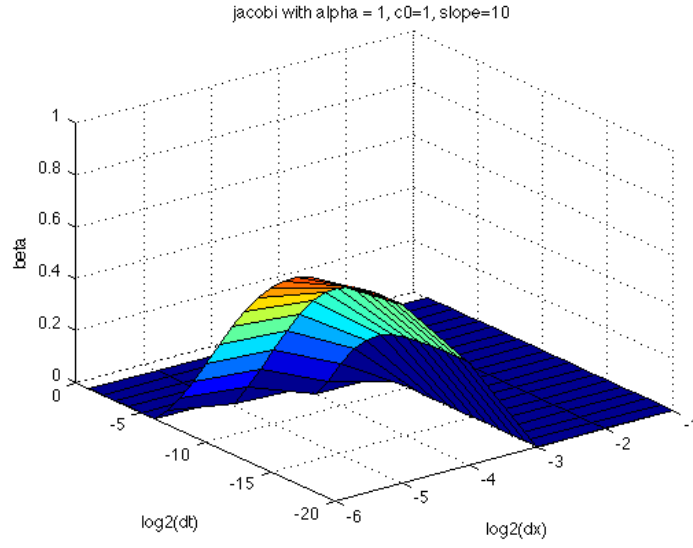


Figure 4.17: Threshold Surface of optimal y-intercept b^* values at various Δt and Δx values with $\alpha = c_0 = 1$ and $m = 10.0$.

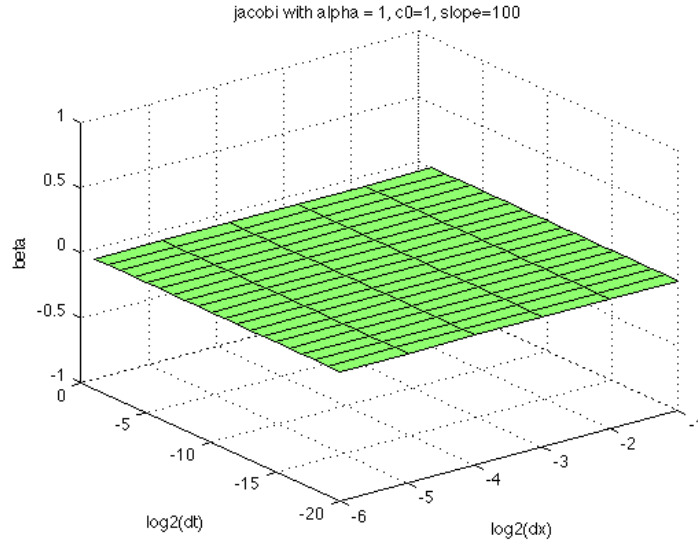


Figure 4.18: Threshold Surface of optimal y-intercept b^* values at various Δt and Δx values with $\alpha = c_0 = 1$ and $m = 100.0$.

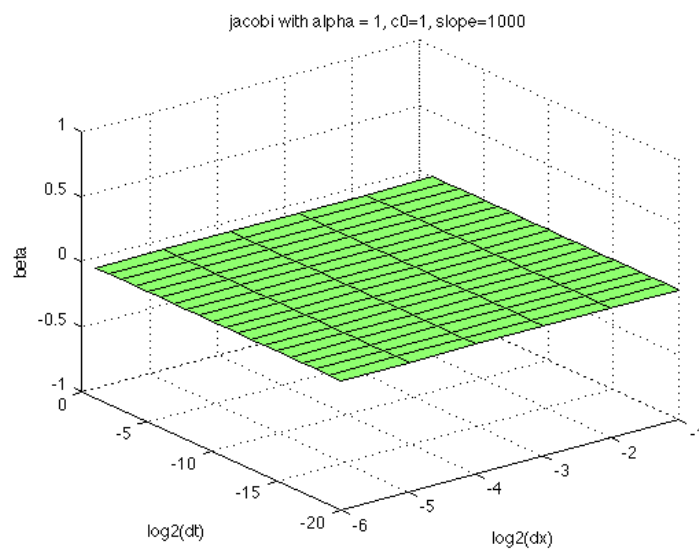


Figure 4.19: Threshold Surface of optimal y-intercept b^* values at various Δt and Δx values with $\alpha = c_0 = 1$ and $m = 1000.0$.

Chapter 5

Multiscale Experiments

In this chapter, we explore the convergence of the proposed multiscale method for fluid flow and solid deformation. We divide our analysis into three stages in which we verify the convergence of the following methods separately:

1. Chu et al.'s method for multiscale flow in porous media
2. Our multiscale solid deformation method
3. Our multiscale reaction-diffusion method

5.1 Verification of Chu et al.'s method

In our preliminary numerical verification experiments, we implemented Chu et al.'s method for fluid flow in porous media. We designed two dimensional medium consisting of a pore network of size 10×4096 throats of unit length L . Each interior pore is connected by four throats while boundary pores are connected by a single throat. The flux between flux is given as by the Hagen-Poiseuille Law. Additionally, a uniform pressure gradient was imposed with $p = 100$ on the left and $p = 0$ on the right axial boundaries (x-direction) and periodic conditions on the transverse boundaries (y-direction). For simplicity, a unit fluid viscosity was also used.

To confirm the convergence of the multiscale method, we vary the number of sampling subdomains μ and sample lengths δ to be positive integer powers of two such that $16 \leq \mu\delta \leq 4096 * L$. As illustrated in figure 5.1 samples of length δ are extracted from center of the subdomain $x_{l+\frac{1}{2}}$ of size Δx . Each sample pore network is of size $\delta \times 10$ throats.

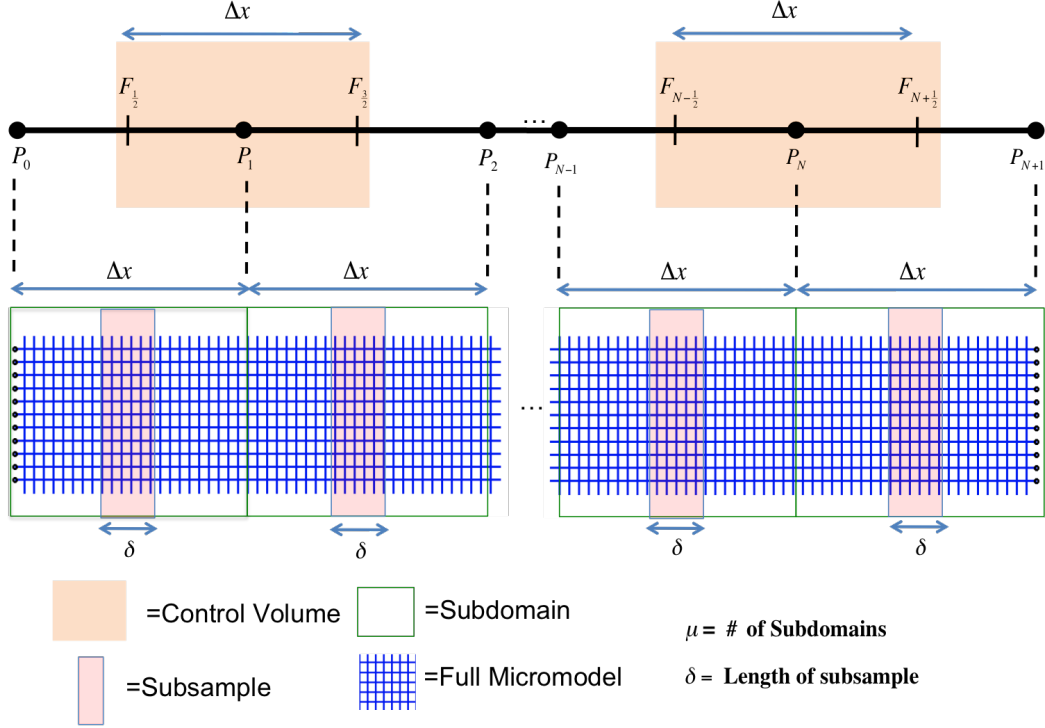


Figure 5.1: Illustration of a one dimensional multiscale flow model method sampling a two-dimensional pore network model

This ensures that the boundaries of all sampled pore networks correspond to nodes of the original network and no throats are artificially truncated.

To measure the error in the multiscale method, we compare the computed pressure and flux values to those of the fully microscopic pore network model consisting of 10×4096 throats. Note that the macroscopic pressure values computed in the multiscale method are in a one-dimensional domain, but the fully microscopic model is two dimensional. To compare, we average the pressure values along each vertical cross-section of the fully microscopic pore network model and compare only those pressure values at locations collocated in the macroscopic grid of the multiscale model. We define the relative ∞ -norm metric in pressure and flux respectively as $e_{\infty}^p \equiv \frac{\|P_m - P_d\|_{\infty}}{\|P_d\|_{\infty}}$ and $e_{\infty}^F \equiv \frac{\|F_m - F_d\|_{\infty}}{\|F_d\|_{\infty}}$, where P_m and F_m are the pressure and flux values obtained from the multiscale method while P_d and F_d are the average pressure and flux values obtained from the fully microscopic model. In this

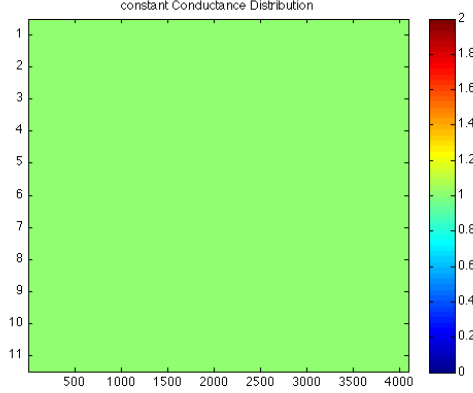


Figure 5.2: Conductance distribution for Fluid Flow Case I.

context, the infinity norm error produces the maximum error between the fully microscopic and multiscale models only at overlapping grid points. All other grid points of the fully microscopic model are ignored.

According to [26, 25], the multiscale method converges in a single iteration from any initial guess of the vector of macroscopic pressure values P satisfying the macroscopic boundary conditions assuming that the microscopic conductance is linear. In our experiments, we allow the multiscale method to iterate between micro and macroscale models until the maximum error in pressure between two consecutive iterations is less than $\epsilon \equiv 10^{-8}$. In all experiments, we chose the initial guess of macroscopic pressure to be linearly distributed between the (dirichlet) boundary conditions.

We conduct three classes of numerical experiments to verify the accuracy of the multiscale flow model. The three experiments correspond to different distributions of conductances within the fully microscopic model. Figures 5.3- 5.4 depict the conductances for the three cases tested.

In experiment I, we assume constant conductance values $g = 1$ at all locations in the fully microscopic grid. In this case, we hypothesize that all simulations, irrespective of sample size or number of sampling domains, converge to the same solution with the same accuracy.

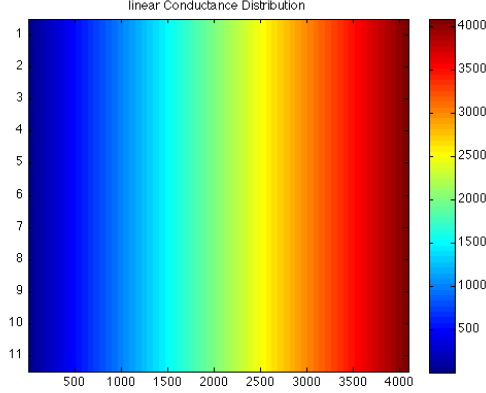


Figure 5.3: Conductance distribution for Fluid FLOW Case II.

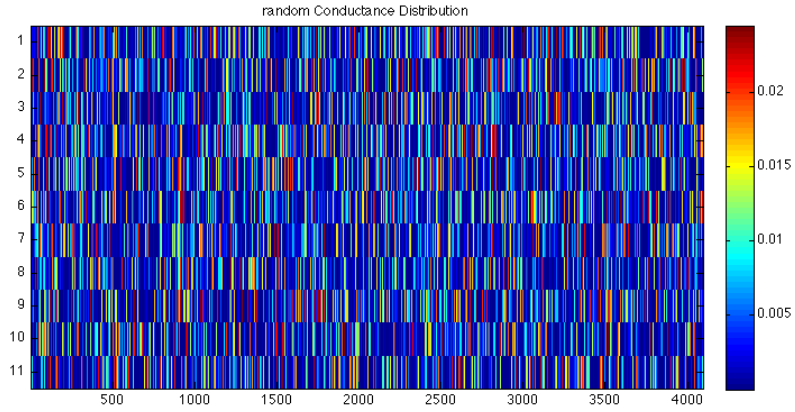


Figure 5.4: A random conductance distribution for Fluid Flow Case III.

In experiment II, we assume linearly increasing conductance values from the left to the right of the domain. $g(x) = x$ where x is the x-component of the coordinates center of the throat. As such, there is no variation in conductance values across any vertical cross-section in the fully microscopic model. All variations in conductances are in the horizontal direction. In this case, we hypothesize that the structured nature of the conductance values should lead to rapid convergence.

In experiment III, we assume the conductances are distributed randomly throughout the fully microscopic model. We generate the random conductances by randomly assigning

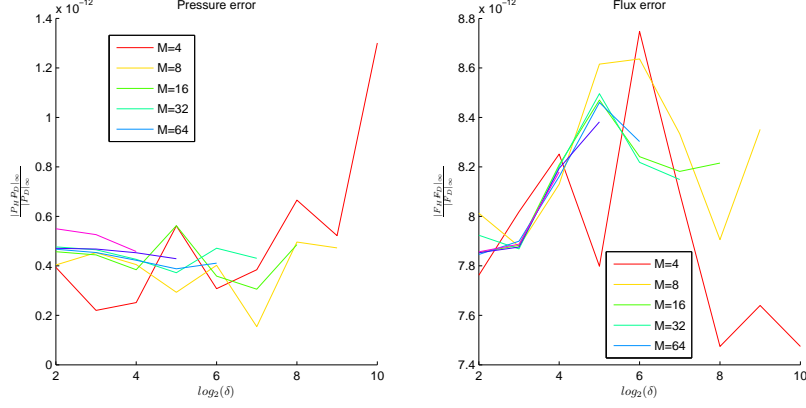


Figure 5.5: Experiment I Constant μ Analysis: Solid lines represent a constant number of sampling domains μ with relative errors displayed for pressure (left) and flux (right).

throat radii of the throats in the model. In our experiments, the throat radii are uniformly randomly assigned in a range $[r_{min}, r_{max}]$, with $r_{min} = 0.005$ to $r_{max} = 0.5$. Since the Hagen-Poiseuille Law assigns conductance in quartic proportion with the radius of the throat connecting two pores this corresponds to a conductance range $[2.25 \times 10^{-10}, 2.25 \times 10^{-2}]$. To remove any bias in error calculation due to the distribution, we conduct 100 separate tests, each with its own separate initial distribution. Within each individual test, all subsequent error analysis varying the number of sampling domains μ and sample size δ is conducted on the same initial conductance distribution. Finally, all relative pressure and flux errors for each combination of μ and δ are averaged.

5.1.1 Experiment I

Recall that in Experiment I, we assume a constant conductance value distributed throughout the fully microscopic model. In this case, we previously assumed that the relative errors would be nearly zero in all cases. Clearly, Figures 5.5 and 5.6 illustrates that non-zero errors exist between the multiscale solution and the fully microscopic solution. Figure 5.5 illustrates the convergence of the multiscale method holding the number of sampling

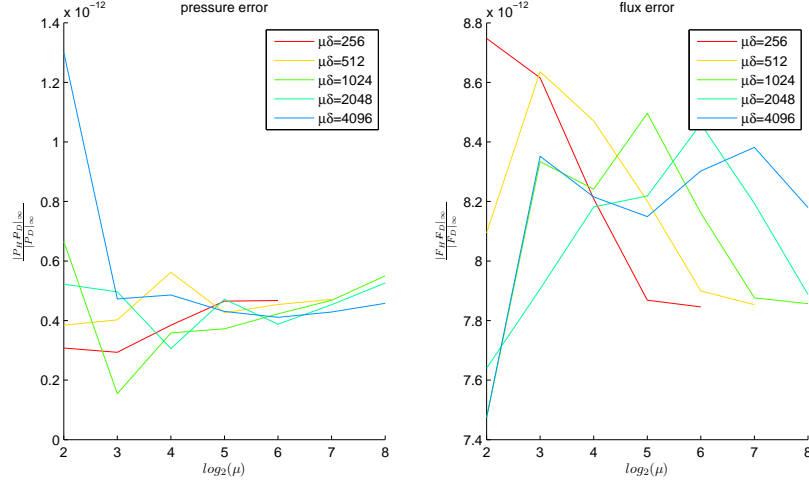


Figure 5.6: Experiment I Constant $\mu\delta$ Analysis: Solid lines represent a constant total sampling area $\mu\delta$ with relative errors displayed for pressure (left) and flux (right).

subdomains μ constant and varying the size of the sampling domain. Figure 5.8 illustrates the convergence behavior as the total sampling area $\mu\delta$ is held constant and the number of sampling domains increases. The relative error is less than 1.4×10^{-12} for pressure and 8.6×10^{-8} in flux. Though the flux errors remained slightly larger in magnitude the flux errors, both were extremely small and nearly equal to the convergence criterion parameter ϵ .

Note that in all cases of Experiment I, the multiscale method converged in only two multiscale iterations, which is the minimum number possible under our constraints. Further experimentation with consecutive iteration error $\epsilon = 10^{-11}$ revealed higher accuracy, but required considerably more iterations. Further analysis of the absolute error in pressure $\|P_m - P_d\|_\infty$ shows the error oscillates at values between 10^{-10} and 10^{-11} . Using different suitable initial guesses, we observe that the multiscale method does in fact achieve considerable accuracy in the first iteration, but fails to improve this error significantly in subsequent iterations. This result indicates that the multiscale method gives a relatively accurate answer, but converges cannot achieve arbitrary accuracy even in the constant

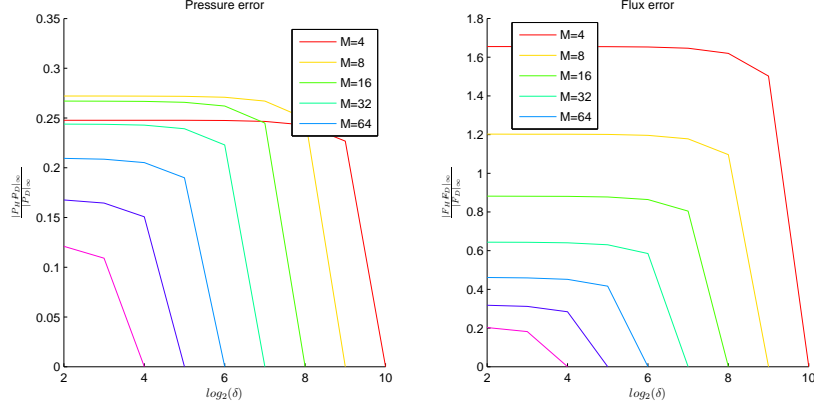


Figure 5.7: Experiment II Constant μ Analysis: Solid lines represent a constant number of sampling domains μ with relative errors displayed for pressure (left) and flux (right) in the linearly varying conductance case.

conductance case.

5.1.2 Experiment II

In experiment II, conductances remain constant along each vertical cross-section but vary linearly in the x-direction. We previously hypothesized that the structured nature of the conductance model would lead to fast convergence behaviors. Figures 5.7- 5.8 illustrate that the convergence behavior is much slower than expected. In Figure 5.7 shows the behavior as the number of sampling subdomains is held constant and the sample sizes successively double. It is easy to see that relative errors are high initially and do not decrease significantly until all possible information in the fully microscopic model is utilized.

Figure 5.8 illustrates the convergence behavior holding the total sampling area $\mu\delta$ constant and varying the number of sampling subdomains. We observe an interesting phenomenon: a slight initial increase in pressure errors when the number of sampling subdomains increases from $\mu = 2^2$ to $\mu = 2^3$. After this initial spike, the pressure errors decrease monotonically. The relative flux errors are significantly higher than the relative pressure errors in all cases except when $\mu\delta = 4096$. In other words, high accuracy is only achieved

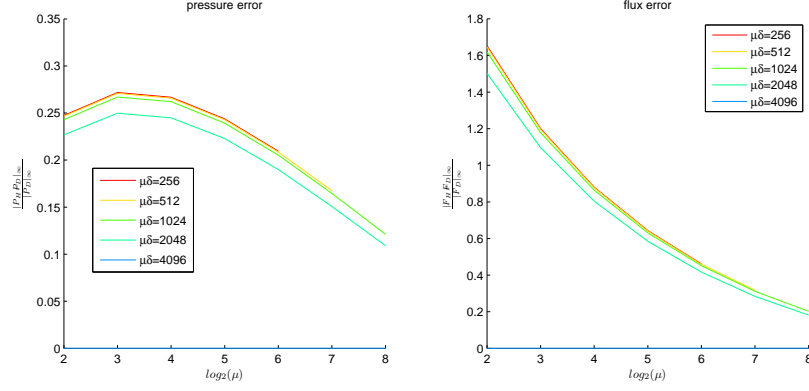


Figure 5.8: Experiment II Constant $\mu\delta$ Analysis: Solid lines represent a constant total sampling area $\mu\delta$ with relative errors displayed for pressure (left) and flux (right) in the linearly varying conductance case.

in the case when the total sampling area is equal to the total area of the domain. We interpret this case as a Domain Decomposition case because the subdomains form a complete, non-overlapping partition of the computational domain.

5.1.3 Experiment III

In experiment III, 100 tests were conducted using random conductances obtained from a uniformly random throat radii distribution. Each test consisted of fixing the conductance values initially and varying the number of sampling subdomains μ and sample size δ analogously as in Experiments I & II. After 100 tests, the results from each $\mu\delta$ combination are averaged and presented in figures 5.9- 5.10 with a logarithmic scale in the x-axis.

Figures 5.11- 5.14 compare a typical multiscale solutions to the solution of the fully microscopic model. The solid bold line represents the average pressures along each cross-section of the fully microscopic model at all points. The open circles at the end of each vertical line represents the approximated multiscale solution at the discrete point. Note that all error measures are the maximum difference between overlapping points between the macroscopic grid and the fully microscopic model. Observing these particular instances

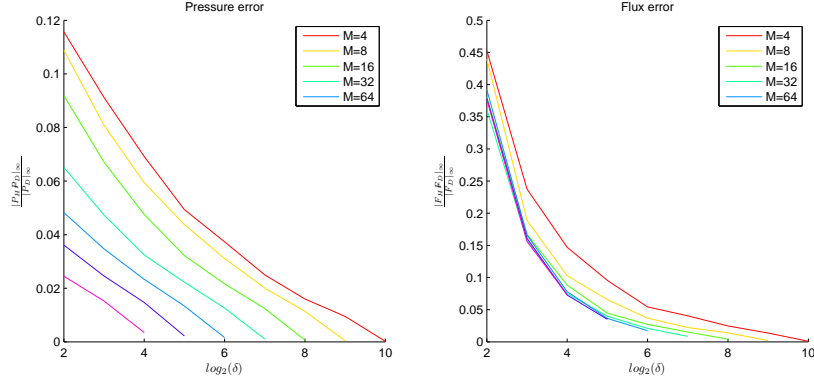


Figure 5.9: Experiment III Constant μ Analysis: Solid lines represent a constant number of sampling domains μ with relative errors displayed for pressure (left) and flux (right) in the random conductance case.

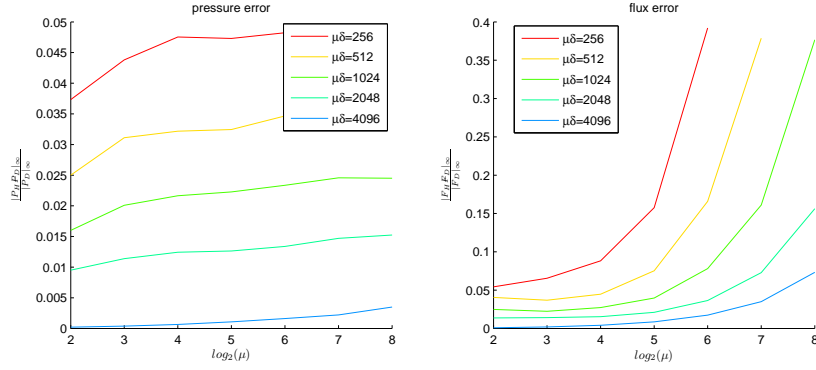


Figure 5.10: Experiment III Constant $\mu\delta$ Analysis: Solid lines represent a constant total sampling area $\mu\delta$ with relative errors displayed for pressure (left) and flux (right) in the random conductance case.

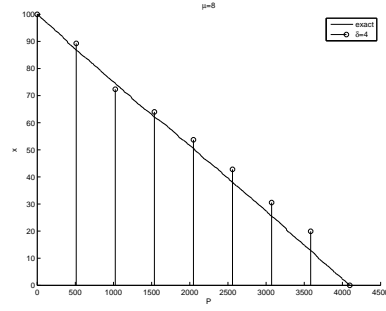


Figure 5.11: Comparison between the averaged fully microscopic solution and the multiscale solution with $\mu = 8$ subdomains and sample size $\delta = 4$.

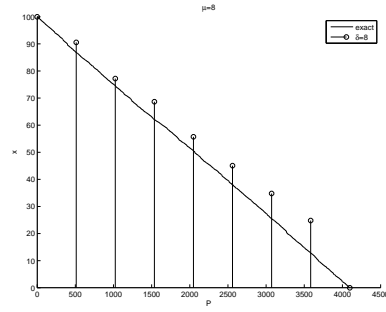


Figure 5.12: Comparison between the averaged fully microscopic solution and the multiscale solution with $\mu = 8$ subdomains and sample size $\delta = 8$.

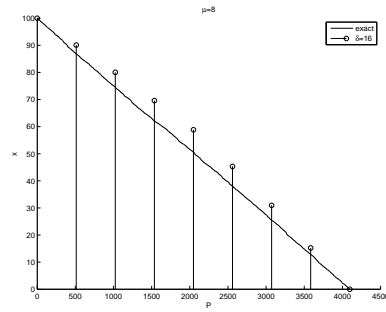


Figure 5.13: Comparison between the averaged fully microscopic solution and the multiscale solution with $\mu = 8$ subdomains and sample size $\delta = 16$.

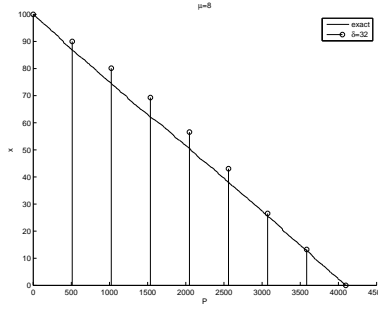


Figure 5.14: Comparison between the averaged fully microscopic solution and the multiscale solution with $\mu = 8$ subdomains and sample size $\delta = 32$.

may lead the reader to believe that smaller sample sizes (e.g. $\delta = 4$ in figure 5.11) lead to smaller errors than larger sample sizes (e.g. $\delta = 8$ in figure 5.12). However, the average trend as the sample size δ increases shows that the multiscale solution approaches the cross-section averaged solution of the fully microscopic model.

The results in figure 5.9 indicate that relative errors of both pressure and flux uniformly decrease when the number of sampling subdomains μ is held constant and the sample size δ increases. However, the results in figure 5.10 indicate that neither pressure nor flux achieve convergence when the total sampling area is constant and the number of sampling subdomains increases. In this case, the relative pressure error increases slightly, but the flux error increases dramatically.

Under analogous testing parameters, Chu et al.[26] encountered similar divergent tendencies. They reported that this lack of convergence is a byproduct of the constant boundary conditions imposed upon the local pore network models sampled from the fully microscopic model. The random distribution of conductances ensures that the true pressure across any vertical cross-section of the fully microscopic model is non-constant with probability 1. Hence, as more sampling subdomains are used, more vertical cross-sections are artificially held constant. This modeling error increases significantly and is in stark contrast to the convergence behavior observed in figure 5.9.

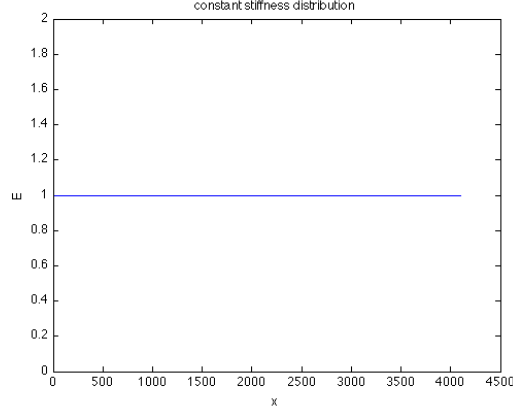


Figure 5.15: Stiffness distribution for Solid Deformation Case I.

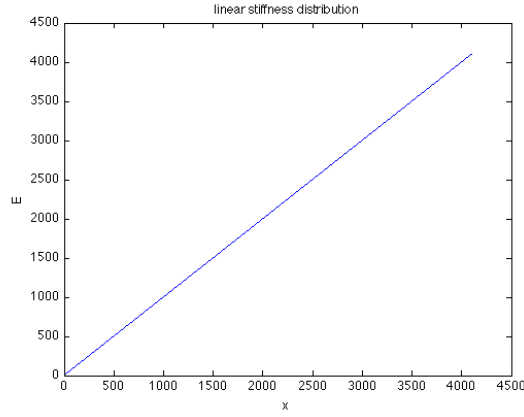


Figure 5.16: Stiffness distribution for Solid Deformation Case II.

5.2 Multiscale Solid Deformation

Like the multiscale flow experiments, we test the convergence of the multiscale deformation model with constant, linearly varying and random stiffnesses E_{ij} . Like the previous experiments, we use $E = 1$ for all springs in experiment I and $E(x) = x$ in experiment II. In experiment III, we choose stiffnesses from a uniformly random distribution in the interval $[1, 1000]$. Figures 5.15- 5.17 displays the stiffness distributions for the three experiments. Again, we choose the number of sampling subdomains μ and sample lengths δ as positive integer powers of two.

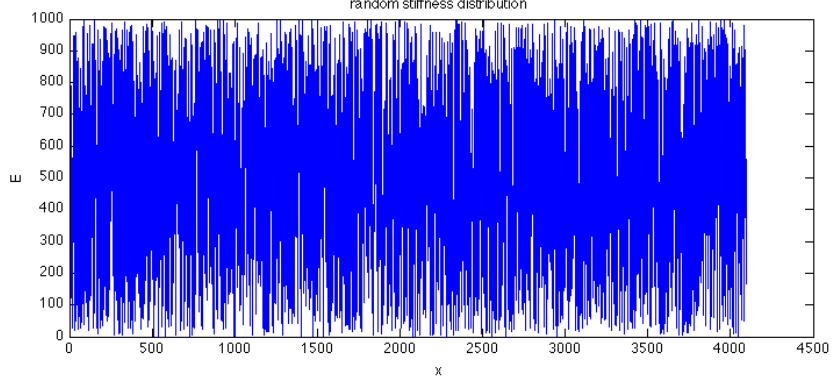


Figure 5.17: A random stiffness distribution for Solid Deformation Case III.

In all experiments, the fully microscopic model consists of $|\Omega| \equiv 2^8 = 4096$ spring elements with unit length and cross-sectional area. Consequently, we choose μ & δ as positive integer powers of two such that $\mu\delta \leq 4096$. We also impose purely dirichlet boundary conditions at the macroscopic level and compare the multiscale solutions to the solution of the fully microscopic model.

Based on the convergence behaviors observed in the multiscale flow algorithm, we predict that the multiscale deformation algorithm will have analogous behaviors. In Experiment I, we predict uniformly small relative errors in displacement and total force, regardless of the choice of μ and δ when all spring stiffnesses are constant. In Experiment II, we expect very small relative errors only when the multiscale model fully samples the underlying micro models; i.e. when $\mu\delta = 65,536$. In the case with μ constant and δ increases, we expect to see significant reduction in relative errors only when δ is large. In experiment III, we expect to observe convergence with μ constant and δ increasing, but not when $\mu\delta$ is constant and μ increasing.

5.2.1 Results

Figures 5.18- 5.23 show analogous convergence behaviors in displacement and total boundary force for the three cases considered as observed in the multiscale flow problem in the

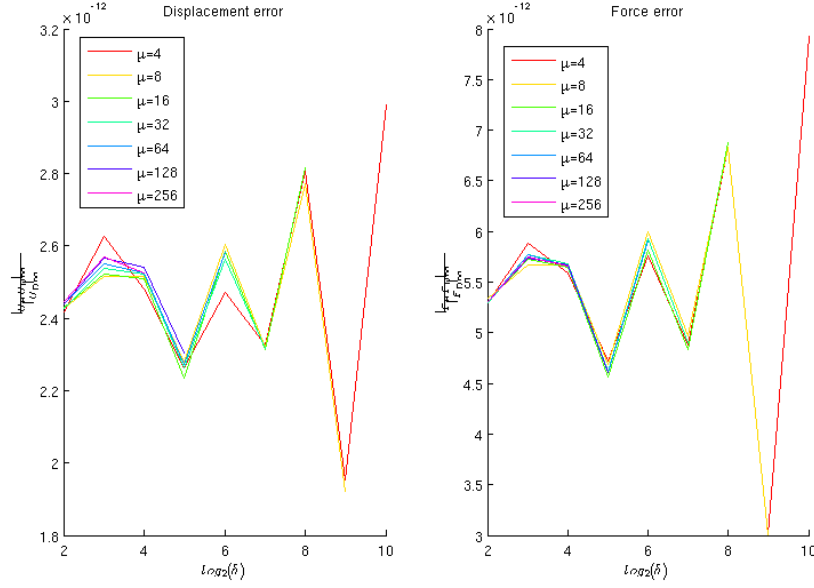


Figure 5.18: Multiscale deformation errors for constant stiffness and constant μ , varying sample size δ

previous section.

Small fluctuations in displacement and force errors exist when the stiffnesses are constant throughout the medium (figures 5.18- 5.19). The relative errors fluctuate within less than 10^{-11} , indicating nearly constant accuracy 5.18. Analysis with constant sampling area (figure 5.19) shows that as the number of sampling subdomains μ increases, the relative errors in displacement and force fluctuate closer and closer to approximate asymptotes at 2.4×10^{-12} and 5.2×10^{-12} , respectively. The small relative errors across all simulations indicates that the multiscale algorithm converges with reasonable accuracy in the constant stiffness case.

Figures 5.20- 5.21 illustrate the convergence behavior for a medium with linearly increasing stiffness. An analogous phenomenon occurs as discovered in Experiment II of the multiscale flow problem in the previous section. Initial relative errors are large, but incrementally decreases as the sample size increases. In the simulations with full sampling $\mu\delta = |\Omega| = 4096$, relative errors are significantly smaller (relative error $< 10^{-10}$) than all

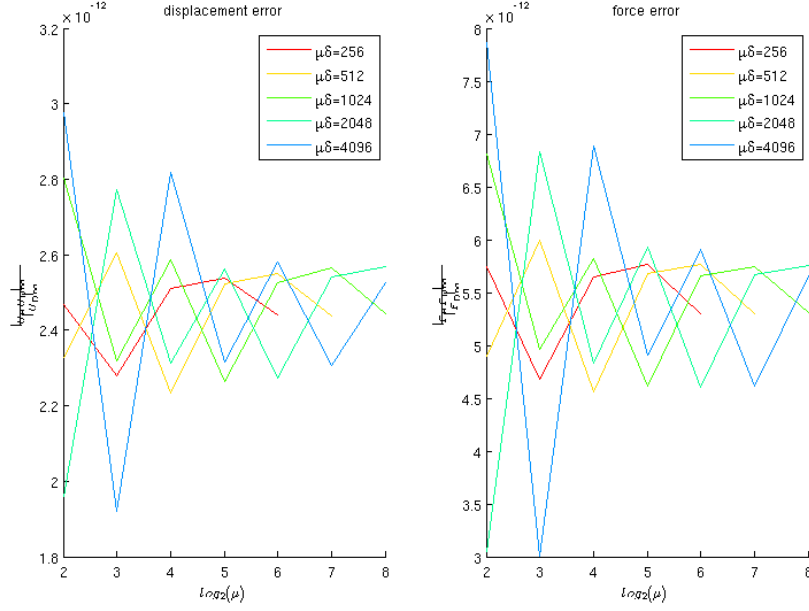


Figure 5.19: Multiscale deformation errors for constant stiffness and constant sampling area $\mu\delta$, varying number of sampling subdomains μ

other simulations. This indicates that the multiscale algorithm operates most effectively as a full domain decomposition method in this case. Holding μ constant, we observe uniform decrease in error as δ (figure 5.20) increases. Maintaining a constant sampling area $\mu\delta$, we observe a slight initial increase in relative error as μ increases from 2^2 to 2^3 sampling subdomains. After this initial increase, all other errors decay uniformly with increasing μ .

Figures 5.22- 5.23 illustrate the resulting averaged relative errors after 100 tests with uniformly random distributed stiffnesses $E \in [1, 1000]$. Figure 5.22 apparently illustrates that both displacement and force errors decrease uniformly with increasing μ and δ . However, Figure 5.22 clearly shows that the algorithm is divergent in displacement and force for constant $\mu\delta$ and increasing μ .

These results are consistent with the multiscale flow simulations in the previous chapters and with the results in [26, 25]. In [26, 25], they tested a fully two dimensional microscopic flow model with a one dimensional macroscopic model. They attributed lack of convergence

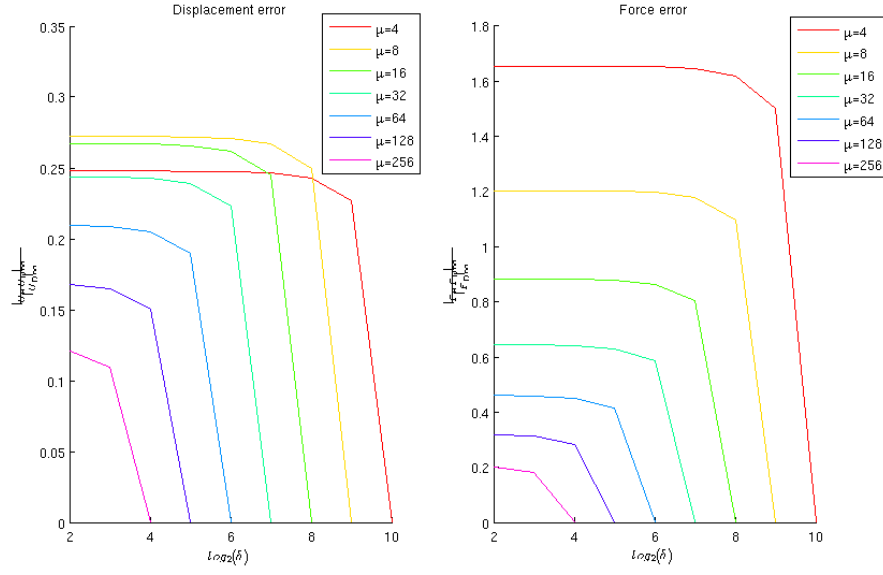


Figure 5.20: Multiscale deformation errors for linearly increasing and constant μ , varying sample size δ

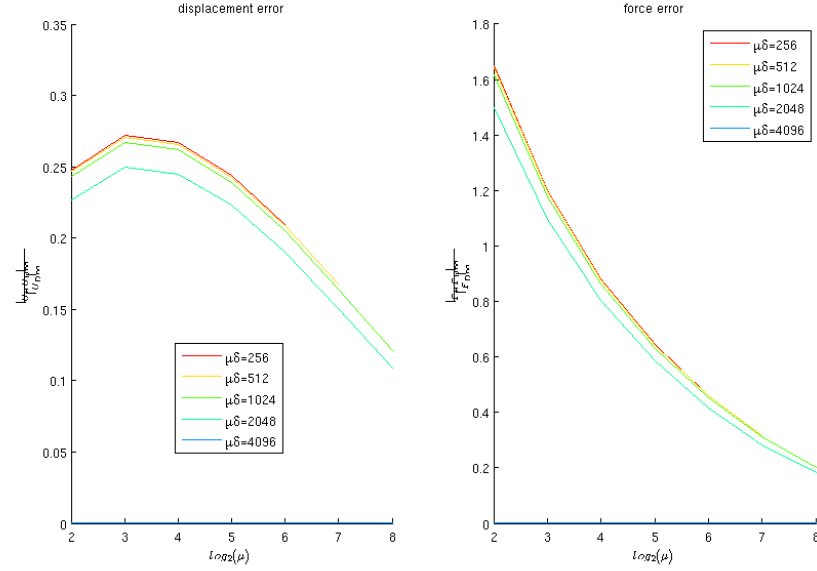


Figure 5.21: Multiscale deformation errors for linearly increasing stiffness and constant sampling area $\mu\delta$, varying number of sampling subdomains μ

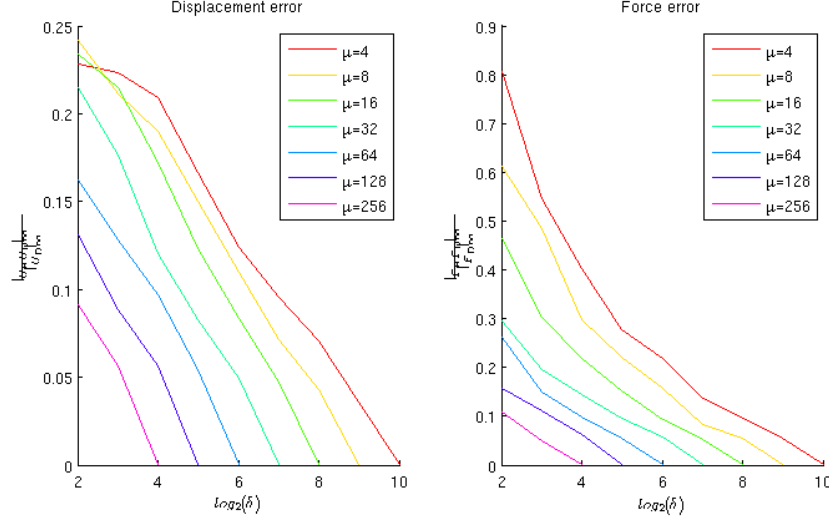


Figure 5.22: Average multiscale deformation errors for 100 random stiffness tests with constant μ , varying sample size δ

to the artificially constant dirichlet boundary condition imposed on vertical cross-sections of the two dimensional model despite non-constant (random) conductances along these cross-sections. It was argued that larger numbers of sampling subdomains μ result in more micro models with artificially constant dirichlet conditions and thus greater errors. Our results indicate that this may not be entirely accurate. Our model uses a one-dimensional fully microscopic and macroscopic model, but results in analogous divergent behavior as μ increases. We explore possible explanation of this phenomenon in the next chapter.

5.3 Multiscale Elliptic Reaction-Diffusion

We use the same testing framework as introduced in section 5.1 to test our multiscale elliptic reaction diffusion algorithm to solve

$$-\frac{d}{dx} \left(K(x) \frac{dp}{dx} \right) + c^* P = f.$$

The fully microscopic model is a two dimensional rectangular lattice network model with 4096×10 edges, each of unit length; yielding a one dimensional macroscopic domain

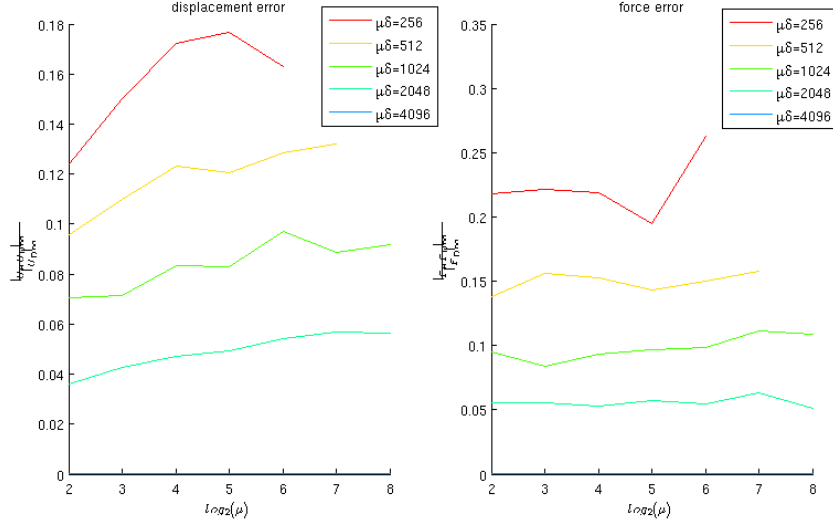


Figure 5.23: Average multiscale deformation errors for 100 random stiffness tests with constant sampling area $\mu\delta$, varying number of sampling subdomains μ

$\Omega \equiv [0, 4096]$. We impose purely dirichlet boundary conditions $P_L = 100$ and $P_R = 0$ at the left and right cross-sectional boundaries of model. We use its solution as the basis of comparison with the multiscale method. Again, we choose μ and δ as positive integer powers of two such that $\mu\delta \leq 4096$ and compare the multiscale solution to the fully microscopic solution.

In this case, we examine the convergence behavior of the constant coefficient case with $K(x) = 1$ and the linear case with $K(x) = x$. Without loss of generality, we choose $c^* = 1$ in both cases. We only measure the relative pressure error measure in the L^∞ norm and do not consider the flux error. For additional comparison, we also compute errors in the finite difference solution on a mesh with $N = \mu$ equispaced intervals. The finite difference method uses a 2nd order centered spatial difference to approximate the second derivative term in the PDE. We hypothesize that the relative errors will be consistent with the behavior observed in the previous two sections. That is, we suspect relative errors on the order of 10^{-12} in all cases, with some fluctuations no greater than 10^{-11} . We also

hypothesize no significant difference between the finite difference and multiscale solutions for a given $\mu = N$.

5.3.1 Results

Figure 5.24 depicts the exact, finite difference, and multiscale solutions on a logarithmic y-axis for a given $N = \mu$ and sample length $\delta = 4$. Visually, it appears as though the non-linear nature of the fully microscopic solution is more easily captured by both the finite difference and our multiscale method when the number of macroscopic gridpoints increases. Examination of the relative errors in tables 5.1- 5.2, however, suggests a different story. As the macroscopic grid refines, larger errors are incurred in both the finite difference and multiscale methods. This apparent divergence is simply a by-product of the scale of heterogeneity in the true solution itself. At a very small length scale, the solutions sharply drop from the left boundary condition value $P_L = 100$ to nearly 0. Though the mesh is refined, the spatial stepsize is never completely refined to scales smaller than the finite interval containing this drop; neither for the finite difference nor for the multiscale model. Thus, the discrete solutions increase in absolute error as they approximate the large initial drop in values.

Figure pairs 5.26- 5.27 and 5.28- 5.29 show the convergence behavior for the constant and linearly varying conductance cases, respectively. In the constant case, our multiscale method converges to more accurate solutions than the finite difference solution as the sample lengths δ increase. As the number of sampling subdomains μ increases, errors apparently increase. However, as with the finite difference method, this is a byproduct of the inability of the macroscopic grid to capture the behavior in the heterogeneous region near the left boundary condition.

The linearly varying case exhibits dramatically distinct behavior in comparison to the analogous cases for solid deformation and Chu et al.'s model. Figure 5.25 shows that the non-constant conductance intensifies the decay in the solutions. This decay is illustrated by the smaller boundary layer near the x_0 . The multiscale method's convergence more

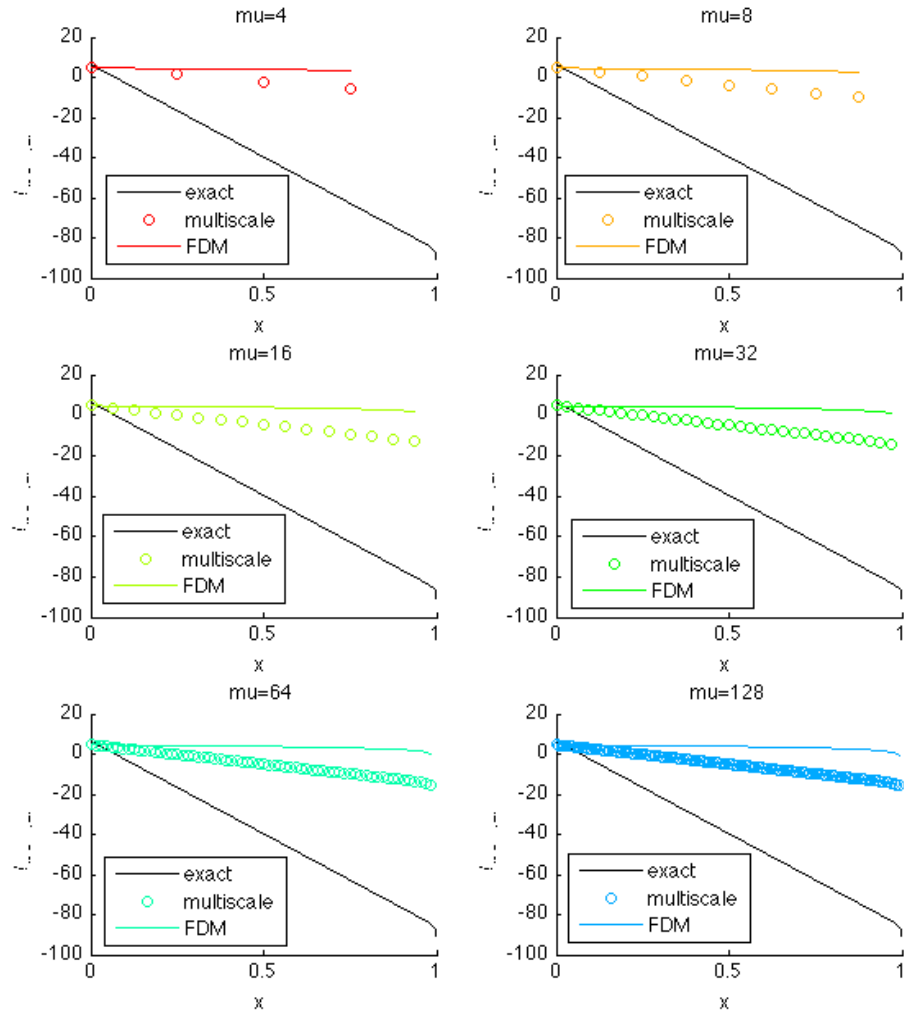


Figure 5.24: Exact, finite difference, and multiscale solutions to the reaction-diffusion equation with constant conductance $K(x) = 1$ and various number of sampling subdomains μ and $\delta = 4$. All graphs are plotted with a logarithmic scale on y-axis.

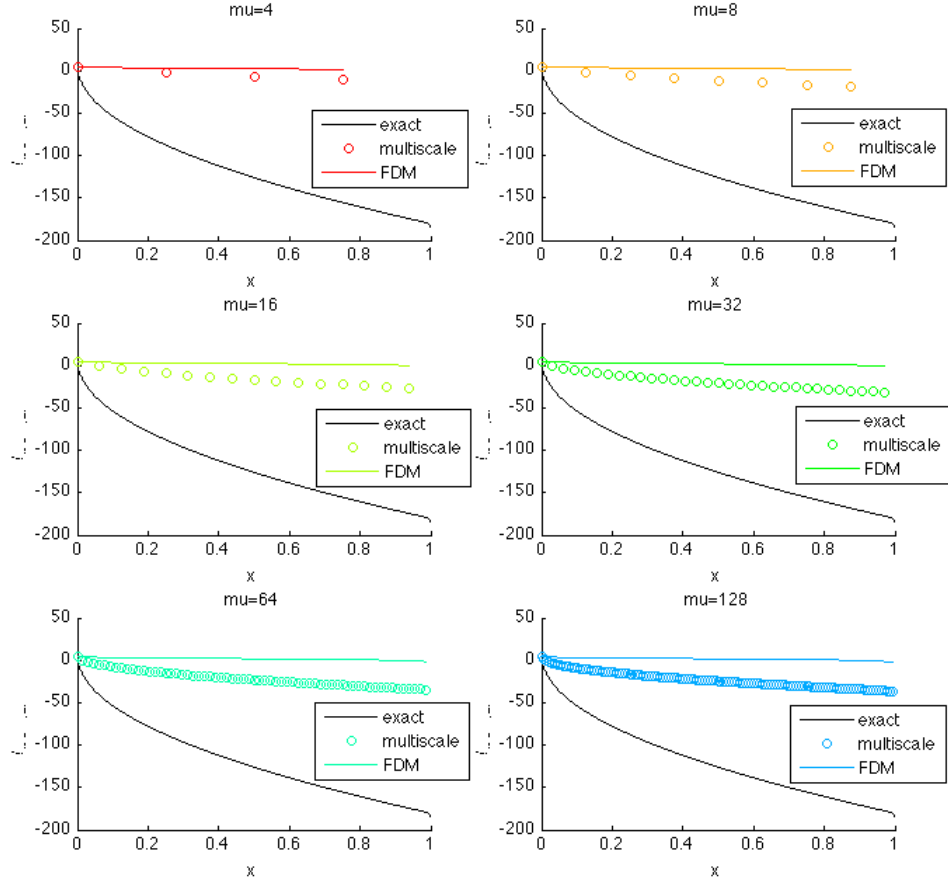


Figure 5.25: Exact, finite difference, and multiscale solutions to the reaction-diffusion equation with linearly increasing conductance $K(x) = x$ and various number of sampling subdomains μ and $\delta = 4$. All graphs are plotted with a logarithmic scale on y-axis.

Table 5.1: Relative Error in multiscale model solution w.r.t. fully microscopic model in the constant conductance case

		δ						
		4	8	16	32	64	128	256
μ	4	1.1154e-08	2.1192e-14	3.8248e-26	8.2631e-98	7.2690e-194	0	0
	8	8.9059e-08	6.7419e-13	1.9318e-23	7.9306e-45	6.6827e-88	2.3726e-174	9.9233e-215
	16	7.0971e-07	2.1325e-11	9.6264e-21	9.8081e-40	5.0910e-78	9.9616e-108	9.9616e-108
	32	5.6340e-06	6.6683e-10	4.6706e-18	1.1457e-34	3.1562e-54	3.1562e-54	
	64	4.4385e-05	2.0390e-08	2.1512e-15	1.7646e-27	1.7766e-27		
	128	3.4443e-04	5.9735e-07	8.5496e-13	4.2149e-14			
	256	2.5905e-03	1.5969e-05	2.0499e-07				

closely resembles the behavior of the constant case in the reaction diffusion problem. That is, the relative errors decrease significantly as the number of sampling subdomains μ is held constant and the sample length increases. However, holding the total sampling area $\mu\delta$ constant and increasing μ , relative errors increase. This behavior is akin to the divergent behavior observed in the random heterogeneous cases for solid deformation and Chu et al.'s model. This increase in error is reflective of the macroscopic grid's inability to capture a steep, continuous gradient in a boundary layer near x_0 .

The results above suggest that application to the heterogeneous (random) case would exhibit similar characteristics. At first glance, figure 5.30 seems to indicate positive results. Upon closer inspection, we observed two unexpected tendencies in our numerical results. First, the algorithm frequently generates ill-conditioned macroscopic matrix systems. The ill-conditioned systems are a consequence of the iterative algorithm approximating values less than machine precision and can be avoided by carefully choosing the convergence criterion. Secondly, and more problematically, the algorithm often generated negative pressure and flux values. Further investigation revealed that monotonicity was not preserved in the micromodels. That is, given boundary conditions Clearly, the lack of source terms in

N	Relative Error
4	1.1154e-08
8	8.9059e-08
16	7.0971e-07
32	5.6340e-06
64	4.4385e-05
128	3.4443e-04
256	2.5905e-03

Table 5.2: Relative Error in finite difference solution w.r.t. fully microscopic model

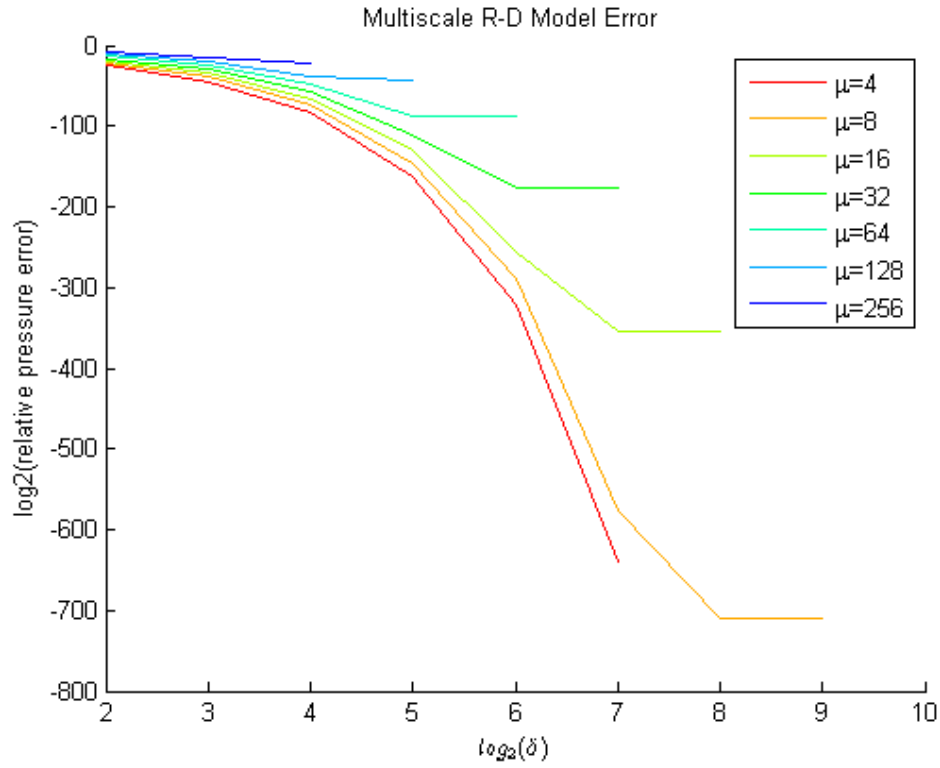


Figure 5.26: Logarithms of relative pressure error for Multiscale Reaction-Diffusion PDE with constant conductance; holding μ constant and increasing δ .

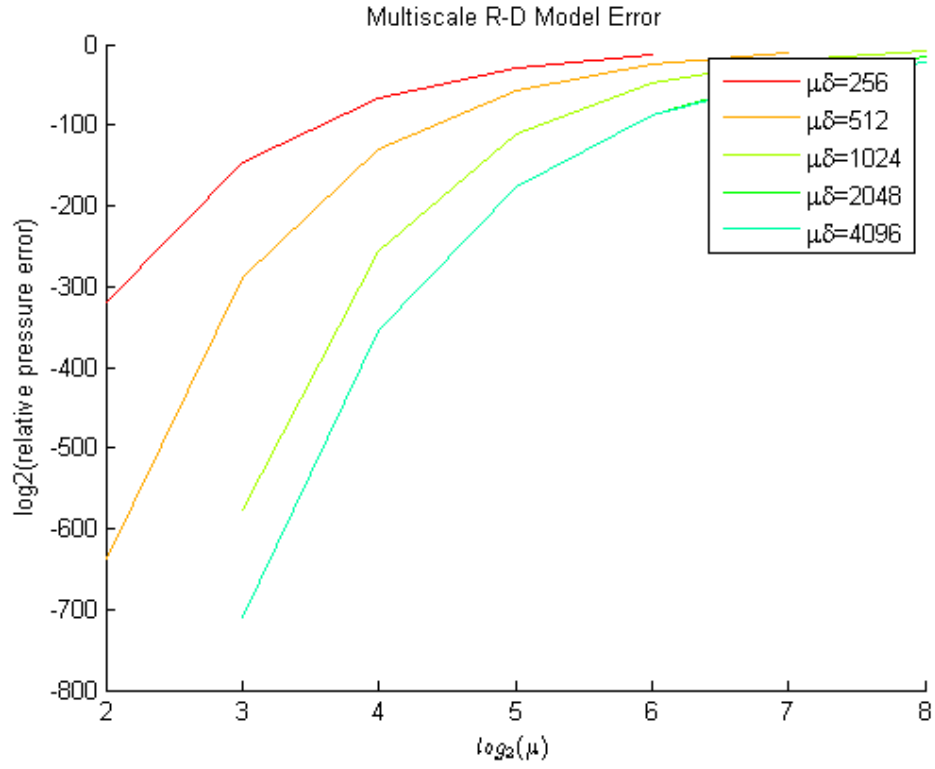


Figure 5.27: Logarithms of relative pressure error for Multiscale Reaction-Diffusion PDE with constant conductance, holding total sample area $\mu\delta$ constant and increasing μ

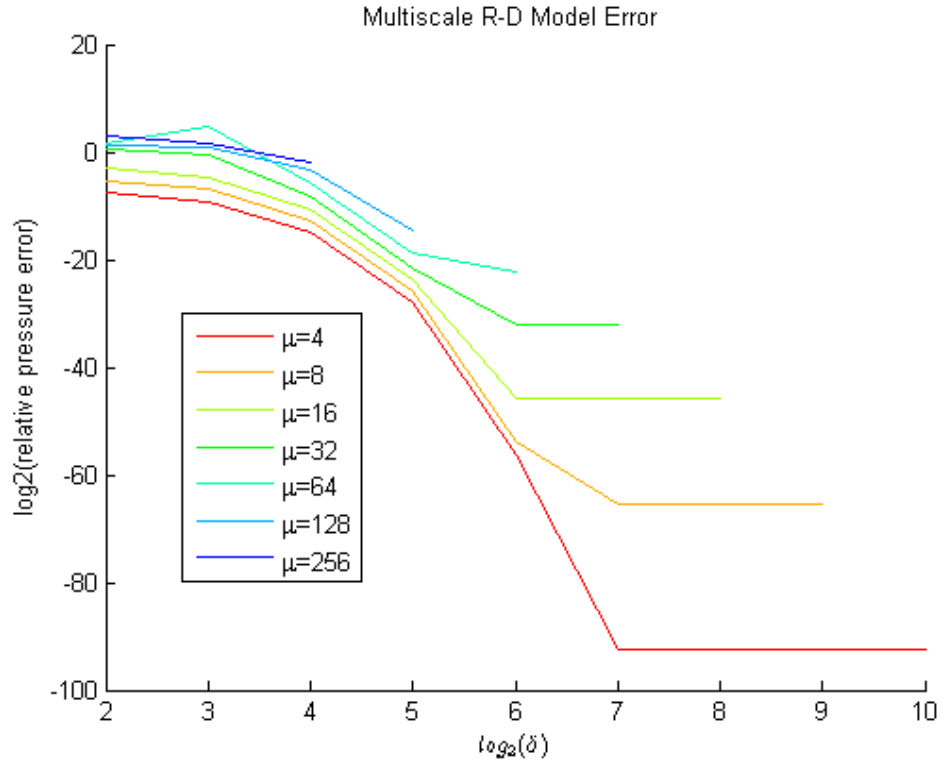


Figure 5.28: Logarithms of relative pressure error for Multiscale Reaction-Diffusion PDE with linearly varying conductance, holding μ constant and increasing δ .

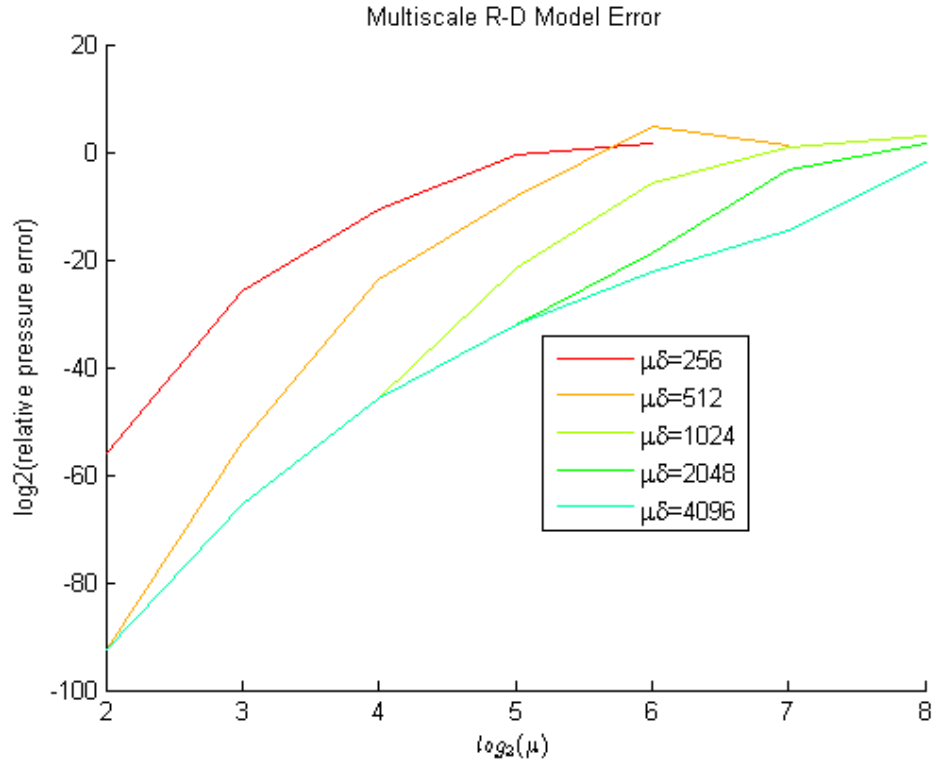


Figure 5.29: Logarithms of relative pressure error for Multiscale Reaction-Diffusion PDE with linearly varying conductance, holding total sample area constant $\mu\delta$ and increasing μ .

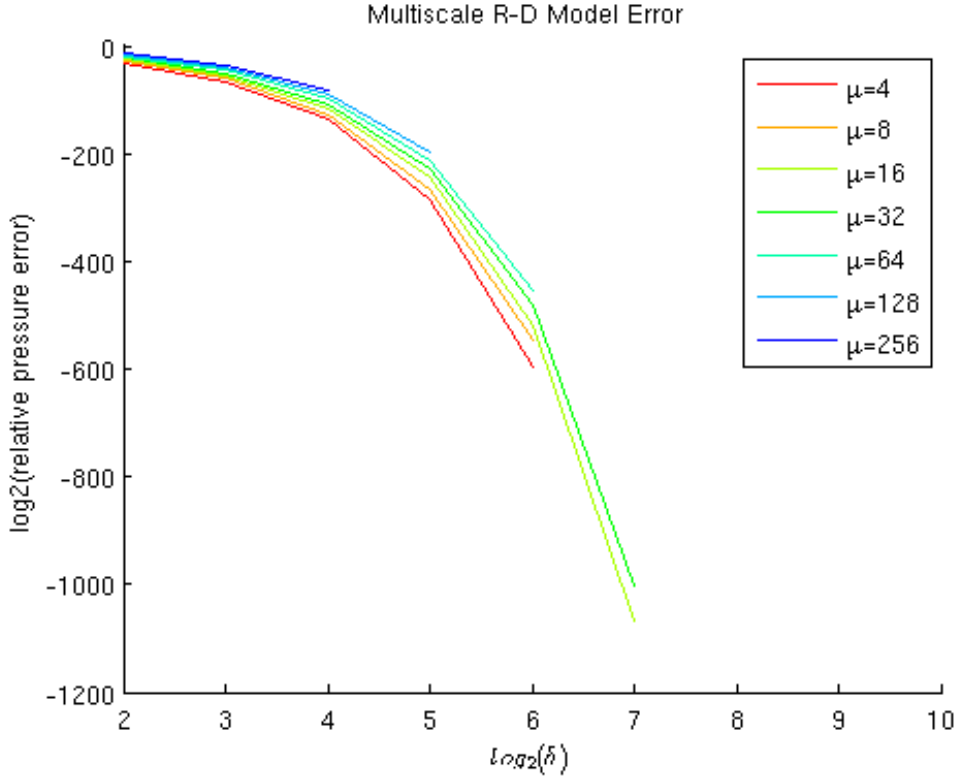


Figure 5.30: Logarithms of average relative pressure error for Multiscale Reaction-Diffusion PDE with random conductance, holding μ constant and increasing δ .

the elliptic PDE suggests that pressure values be bounded by the boundary conditions. Monotonicity in the solution also suggests that flux values also be non-negative for a negative pressure gradient. Lack of these two properties suggests that the proposed microscale model may not approximate the heterogeneous case effectively.

Chapter 6

Discussion

6.1 Operator Splitting

It was predicted in chapter 3 that the proposed block operator splitting method is conditionally convergent. Our numerical experiments characterize both the range of problems for which the operator splitting methods converge and their corresponding rates of convergence. We found no qualitative difference between the Block Jacobi and Block Gauss-Seidel Splitting methods.

6.1.1 Key Findings

In the homogeneous material property case, non-dimensionalization revealed that the product between the constrained specific storage coefficient and the elastic moduli $\beta = c_0\nu$ adequately characterizes the convergence behavior for constant Biot-Willis Coefficient α . We define a threshold surface β^* for each α which separates the parameter space into problems guaranteed to converge or diverge for each choice of Δt and Δx . As $\alpha \rightarrow 0$, the surface uniformly decreases to the plane $\beta = 0$. This corresponds both to a larger range of parameter values which converge and faster convergence rates. The physical interpretation of this limit is a characterization of a weakened coupling between the fluid flow and deformation processes. Moreover, the threshold surface β^* always approaches a limiting plane parallel to the Δx - Δt plane, above which convergence is assured. In the strongly-coupled case with $\alpha = 1$, the limiting plane is given by $\beta = 1$. This result indicates that problems with $\beta > 1$ are guaranteed to converge with a rate of convergence that increases as β increases.

We use the characterization of the homogeneous case to guide our tests of the linearly variable coefficient case with $\nu(x) = k(x) = mx + b$. We find that the increases in slope m shift the threshold surfaces toward the origin, enabling the convergence of the operator splitting for a larger set of problems. However, the slope does not lower the value of the limiting plane which the threshold surface does not cross. This limiting plane is strongly affected by variations in c_0 and α . Again as $\alpha \rightarrow 0$, the strength of the coupling decreases and the limiting plane also decreases with it.

More importantly, large material property gradients result in a wider range of convergent problems for larger values of Δt and Δx . This suggests that larger heterogeneity results in improved convergence of the operator splitting method. In the context of multiscale poroelasticity, this is significant because we wish to approximate the solution on a coarse mesh corresponding to Δx larger than the scale of the heterogeneity. Further testing is needed to determine if this trend holds true for highly oscillatory material coefficients with large amplitudes.

6.1.2 Limitations

The numerical experiments give evidence that the threshold surface separating convergent and divergent problems for our operator splitting method approaches an asymptotic limit as Δt and Δx approach zero. This is, by no means, an analytical proof of the limit. Given the complexity of determining the analytical form of the spectral radius of the stationary operator $M^{-1}N$, this is our best attempt to characterize the parameter space which guarantees convergence.

These results only apply to the case linear heterogeneity and with $\nu(x) = k(x)$ only. Because of the infinitely many possible choices of functions $\nu(x)$ and $k(x)$, it is impossible to characterize all possible variations and permutations. One particular case of interest not addressed by this thesis is the case with highly oscillatory $\nu(x)$ and $k(x)$. This is an important benchmark case for a multiscale method for poroelasticity and we seek to test this case in the future for various amplitudes and frequencies.

Number of iterations needed to achieve convergence within a given error tolerance is a significant drawback to the proposed operator splitting method. As the material parameter values approach the threshold surface, more iterations are required for the operator splitting method to converge. The computational cost of multiple iterations using the operator splitting method can supersede the cost of a single solve of the fully coupled equations.

The proposed operator splitting methods are pure decompositions of the coupled operator at a specific time t . In the block gauss-seidel splitting methods, the unmodified solution from one equation is used as a source term in the remaining equation without projective corrections. In the framework of fixed point iterations, various acceleration methods can be employed to improve the rate of convergence. Most notably, successive overrelaxation, Aitken, Chebyshev, and various krylov methods can be used to accelerate its convergence. An ideal method enables convergence in a fixed number of iterations independent of parameter values and spatiotemporal discretization. Use of Kim[46]’s projective corrections may significantly improve the convergence rates, but it remains unclear if these methods can be extended to the variable coefficient case.

The current thesis assumes heterogeneous mobility K and elastic moduli material parameters ν without regard to their correlation with the specific storage coefficient c_0 and the Biot-Willis Coefficient α . In the homogeneous case, α and c_0 depend on other material properties which may vary in space as well. We aggressively assume α and c_0 are constant throughout the medium. Though characterization of their spatial variations is beyond the scope of this thesis, their variations may impact the applicability of our results to general multiscale poroelasticity problems.

6.2 Multiscale Methods

As a component of treating the multiscale nature of the poroelasticity equations, the current thesis sought to develop a multiscale method for the decoupled solid deformation and fluid flow equations resulting from the proposed operator splitting method. Our method is

uses finite volume method at the macroscopic scale and discrete network models at the microscale. In particular, a microscopic reaction-diffusion model was proposed to resolve the fluid flow equation.

6.2.1 Key Findings

In the course of attempting to replicate the results of Chu et al.’s multiscale algorithm, we implemented and tested their algorithm for diffusion in porous media in three benchmark cases; two of which were not addressed in their original paper: Homogeneous and Linearly Variant conductances. In addition to replicating the results for the heterogeneous (random) conductance case, we discovered two important facts about the algorithm. Firstly, in the case of the Hagen-Poiseuille conductance model, Chu et al. (2012) claimed that convergence is theoretically attained in a single iteration within machine precision. Our results indicate that residual error decreases significantly in the first iteration, but not necessarily to within machine precision even in the homogeneous conductance case. This indicates that we cannot impose excessively small error tolerances between the multiscale and fully microscopic solutions, even in the most idealized circumstances.

Secondly, while convergence is achieved in the linearly variant conductance case, significant relative errors exist when subsampling is used. In this case, relative errors are only small when fully micro sampling is used. The only case in which subsampling proved efficient is in the heterogeneous (random) conductance case. In the heterogeneous case, we confirm that convergence is achieved when the number of sampling subdomains μ is held constant and the length of the samples δ increases but not vice-versa. Constant δ and increasing μ results in increasing relative errors both in pressure and flux. Similar trends were also reported in Chu et al. (2012).

We proposed a method for multiscale solid deformation in 1D based on coupling finite volume method at the macroscopic level with direct stiffness methods at the microscopic level. We achieved analogous convergence behavior for the homogeneous, linearly variant, and heterogeneous cases in comparison to the aforementioned replication tests. Our results

indicate a similar lack of convergence in the heterogeneous case with constant sample length δ and increasing the number of sampling subdomains μ . Chu et al. (2012) claimed this behavior to be the result of the imposition of uniform dirichlet boundary conditions along cross-sections of the fully microscopic model with non-uniform conductances. Since our micromodel is 1D, this behavior cannot be attributed to this phenomenon. It is clear that the use of purely dirichlet boundary conditions in the micromodel contains within it inherent errors that amplify with increasing sampling subdomains. The exact source of these errors is unknown and requires further testing.

We also proposed a method to solve the multiscale reaction-diffusion problem resulting from the decoupled flow problem. Our method proposed an alternative network model which accounts for the reaction term in the macroscopic equation. The characteristics of the test problem produce a boundary layer which is difficult to capture even in the constant coefficient case with finite difference method. Our preliminary results indicate that our multiscale algorithm produces more accurate results than the standard finite difference method for the constant and linearly varying coefficient cases. The heterogeneous (random) case produced inconsistent convergence results related to negative fluxes generated in the reaction-diffusion micromodels. Despite the use of purely dirichlet boundary conditions in the axial directions and periodic boundary conditions along the transverse boundaries, monotonicity was not preserved in the micromodel. Further investigation is required to determine the exact cause of the negative fluxes.

6.2.2 Limitations

The constant coefficient cases of solid deformation and Chu et al.’s method reveals that the multiscale method does not achieve accuracy to approximately machine precision. We note that Chu et al. never disclosed results in the constant coefficient or linearly increasing case. Furthermore, the micromodels in our method utilized a distinct topological structure in comparison to Chu et al.’s work. In our models, we use connectivity number 4 and 2 in the replication study and the solid deformation model, respectively while Chu et al. (2012)

used connectivity 6 arranged in a triangular mesh structure. We hypothesize the difference in performance results may partially be attributed to this difference.

Except for the constant coefficient cases, significant sampling area is always required to achieve small relative errors in Chu et al.’s model and the multiscale solid deformation model. Particularly in the linearly variant case, relative errors do not diminish significantly except in the case of full sampling of the microscopic model. While this appears to be a significant limitation of the method, one must keep in mind that it is inherently unrealistic to expect large accuracy using extremely small sampling subdomains in a multiscale method. The fact remains that convergence is achieved in the limit as the total sampling area approaches the size of the full computational domain. For many engineering applications, relative error less than 5% may be adequate. It remains unclear, however, how significant the impact of the relative error in the multiscale method is on the convergence of the operator splitting method. Further testing is required to determine the scope of this impact.

Extensions of the multiscale method to higher dimensions is a bit more problematic in the case of solid deformation. Static determinacy limitations and lack of shearing effects severely reduce the use of truss-elements to the one dimensional case only. Moreover, the discrete nature of the fully microscopic model necessitates that the sample length δ cannot be chosen smaller than the length of the elements of the micromodels (e.g. the length of the throat in a pore network model). The assumption is that the underlying microstructure is known exactly and can be represented as a discrete graph. If the material properties $\nu(x)$ and $k(x)$ are given as smooth functions, we may substitute the discrete network models for other continuous representations. Our heterogeneous multiscale framework enables us to use any suitable microscale model which approximates the flux locally within each sampling subdomain. In this case, we may also use traditional numerical techniques such as finite difference or finite element method. To maintain higher order accuracy approximations of the flux, a mixed finite element method may prove to be ideal in this case.

Chapter 7

Future Work

The current thesis analyzed the operator splitting and multiscale methods separately as modules of the same framework. Our future work seeks to incorporate the methods together. In order to do this, three primary issues must be addressed:

- Alternative restriction operators & data estimators to incorporate mixed dirichlet-neumann boundary conditions.
- Projection of source terms onto microscale models
- Development of a multiscale elliptic reaction-diffusion model for the heterogeneous (random) case.

Our multiscale poroelasticity problem is subject to mixed dirichlet-neumann boundary conditions while our multiscale were only tested for purely dirichlet boundary conditions. Alternative methods are required to incorporate these multiscale methods within the scope of the proposed operator splitting framework. We propose an algorithm which constructs successive iterations that preserve the mixed boundary conditions and linearly interpolates both the dirichlet and neumann conditions onto micromodel boundaries.

Source terms in the operator splitting method originate from the decoupled gradient and divergence operators in the poroelasticity equations. As the pressure and displacement field variables lie on a staggered grid, their values fall on the boundaries of the control volumes and are non-trivially distributed to either micromodel. We propose an averaging approach in which the total contribution of source terms on control volume boundaries is divided equally to the two control volumes connected to the boundary. Compatibility

between the total source term in the control volume and the micromodel must also be preserved. We propose an equal distribution of the total control volume source term to the sampling subdomain's source terms.

The multiscale reaction-diffusion model apparently fails to converge in some of the heterogeneous (random) tests due to a lack of monotonicity preservation. We hypothesize that the micromodel's reaction term's coefficient may not be appropriately scaled. In our future work, we seek to test an alternative micromodel with scaling based on the internodal length of fully microscopic model L instead of the macroscopic spatial stepsize Δx . Fortunately, our operator splitting method is in a sufficiently generalized form such that any multiscale method applicable to the decoupled diffusion and reaction diffusion equation can be used. We may explore alternative multiscale methods for the elliptic reaction diffusion equation if the proposed modifications do not result in adequate convergence results.

Regardless of the multiscale method chosen for either the solid deformation or the flow equation, it is absolutely necessary to preserve higher order accuracy in the multiscale methods to ensure convergence of the fixed point iteration. Since the multiscale solution of one problem must necessarily be used as the source term of the other, relative errors may result in divergence of the fixed point iteration. Ultimately, we seek the highest amount of accuracy achievable using as little microscopic information as possible. As part of our future work, we will determine the amount of accuracy required in the decoupled solutions to ensure convergence in the fixed point iteration.

References

- [1] G Aguilar, F Gaspar, F Lisbona, and C Rodrigo. Numerical stabilization of biot's consolidation model by a perturbation on the flow equation. *International journal for numerical methods in engineering*, 75(11):1282–1300, 2008.
- [2] Ravi Appana. *Aquifer and Shallow San Andreas Fault Permeabilities Inferred from Poroelastic Modeling of InSAR Measurements of Land Surface Deformation in Coachella Valley, California*. PhD thesis, UNIVERSITY OF MINNESOTA, 2009.
- [3] Todd Arbogast and Hailong Xiao. A multiscale mortar mixed space based on homogenization for heterogeneous elliptic problems. *SIAM Journal on Numerical Analysis*, 51(1):377–399, 2013.
- [4] Christoph H Arns, Mark A Knackstedt, W Val Pinczewski, and Edward J Garboczi. Computation of linear elastic properties from microtomographic images: Methodology and agreement between theory and experiment. *Geophysics*, 67(5):1396–1405, 2002.
- [5] Natalie K Axtell, Moongyu Park, and John H Cushman. Micromorphic fluid in an elastic porous body: blood flow in tissues with microcirculation. *Int J Multiscale Comput Eng*, 3(1), 2005.
- [6] Juarez S Azevedo, Márcio A Murad, Marcio R Borges, and Saulo P Oliveira. A space–time multiscale method for computing statistical moments in strongly heterogeneous poroelastic media of evolving scales. *International Journal for Numerical Methods in Engineering*, 90(6):671–706, 2012.
- [7] Alireza Bahraminasab, S Mehdi Vaez Allaei, Farhad Shahbazi, Muhammad Sahimi, MD Niry, and M Reza Rahimi Tabar. Renormalization group analysis and numerical simulation of propagation and localization of acoustic waves in heterogeneous media. *Physical Review B*, 75(6):064301, 2007.

- [8] Miao Bai and Derek Elsworth. *Coupled processes in subsurface deformation, flow, and transport*. ASCE Publications, 2000.
- [9] SI Barry and GN Mercer. Flow and deformation in poroelasticity: unusual exact solutions. *Mathematical and computer modelling*, 30(9):23–29, 1999.
- [10] J Bear and MY Corapcioglu. Centrifugal filtration in deformable porous media. *A Series of Four Papers on Water Flow in Deformable Porous Media. Technical Report UMR-0284, Department of Civil Engineering, University of Michigan, Ann Arbor, Michigan, Section I*, 1981.
- [11] Jacob Bear and M Yavuz Corapcioglu. Mathematical model for regional land subsidence due to pumping: 1. integrated aquifer subsidence equations based on vertical displacement only. *Water Resources Research*, 17(4):937–946, 1981.
- [12] Michele Benzi, Gene H Golub, and Jörg Liesen. Numerical solution of saddle point problems. *Acta numerica*, 14(1):1–137, 2005.
- [13] James G Berryman. Comparison of upscaling methods in poroelasticity and its generalizations. *Journal of Engineering Mechanics*, 131(9):928–936, 2005.
- [14] William Bickford. *A first course in the finite element method*. Irwin, 1990.
- [15] M.A. Biot. General theory of three-dimensional consolidation. *Journal of applied physics*, 12(2):155–164, 1941.
- [16] MA Biot. Theory of deformation of a porous viscoelastic anisotropic solid. *Journal of Applied Physics*, 27(5):459–467, 1956.
- [17] MA Biot. Generalized theory of acoustic propagation in porous dissipative media. *The Journal of the Acoustical Society of America*, 34(9A):1254–1264, 1962.
- [18] Maurice A Biot and DG Willis. The elastic coefficients of the theory of consolidation. *J. appl. Mech*, 24(594-601):206, 1957.

- [19] John R Booker and John Phillip Carter. Analysis of a point sink embedded in a porous elastic half space. *International Journal for Numerical and Analytical Methods in Geomechanics*, 10(2):137–150, 1986.
- [20] JR Booker and JC Small. Finite layer analysis of consolidation. i. *International Journal for Numerical and Analytical Methods in Geomechanics*, 6(2):151–171, 1982.
- [21] David F Boutt. Poroelastic loading of an aquifer due to upstream dam releases. *Ground water*, 48(4):580–592, 2010.
- [22] Robert Burridge and Joseph B Keller. Poroelasticity equations derived from microstructure. *The Journal of the Acoustical Society of America*, 70:1140, 1981.
- [23] Jan Carmeliet, Hannelore Derluyn, Stijn Mertens, Peter Moonen, E Schlangen, and G De Schutter. Multiscale modelling of coupled problems in porous materials. In *International RILEM Symposium on Concrete Modelling-ConMod’08*, pages 325–336. RILEM Publications SARL, 2008.
- [24] Chia-Chieh Chu. *Multiscale methods for elliptic partial differential equations and related applications*. PhD thesis, California Institute of Technology, 2010.
- [25] Jay Chu, Björn Engquist, Maša Prodanović, and Richard Tsai. A multiscale method coupling network and continuum models in porous media ii-single-and two-phase flows. *Advances in Applied Mathematics, Modeling, and Computational Science*, pages 161–185.
- [26] Jay Chu, Björn Engquist, Maša Prodanovic, and Richard Tsai. A multiscale method coupling network and continuum models in porous media i: Steady-state single phase flow. *Multiscale Modeling & Simulation*, 10(2):515–549, 2012.
- [27] CRI Clayton, H Müller Steinhagen, and W Powrie. Terzaghi’s theory of consolidation, and the discovery of effective stress. In *International Journal of Rock Mechanics and*

- Mining Sciences and Geomechanics Abstracts*, volume 33, pages 162A–162A. Elsevier, 1996.
- [28] Massimo Cocco and James R Rice. Pore pressure and poroelasticity effects in coulomb stress analysis of earthquake interactions. *Journal of geophysical research*, 107(B2):2030, 2002.
 - [29] ME Contadakis and G Asteriadis. Hydrologic changes as possible earthquake precursor in greece. *Natural Hazards*, 23(1):29–47, 2001.
 - [30] Stephen C Cowin. Bone poroelasticity. *Journal of Biomechanics*, 32(3):217–238, 1999.
 - [31] H Darcy. Les fontaines publiques de la ville de dijon, 1856. *Dalmont, Paris*, 70.
 - [32] K. Delgado, P. & Kumar. A heterogeneous multiscale model of solid deformation mechanics using finite volume and direct stiffness methods. In *Proceedings of the 3rd Annual Southwest Energy Science & Engineering Symposium*, 2013.
 - [33] P. Delgado and K. Kumar. Generalization of a heterogenous multiscale framework coupling discrete microscale and continuous macroscale physics in a porous medium. In *Proceedings of the 2013 ASME Fluid Engineering Division Summer Meeting*, 2013.
 - [34] Dominique Derome, Ahmad Rafsanjani, Stefan Hering, Martin Dressler, Alessandra Patera, Christian Lanvermann, Marjan Sedighi-Gilani, Falk K Wittel, Peter Niemz, and Jan Carmeliet. The role of water in the behavior of wood. *Journal of Building Physics*, 2013.
 - [35] E. Detournay and A.H.D. Cheng. Fundamentals of poroelasticity1. 1993.
 - [36] I. Fatt. The network model of porous media. i. ii. iii. *Pet. Trans.*, 207(144), 1956.
 - [37] FJ Gaspar, FJ Lisbona, and CW Oosterlee. On a decoupled algorithm for poroelasticity and its resolution by multigrid. In *Proceedings of the ECCOMAS Computational Fluid Dynamics Conference, Delft*, 2006.

- [38] FJ Gaspar, FJ Lisbona, CW Oosterlee, and PN Vabishchevich. An efficient multigrid solver for a reformulated version of the poroelasticity system. *Computer methods in applied mechanics and engineering*, 196(8):1447–1457, 2007.
- [39] FJ Gaspar, FJ Lisbona, and PN Vabishchevich. A finite difference analysis of biot’s consolidation model. *Applied numerical mathematics*, 44(4):487–506, 2003.
- [40] FJ Gaspar, FJ Lisbona, and PN Vabishchevich. Staggered grid discretizations for the quasi-static biot’s consolidation problem. *Applied numerical mathematics*, 56(6):888–898, 2006.
- [41] Francisco J Gaspar, Francisco J Lisbona, and Petr N Vabishchevich. Finite difference schemes for poro-elastic problems. *Comput. Methods Appl. Math.*, 2(2):132–142, 2002.
- [42] Francisco J Gaspar, Francisco J Lisbona, and Petr N Vabishchevich. A numerical model for the radial flow through porous and deformable shells. *Comput. Methods Appl. Math.*, 4(1):34–47, 2004.
- [43] Margot G Gerritsen and Louis J Durlofsky. Modeling fluid flow in oil reservoirs. *Annu. Rev. Fluid Mech.*, 37:211–238, 2005.
- [44] David J Hart. *Laboratory measurements of poroelastic constants and flow parameters and some associated phenomena*. PhD thesis, UNIVERSITY OF WISCONSIN, 2000.
- [45] Wang Jing, Liu Huiqing, and Wang Zenglin. Quantitative models of development laws for heterogeneous sandstone reservoirs by water flooding. *Open Petroleum Engineering Journal*, 5:26–35, 2012.
- [46] J. Kim. *Sequential methods for coupled geomechanics and multiphase flow*. PhD thesis, Stanford University, 2010.
- [47] V. Kumar. *Advanced computational techniques for incompressible/compressible fluid-structure interactions*. PhD Thesis Rice University, 2005.

- [48] Pierre Ladevèze and Anthony Nouy. On a multiscale computational strategy with time and space homogenization for structural mechanics. *Computer Methods in Applied Mechanics and Engineering*, 192(28):3061–3087, 2003.
- [49] Daryl L Logan. *A first course in the finite element method*. Thomson Learning, 2007.
- [50] J Mandel. Consolidation des sols (étude mathématique)*. *Geotechnique*, 3(7):287–299, 1953.
- [51] Günther Meschke, Dirk Leonhart, Jithender J Timothy, and Meng-Meng Zhou. Computational mechanics of multiphase materials—modeling strategies at different scales. *Computer Assisted Mechanics and Engineering Sciences*, 18(1-2):73–89, 2011.
- [52] TJ Mitchison, GT Charras, and L Mahadevan. Implications of a poroelastic cytoplasm for the dynamics of animal cell shape. In *Seminars in cell & developmental biology*, volume 19, pages 215–223. Elsevier, 2008.
- [53] Anna Naumovich. *Efficient numerical methods for the Biot poroelasticity system in multilayered domains*. PhD thesis, PhD Thesis, Technical University Kaiserslautern, 2007.
- [54] Bogdan Orlic. Some geomechanical aspects of geological co2 sequestration. *KSCE Journal of Civil Engineering*, 13(4):225–232, 2009.
- [55] Grigorios A Pavliotis and Andrew M Stuart. *Multiscale methods: averaging and homogenization*, volume 53. Springer Science+ Business Media, 2008.
- [56] Phillip Joseph Phillips and Mary F Adviser-Wheeler. *Finite element methods in linear poroelasticity: theoretical and computational results*. University of Texas at Austin, 2005.
- [57] P.J. Phillips and M.F. Wheeler. A coupling of mixed and continuous galerkin finite element methods for poroelasticity i: the continuous in time case. *Computational Geosciences*, 11(2):131–144, 2007.

- [58] P.J. Phillips and M.F. Wheeler. A coupling of mixed and continuous galerkin finite element methods for poroelasticity ii: the discrete-in-time case. *Computational Geosciences*, 11(2):145–158, 2007.
- [59] P.J. Phillips and M.F. Wheeler. A coupling of mixed and discontinuous galerkin finite-element methods for poroelasticity. *Computational Geosciences*, 12(4):417–435, 2008.
- [60] James R Rice and Michael P Cleary. Some basic stress diffusion solutions for fluid-saturated elastic porous media with compressible constituents. *Rev. Geophys. Space Phys*, 14(2):227–241, 1976.
- [61] APS Selvadurai. *Mechanics of poroelastic media*, volume 35. Springer, 1996.
- [62] Reza Sepehrinia, M Reza Rahimi Tabar, and Muhammad Sahimi. Numerical simulation of the localization of elastic waves in two-and three-dimensional heterogeneous media. *Physical Review B*, 78(2):024207, 2008.
- [63] RE Showalter. Diffusion in poro-elastic media. *Journal of mathematical analysis and applications*, 251(1):310–340, 2000.
- [64] Karl Terzaghi and Otto Karl Fröhlich. *Theorie der Setzung von Tonschichten*. Deuticke, 1936.
- [65] H.F. Wang. *Theory of linear poroelasticity with applications to geomechanics and hydrogeology*. Princeton University Press, 2000.
- [66] E Weinan. *Principles of multiscale modeling*. Cambridge University Press, 2011.
- [67] Son-Young Yi. A coupling of nonconforming and mixed finite element methods for biot’s consolidation model. *Numerical Methods for Partial Differential Equations*, 2013.
- [68] Alexander Ženíšek. The existence and uniqueness theorem in biot’s consolidation theory. *Aplikace matematiky*, 29(3):194–211, 1984.

- [69] O.C. Zienkiewicz. *Coupled problems and their numerical solution, in Numerical Methods in Coupled Systems, edited by Lewis, Bettes, & Hinton*. John Wiley & Sons Ltd., 1984.
- [70] OC Zienkiewicz and T Shiomi. Dynamic behaviour of saturated porous media; the generalized biot formulation and its numerical solution. *International journal for numerical and analytical methods in geomechanics*, 8(1):71–96, 1984.
- [71] Olgierd Cecil Zienkiewicz, Robert Leroy Taylor, and Jian Z Zhu. *The finite element method: its basis and fundamentals*, volume 1. Butterworth-Heinemann, 2005.

Curriculum Vitae

Paul M. Delgado was born August 2nd, 1981. The first and only son of Pablo and Elva Delgado, he graduated from Manzano High School, Albuquerque, New Mexico in the Spring of 1999. He entered the University of New Mexico in the fall of 1999 and in the fall of 2003, he graduated with a B.S. in Mathematics and Spanish. He interned for NASA Ames Research Center in 2002 and Los Alamos National Laboratories in 2004. In the fall of 2004, he returned to the University of New Mexico to pursue a masters degree in Applied Mathematics. He also published the book "Calculus Jokes: For the Not-So-Typical Math Nerd" in 2005. He received an M.S. degree from UNM in Applied Mathematics in 2007 under the guidance of Dr. Kristen Umland with a thesis entitled "Calculus Jokes: the effects of the use of humor in a calculus course". In the fall of 2007, he became a full time lecturer in the mathematics department at the University of Texas at El Paso. In 2011, he entered the Computational Science PhD program at the University of Texas at El Paso as a research assistant. He became an XSEDE Scholar and an NSF Fellow (HRD-1139929) in 2012. He was also president of UTEP's Society for Industrial and Applied Mathematics and founded the UTEP Graduate Research Elevator Pitch Competition.

Permanent address: 220 Torres St.

El Paso, Texas 79922